

This is the author's peer reviewed, accepted manuscript. However, the online version of record will be different from this version once it has been copyedited and typeset.

PLEASE CITE THIS ARTICLE AS DOI: 10.1063/5.0009138

1                   **Evaluating the WFIP2 updates to the HRRR model using scanning Doppler lidar**  
2                   **measurements in the complex terrain of the Columbia River Basin**

3                   Yelena L. Pichugina<sup>1,2</sup>, Robert M. Banta<sup>1,2</sup>, W. Alan Brewer<sup>2</sup>, L. Bianco<sup>1,4</sup>, C. Draxl<sup>5</sup>, J. Kenyon<sup>1,3</sup>,  
4                   J. K. Lundquist<sup>6,7</sup>, J.B. Olson<sup>1</sup>, D.D. Turner<sup>3</sup>, S. Wharton<sup>11</sup>, J. Wilczak<sup>4</sup>, S. Baidar<sup>1,2</sup>,  
5                   L.K. Berg<sup>5</sup>, H.J.S. Fernando<sup>8</sup>, B.J. McCarty<sup>1,2</sup>, R. Rai<sup>5</sup>, B. Roberts<sup>6</sup>,  
6                   J. Sharp<sup>9</sup>, W.J. Shaw<sup>5</sup>, M.J. Stoelinga<sup>10</sup>, and R. Worsnop<sup>7</sup>

7                   <sup>1</sup>CIRES, University of Colorado, Boulder, CO 80309, USA

8                   <sup>2</sup>NOAA Chemical Sciences Laboratory, Boulder, CO 80305, USA

9                   <sup>3</sup>NOAA Global Systems Laboratory, Boulder, CO 80305 USA

10                  <sup>4</sup>NOAA Physical Sciences Laboratory, Boulder, CO 80305, USA

11                  <sup>5</sup>Pacific Northwest National Laboratory, Richland, WA 99352, USA

12                  <sup>6</sup>National Renewable Energy Laboratory, Golden, CO 80401, USA

13                  <sup>7</sup>University of Boulder, Boulder, CO 80309, USA

14                  <sup>8</sup>University of Notre Dame, Notre Dame, IN 46556, USA

15                  <sup>9</sup>Sharply Focused LLC, Portland, OR 97213, USA

16                  <sup>10</sup>Vaisala, Seattle, WA 98121, USA.

17                  <sup>11</sup>Lawrence Livermore National Laboratory, Livermore, CA 94550, USA

18                  Correspondence to: Yelena Pichugina (Yelena.Pichugina@noaa.gov)

19                  **Abstract.** The wind-energy (WE) industry relies on numerical weather prediction (NWP) forecast models as  
20                  foundational or base models for many purposes, including wind-resource assessment and wind-power forecasting.  
21                  During the Second Wind Forecast Improvement Project (WFIP2) in the Columbia River Basin of Oregon and  
22                  Washington, a significant effort was made to improve NWP forecasts through focused model development, to include  
23                  experimental refinements to the High Resolution Rapid Refresh (HRRR) model physics and horizontal grid spacing.  
24                  In this study, the performance of an experimental version of HRRR that includes these refinements is tested against a  
25                  control version, which corresponds to that of the operational HRRR run by NOAA/NCEP at the outset of WFIP2. The  
26                  effects of horizontal grid resolution were also tested by comparing wind forecasts from the HRRR (with 3-km grid  
27                  spacing) with those from a finer-resolution HRRR nest with 750-m grid spacing. Model forecasts are validated against  
28                  accurate wind-profile measurements by three scanning, pulsed Doppler lidars at sites separated by a total distance of  
29                  71 km. Model skill, and improvements in model skill, attributable to physics refinements and improved horizontal grid  
30                  resolution varied by season, by site, and during periods of atmospheric phenomena relevant to WE. In general, model  
31                  errors were the largest below 150 m AGL. Experimental HRRR refinements tended to reduce the mean absolute error  
32                  (MAE) and other error metrics for many conditions, but degradation in skill (increased MAE) was noted below 150 m

This is the author's peer reviewed, accepted manuscript. However, the online version of record will be different from this version once it has been copyedited and typeset.

PLEASE CITE THIS ARTICLE AS DOI: 10.1063/1.50009138

33 AGL at the two lowest-elevation sites at night. Finer resolution was found to produce the most significant reductions  
34 in the error metrics.

35  
36

## 37 **1 Introduction**

38 Numerical weather prediction (NWP) forecast models are widely used in the wind energy (WE) industry as  
39 foundational or base models for wind resource assessment and wind-power forecasting. Continual changes to the base  
40 forecast models, by implementing updated model physics, parameterization schemes, and horizontal grid spacing, are  
41 performed to improve model skill. Evaluating and quantifying the effects of these updates on model performance  
42 require accurate measurements of atmospheric variables such as wind speed, wind direction, and turbulence (Bonin et  
43 al. 2017) in various landscapes and atmospheric conditions.

44 The performance of mesoscale NWP models has been evaluated using measurements above the surface from  
45 various instruments during short-term field experiments over complex terrain (Fast and Darby 2004, Yang et al. 2017,  
46 Zhong and Fast, 2003), coastal areas (Draxl et al. 2014), and offshore (Drechsel et al. 2012, Krogsæter and J. Reuder  
47 2015, Pichugina et al. 2017, Banta et al. 2018) documenting the relative strengths and weaknesses of model forecasts  
48 at a horizontal grid spacing of 1 km or less.

49 In this study, the performance of the High Resolution Rapid Refresh (HRRR) and a HRRR nest (HRRRNEST),  
50 developed at the Global Systems Laboratory (GSL) of the National Oceanic and Atmospheric Administration (NOAA)  
51 /Earth Systems Research Laboratories (ESRL), is investigated by measurements from scanning, pulsed Doppler lidars  
52 during the Second Wind Forecast Improvement Project (WFIP2) in the complex terrain of the Columbia River Valley  
53 in Oregon and Washington in the United States. This 18-month long (September 2015 to April 2017), multi-institutional  
54 collaborative project aimed to improve forecasting of wind flow complicated by mountainous terrain, coastal effects,  
55 and the presence of numerous wind farms in this area. Overviews of the WFIP2 campaign describe the experiment and  
56 scientific objectives (Shaw et al., 2019), instrumentation involved in the experiment and the logistics of their  
57 deployments (Wilczak et al. 2019), and the model-physics updates made during WFIP2 (Olson et al. 2019).

58 WFIP2 measurements from three scanning lidars separated from each other by 30-40 km, sited at different terrain  
59 elevations over a total distance of 71 km, were used previously (Pichugina et al., 2019) to analyze temporal and spatial  
60 variability of the wind flow and to evaluate the performance of the operational HRRR-NCEP (National Centers for  
61 Environmental Protection) model for the entire 18-month period. Pichugina et al. (2019) found significant differences  
62 in the characteristics of model errors between seasons, over the diurnal cycle at each site and between sites. In winter,  
63 the highest-elevation lidar site (Wasco, Oregon) showed anomalously high model wind speeds, which were attributed  
64 to overly shallow predicted cold pools. In summer, the two lower-elevation sites (Arlington and Boardman, Oregon)  
65 showed systematic low biases in the simulated wind-turbine rotor-layer wind speeds at night, due to a premature end  
66 to a diurnal, sea-breeze related, marine-intrusion flow (Banta et al. 2020). Both of these error types influenced the  
67 annual error statistics.

This is the author's peer reviewed, accepted manuscript. However, the online version of record will be different from this version once it has been copyedited and typeset.

PLEASE CITE THIS ARTICLE AS DOI: 10.1063/1.50009138

68 The HRRR-NCEP versions validated by Pichugina et al. (2019) were run operationally during WFIP2—version  
69 1 of the HRRR-NCEP (HRRRv1) until 23 August 2016, then version 2 of the HRRR-NCEP (HRRRv2) afterward—as  
70 described by Benjamin et al. (2016) and Olson et al. (2019). By the end of WFIP2, NOAA/ESRL had developed  
71 experimental refinements for its nonoperational version of the HRRR.

72 For the present study, a provisional HRRR model was run in two domain configurations: a ‘parent’ HRRR with  
73 standard 3-km horizontal grid spacing, and an experimental, finer-resolution, HRRR nest with 750-m horizontal grid  
74 spacing. Additionally, both domain configurations were run with a control physics configuration and again with an  
75 experimental physics configuration. The control configuration represents the state of HRRR physics at the beginning  
76 of WFIP2 (September 2015), which also corresponds to the physics of HRRRv1, whereas the experimental  
77 configuration represents physics developments made during WFIP2 (Olson et al. 2019, Bianco et al. 2019), to be  
78 discussed in a later section.

79 We use the Doppler lidar measurements at the three sites to see how these updates affected model skill season  
80 by season, site by site, and over periods with atmospheric phenomena relevant to WE, and to determine the effects of  
81 finer resolution on model performance. Evaluating improvement in model skill involves comparing model errors from  
82 one version of the model to the next. This evaluation requires accurate measurements with known levels of uncertainty,  
83 against which to validate each model version. Here we exploit the accuracy of wind-speed profile measurements from  
84 the Doppler lidars to perform these comparisons (Banta et al. 2013). The analyses quantify model error as related to  
85 height, diurnal cycle, and season, and evaluate the version-to-version differences.

86 The paper is organized as follows: Section 2 describes the location of lidars and provides a short discussion of  
87 the models used in the study and wind flow complexity in the WFIP2 research area. Section 2 also describes the periods  
88 selected for model reforecasts and shows representativeness of the atmospheric phenomena observed during reforecast  
89 periods relative to 2016 and to the entire length of the WFIP2 field campaign (Sep 2015–Mar 2017). This section also  
90 illustrates signatures of atmospheric events (westerly Gap Flow and Cold Pool events) detected in lidar time-height  
91 cross-sections over diurnal periods and in the composites over all days of the particular event observed during 2016.  
92 Section 3 provides an overview of annual and seasonal wind flows in the lowest 1 km above ground level (AGL) from  
93 lidar measurements and two runs of both models and presents annually/seasonally averaged profiles of validation  
94 metrics for both models. Section 3 also focuses on the evaluation of model errors at 80 m AGL and presents analyses  
95 for different wind directions and diurnal periods, and presents analyses of model performance during the most frequent  
96 atmospheric events observed in the research area and presents model error dependency on both event type and  
97 instrument location. Section 4 contains a discussion of the implications of these findings to model evaluation using  
98 field data. Section 5 presents a summary and conclusions.

## 99 **2 Methods and forecast validation setup**

### 100 **2.1 Scanning Doppler lidars**

101 Two NOAA scanning, pulsed Doppler lidars (Leosphere WindCube 200S) were deployed 40 km apart near the  
102 Wasco and Arlington, Oregon airports, providing real-time wind measurements from September 2015 through April  
103 2017. The third scanning Doppler lidar (Halo Streamline XR) was deployed by the University of Notre Dame (UND)

104 to a site near Boardman, 31 km east-northeast of Arlington (Fig. 1), and continuously operated from January through  
105 December 2016. These instruments provided concurrent measurements of wind flow, each using similar scanning  
106 sequences and data-processing techniques. They were located along a west-southwest/east-northeast line within a high-  
107 density (~2,000 turbines) “wind-energy corridor” region of the Columbia River Basin (Banta et al. 2020).

108 Details of the lidars used during WFIP2 are described in Pichugina et al. (2019). These include lidar operational  
109 parameters, details of scanning pattern, data quality control, and post-processing techniques used to obtain vertical  
110 profiles of the mean wind variables (wind speed and direction) using line-of-sight (LOS) velocity measurements from  
111 the near-surface up to 3.5 km. An assessment of the scanning Doppler lidar random measurement uncertainty of wind  
112 speed in the complex terrain of WFIP2 (Pichugina et al. 2019) showed significant diurnal variability with a peak value  
113 of  $\sim 0.02 \text{ m s}^{-1}$  around local noon as well as dependence on terrain complexity for each site (with larger uncertainty at  
114 the Wasco site compared to the lower-elevation Boardman site). Overall, the lidar measurement uncertainty was  
115 determined to be small enough to quantify the accuracy of the operational HRRR-NCEP model to properly forecast  
116 challenging wind-flow conditions in WFIP2. These accuracies are also sufficient for the comparison of different model  
117 versions.

## 118 2.2 NWP models used in the study

119 The RAP and HRRR models are hourly updating, operational forecast models developed by researchers at  
120 NOAA/GSL, and which employ the Advanced Research version of the WRF Model (WRF-ARW; Skamarock et al.  
121 2008). Benjamin et al. (2016) describe the evolution of the RAP and HRRR models through 2016, and Olson et al.  
122 (2019) describe the RAP and HRRR model-development efforts undertaken during WFIP2.

123 To support the goals of WFIP2 using the limited computational resources available to the project, a  
124 nonoperational version of the HRRR was used for WFIP2 (Olson et al. 2019). This provisional WFIP2 HRRR  
125 (hereafter simply “HRRR”, unless otherwise noted) encompassed a smaller domain than its operational counterpart, as  
126 shown by the large green box in Fig. 2a, but retained the standard 3-km horizontal grid spacing. Within the HRRR, a  
127 nested domain (hereafter “HRRRNEST”), shown by the small green box in Fig. 2a, was run at 750-m horizontal grid  
128 spacing. HRRR forecasts employed a so-called “cold start” initialization, where initial conditions were supplied from  
129 the operational RAP without additional data assimilation or prior cycling, as described by Olson et al. (2019, pp. 2204–  
130 2205). In turn, the HRRRNEST initializations were delayed 3 h after the HRRR initialization (see Bianco et al. 2019)  
131 to minimize “spin up” problems at sub-kilometer scales. The HRRR was initialized twice daily at 0000 and 1200  
132 UTC (lagged 3 h by the HRRRNEST), and both the HRRR and HRRRNEST provided 24-h forecasts at 15-min output  
133 intervals. The collection of HRRR and HRRRNEST forecasts used in this study are referred to as *reforecast* runs.  
134 Table 7 (Appendix A) summarizes key aspects of the model design used for reforecasts.

135 During WFIP2, significant refinements were made to the HRRR and HRRRNEST, intended to improve how  
136 these models represent complex terrain, the vertical mixing between the surface and the atmosphere, and the impact of  
137 turbulence in the horizontal as well as vertical directions (Olson et al. 2019). To evaluate these improvements, HRRR  
138 and HRRRNEST reforecasts for selected periods, to be discussed in the next subsection, were produced using a control  
139 configuration (CNTR), which contained the parameterizations and other model routines present at the beginning of  
140 WFIP2 (Olson et al 2019), and again using an experimental configuration (EXPR), which contained all physics

141 modifications developed during WFIP2. Table 8 summarizes key aspects of the CNTRL and EXPR configurations;  
142 additional details are available in Olson et al. (2019). Reforecasts from both configurations were validated against  
143 wind-profile measurements at three Doppler lidar sites to assess the impacts of these updates on model skill at locations  
144 having different terrain complexity and wind-farm effects on wind flows (Fig1b). To assess the mean model skill over  
145 the extended (~70 km) area, including the net impact of terrain and wind turbines there, the measured and modeled  
146 profiles were averaged over the three lidar sites, referred in this paper as three-site composites.

147 An example of HRRRNEST-modeled, 80-m winds superimposed on the area topography (Fig. 2b) illustrates  
148 the complexity of wind flow in the research area. The figure shows increased westerly winds through the narrow  
149 Columbia River Gorge, (the only sea-level gap through this range [Sharp and Mass 2002]), driven by higher pressure  
150 offshore to the west of the Cascade Mountains, as well as vortices of wind speed and direction caused by the mountain  
151 ridge and local topography. Terrain complexity expressed as the standard deviation of the terrain elevations (SDE)  
152 within a 3-km radius of each instrument location (Ascione et al. 2008), is largest for the Arlington site (71.1 m) followed  
153 by 26.3 m for Wasco, and 18.6 m at Boardman (Pichugina et al. 2019). The lidar deployment locations and terrain  
154 elevation of the surrounding area relative to a portion of the horizontal grid of each model (HRRR and HRRRNEST)  
155 are shown in Fig. 2c.

156 Data from the three Doppler lidars were not assimilated into the model runs, so the lidar wind profiles provide  
157 an independent validation dataset. For validation of models against lidar measurements, the gridded model wind values  
158 from control and experimental runs of both models were extracted at the position of the lidar either by bi-linear  
159 interpolation of winds from the surrounding four grid points or by using modeled winds from the nearest grid point  
160 (Appendix B). Both methods show very similar results for each lidar location (Fig. 18; Table 4), with correlation  
161 coefficients of 0.99 between the two extraction techniques, differences in mean wind speed of 0.01 to 0.22 m s<sup>-1</sup>, and  
162 standard deviations of 0.0 to 0.085 m s<sup>-1</sup>. The offset differs from 0.02 to 0.08 m s<sup>-1</sup> between the results and the slope  
163 varies from 0.97 to 1.02 between the lowest and the highest value. Here, we use bilinear interpolation. For quantitative  
164 comparisons of wind-speed profiles, the modeled values obtained at the location of each lidar were then linearly  
165 interpolated to the heights of lidar measurement. The effects of the vertical-interpolation method and uncertainties of  
166 two approaches—first, when measurements are interpolated to model output levels (lidar-to-model), and second, when  
167 modeled variables are interpolated to the heights of lidar measurements (model-to-lidar)—are discussed in Pichugina  
168 et al. (2017). This interpolation method “allows the fine-scale structure of the lidar data, with such features as thin shear  
169 layers and LLJ noses, to be accounted for in the error computations.” The LOS lidar measurements were then averaged  
170 over vertical bins of 10 m in the lowest 200 m AGL, gradually increasing to 25 m up to 1 km AGL, 50 m up to 2 km  
171 m AGL, and 100 m up to 5 km AGL.

### 172 2.3 Representativeness of the reforecast periods.

173 In addition to the assessment of model errors for different seasons and at different terrain complexity,  
174 understanding of model performance during frequently occurring atmospheric phenomena is important for wind energy  
175 operations. A variety of synoptic conditions were observed over the study area and were cataloged in an Event Log  
176 (Draxl et al. 2019, Shaw et al. 2019, Wilczak et al. 2019) by a group of meteorologists after review of all available  
177 WFIP2 observations, satellite imagery, real-time simulations from all WFIP2 models, and discussion of synopses of

This is the author's peer reviewed, accepted manuscript. However, the online version of record will be different from this version once it has been copyedited and typeset.

PLEASE CITE THIS ARTICLE AS DOI: 10.1063/5.0009138

178 the daily weather. The determination of event type involved subjectivity associated with the identification process.  
179 Besides, an event was assigned a category only if it was observed to occur over a major portion of the study area. An  
180 overview of the mechanism and frequency of the events observed throughout the WFIP2 in the study area appears in  
181 Wilczak et al. (2019).

182 Recent WFIP2 studies provide in-depth analyses of key phenomena to understand how well the HRRR  
183 simulated individual flow types and how periods of these events may impact aggregate wind power generation within  
184 the Bonneville Power Authority (BPA) balancing area  
185 <https://transmission.bpa.gov/Business/Operations/Wind/twndbspt.aspx>.

186 These detailed studies include cold-pool periods (McCaffrey et al. 2019, Whiteman et al. 2001, Zhong et al.  
187 2001), thermodynamically-driven westerly gap flows (Banta et al. 2020), and mountain waves and topographic wakes  
188 (Draxl et al. 2020).

189 Two studies have used the WFIP2 dataset to evaluate the updates in the EXPR versions vs. the CNTR versions.  
190 Olson et al. (2019) and Bianco et al. (2019) used 80-m AGL wind-speed data averaged over 22 sites, 19 equipped with  
191 Doppler sodars, 2 with profiling lidars, and one with a scanning lidar, to calculate model-error and improvement  
192 statistics including diurnal time series (for reference, the locations of these 22 sites are shown in Section 4). The Olson  
193 et al. (2019) study also analyzed time-height cross-sections of wind speed averaged over eight 915-MHz wind-profiling  
194 radars (WPRs). The studies found a strong diurnal behavior of the model errors, the largest errors occurring at nighttime.  
195 Large positive biases were found during winter at higher-elevation sites (including Wasco) due to the modeled cold-  
196 pool depths being too shallow. Significant low biases and large mean absolute error (MAE) occurred in summer at  
197 night, due to the models not properly representing marine-intrusion type gap flows (Banta et al. 2020). These findings  
198 all confirmed that the results and interpretations of Pichugina et al. (2019) using HRRR-NCEP model error statistics  
199 averaged over the entire WFIP2 study period apply equally to the CNTR and EXPR reforecast runs. Olson et al. (2019)  
200 and Bianco et al. (2019) showed that the updates to HRRR in EXPR produced significant improvements in winter  
201 because of better predictions of cold-pool depth, but skill decreased in summer and spring at night. In Bianco et al.  
202 (2019) the EXPR run updates were found to improve forecast skill by 0.1 to 0.2 m s<sup>-1</sup> at 80 m, when averaged over all  
203 four reforecast periods and all 22 locations, and error profile data from the WPRs indicated similar improvements  
204 through a 200- to 600-m layer.

205 Reforecast periods for model runs were selected to provide a reasonable balance between computational expense  
206 and coverage of consequential meteorological event types. These periods represent six weeks during each season, as in  
207 Olson et al. (2019) and Bianco et al. (2019). An additional three weeks of simulation in August 2016 was added for a  
208 detailed study of summertime thermally forced westerly gap-flow events (Banta et al. 2020, Olson et al. 2019). Analysis  
209 of this additional model-output period is included in the present investigation.

210 Overall, the dataset for the reforecast period covers fewer days in the year than the operational HRRR-NCEP  
211 dataset used by Pichugina et al. (2019), but the 15-min output of these models, along with the finer grid resolution of  
212 the HRRRNEST, provide opportunities for more detailed analyses of wind-flow dynamics compared to the hourly  
213 output that was saved from the operational model. The major error characteristics identified in the HRRR-NCEP by  
214 Pichugina et al. (2019) are also found in the HRRR-CNTR reforecast runs, as just described.

215 Distributions of the observed events by event type for the whole experiment, for the annual period of 2016 (the  
216 year of concurrent lidar measurements from all three lidars), and for the reforecast periods selected in 2016 are shown  
217 in Fig. 3a. This figure establishes that each of the major events occurred during the selected reforecast periods.

218 The monthly distribution of events during reforecast periods (Fig. 3b) shows that westerly gap flows occurred  
219 every month. Two types of westerly gap-flow forcing were identified during the event logging, one due to the synoptic  
220 cross-barrier pressure gradient, and the other due to the diurnal heating-cooling cycle, such as the marine-intrusion  
221 flows investigated by Banta et al. (2020). The westerly Gap flows occurred more often during warmer months of the  
222 year (April-September) when a large fraction of these flows were of the thermally forced type (Fig. 3b). Cold-pool  
223 events occurred mostly during winter and fall months, (McCaffrey et al. 2019). The frequent occurrence of westerly  
224 gap flow (Fig. 3a, b) agrees with the regional prevalence of westerly winds in the annual and seasonal (except winter)  
225 distributions of wind direction found by Pichugina et al. (2019) from both lidar observations and HRRR-NCEP output  
226 of 80-m and rotor-layer winds.

227 The representativeness (%) of each event type during the reforecast periods is given in Table 1 by comparison  
228 to the total number of events observed in 2016 and during 18 months of WFIP2. The relative frequency of each event  
229 type over all reforecast periods was similar to the frequency observed for the year and for the WFIP2 period, except  
230 for cold-pool events, which (at 9.2% of all reforecast events) were underrepresented in the reforecast sample.

#### 231 **2.4 Signatures of atmospheric events in lidar observations**

232 Major event types captured by lidar measurements at a 15-min temporal resolution during the reforecast period were  
233 cold pools, westerly gap flows, and easterly gap flows. The daily evolution of wind flow at each site (Fig. 4) for selected  
234 days illustrates major signatures of these atmospheric event types as follow:

235 *Cold pool event on 26 February.* Weak easterly winds associated with the cold pool event occur throughout most  
236 of the day. At all sites, average wind speed below 200 m slowed to  $<2 \text{ m s}^{-1}$  by 0500 UTC and remained low for hours.  
237 Note that this is below the average cut-in ( $\sim 3\text{-}4 \text{ m/s}$ ) wind speed (i.e., minimum wind speed for power generation) for  
238 most wind turbines.

239 *Westerly Gap Flow on 30 June.* Predominant westerly winds were associated with a marine intrusion event. Strong  
240 nocturnal wind speeds ( $12\text{-}15 \text{ m s}^{-1}$  in the rotor layer) decreased to  $6\text{-}10 \text{ m s}^{-1}$  for the rest of the day. A mesoscale  
241 pressure gradient arising from E-W differential heating was superimposed upon a more steady-state synoptic-scale  
242 pressure gradient.

243 *Easterly Gap Flow on 7 April.* An offshore surface low, moving northward during the day, provided the pressure  
244 gradient for a weak easterly gap flow in the lowest 200-400 m, increasing with height.

245 *Mountain wave on 19 September.* A low-pressure system over the western half of the continental United States led  
246 to northwesterly flow in the Columbia River Gorge, which caused stationary mountain waves east of the Cascade  
247 Mountains. Doppler lidar cross-sections (Fig. 4d) reveal evidence for trapped lee waves through temporal fluctuations  
248 of mean wind speed, but more accurate estimates of wave activity were made from high temporal-resolution lidar  
249 measurements of vertical velocity as shown in Draxl et al. (2020). These measurements were obtained by the newly  
250 developed micro-Doppler lidar (Schroeder et al. 2019) tested during a September-October 2016 deployment to the  
251 Wasco site.

This is the author's peer reviewed, accepted manuscript. However, the online version of record will be different from this version once it has been copyedited and typeset.

PLEASE CITE THIS ARTICLE AS DOI: 10.1063/5.0009138

252 Differences in the diurnal flow structure and evolution of each event emerge among sites (Fig. 4). Further  
253 averaging of wind profiles over all instances of each flow-event type at each site (Fig. 5a-c), and for the 3-site  
254 composites (Fig. 5d), leads to smoothed but representative mean features of these flows. The Easterly flow composites  
255 represent all days with easterly wind directions as detected by all three lidars, regardless of how they formed (i.e., they  
256 could be associated with cold pools, easterly gap flows, or other forcings). Note that a mountain-wave phenomenon is  
257 generally unique and may occur at different times of the day, so that diurnal composite time-height cross-sections are  
258 unlikely to be representative of the structure or evolution of individual events.

259 Comparing wind-speed structure and behavior among the three lidar sites (Fig. 1b) reveals wind-flow variations  
260 due to distance, elevation, and the presence of wind turbines. During prevalent westerly winds, the westernmost lidar  
261 at Wasco documented an inflow profile upstream of the wind farms, whereas the lidar at the Arlington site shows how  
262 the flow changed due to location and may give insight as to how the wind farms affect the shape and magnitude of the  
263 wind profile (Banta et al. 2015, Fitch et al. 2012, Lundquist et al. 2019, Rajewski et al. 2013, Redfern et al. 2019,  
264 Siedersleben et al. 2018, 2020). When the flow was from easterly directions, both lidars measured winds affected by  
265 both terrain complexity and wind farms. The flow at the easternmost Boardman site, where winds were weakest of the  
266 three sites, was least influenced by wind farms. Considering the above factors is important for selecting a proper site  
267 for any measurement system.

268 Meteorological events often persisted for several days, accompanied by fluctuations in wind speed and/or wind  
269 direction. Strong increases or decreases of wind speed over a few hours, known as wind *ramp* events, lead to a  
270 corresponding ramping in wind power production. Errors in timing or intensity of these ramp events may cause  
271 significant discrepancies between model-predicted and actual power output (Bianco et al. 2019).

272 The scanning lidars were located along the W-SW wind direction frequently observed over the research area.  
273 During episodes of westerly or easterly winds, the variations in wind power computed from lidar measurements can  
274 approximate the fluctuations of total power generated over the BPA area (see Wilczak et al. 2019 for methodology).  
275 Examples of 80-m wind-speed ramps and wind power computed from lidar measurements at 3 sites as well as the BPA-  
276 reported power generation are shown for a westerly gap-flow event on 13-19 August and a cold pool event on 07-13  
277 February (Fig. 6). During the August case, marine-intrusion flows brought strong nocturnal winds to the area and a  
278 strong diurnal cycle to both wind speed and total generated power.

279 The variations of wind speed and wind power computed from lidar measurements are similar to those of the  
280 power generated over the BPA area. During the August period (Fig. 6a-c), large up or down power ramps reached 3  
281 GW or more (17 August). Time offsets among the lidar-measured ramps in wind speed and between these ramps and  
282 those in the normalized BPA power occurred as the wind-surge event propagated over the 30-40 km distance from one  
283 site to the next (Fig. 1). These time offsets produced discrepancies between individual-site wind measurements and  
284 total power produced but averaging the winds over the three sites smooths the temporal offsets and produces better  
285 agreement and higher temporal correlations. The cold pool during the 07-13 February case (Fig. 6d-f) brought weak  
286 winds to the area leading to low BPA power generation; the power ramped up to 2.5 GW by the end of this period as  
287 the cold pool dissipated and wind speeds increased.



288 Distributions of wind speed and wind direction (Fig.6, bottom row) during the August reforecast period show  
289 stronger wind speeds with predominant westerly winds at each site, whereas the February case had weaker winds and  
290 a larger percentage of easterly flow. A better correlation between power computed from lidar measurements and BPA  
291 generation is found for the August case when the winds were consistently from the west. The correlation coefficient  
292 ( $R^2$ ) values for this period are 0.83, 0.86, 0.78, and 0.95 for Wasco, Arlington, Boardman, and the 3-site composites,  
293 respectively, illustrating how the three-site averaging correlates better with the total power generated in a month  
294 (August) when propagating diurnal wind-surge events occurred often. For the February case of weak wind speeds and  
295 a broader range of wind directions, correlation values are 0.52, 0.78, and 0.69 for Wasco and Arlington, and for the 3-  
296 site composites, respectively. No linear relationship was found for the weakest winds at the lowest Boardman site  
297 situated further to the east of wind farms in the area. Results from Fig. 6a and b illustrate that measurements from  
298 Doppler lidars properly located along the prevalent winds may in some conditions be adequate for the assessment of  
299 wind resources in the larger area of surrounding wind farms.

### 300 3. Results: Model validation by lidar measurements

301 HRRR model performance was quantified using several validation metrics: bias (BIAS), root mean square error  
302 (RMSE) and mean absolute error (MAE). The validation metrics obtained for annual and seasonal periods and for cases  
303 of interesting meteorological events observed in the study area, are analyzed as diurnal time-height cross-sections,  
304 mean profiles, and time-series of hub-height (80-m AGL) winds. These analyses allow models to be assessed regarding  
305 model resolution (HRRRNEST vs. HRRR) and model-physics updates (EXPR vs. CNTR runs). All types of analysis  
306 performed also provide information about model errors between sites of different complexity as well as differences in  
307 model performance for seasons and major events.

#### 308 3.1 Time-height analysis

##### 309 3.1.1 Annual model performance

310 Time-height sections from lidar measurements and HRRR-model output for the 00z run (Fig.7a-c), averaged  
311 over all reforecast periods in 2016 (which we will refer to as *annual*, even though not all days were used), demonstrate  
312 a similarity in diurnal variability of HRRR vs. lidar-measured wind speed. The influence of the frequent westerly gap  
313 flows (46% of all events counted: Fig. 3 and Table 1) on the annual mean is evident at each site and for the 3-site  
314 composites. Winds were fastest at night, and these nocturnal winds were stronger ( $\geq 10 \text{ m s}^{-1}$ ) at the highest, western-  
315 most Wasco site, whereas the weakest winds ( $\sim 7\text{-}8 \text{ m s}^{-1}$ ) were observed at the lowest, eastern-most Boardman site.  
316 The diurnal variability of winds at the Arlington site most closely resembled the diurnal variability of the 3-site  
317 composites.

318 The biases between HRRR-CNTR and lidar (Fig. 7d) and HRRR-EXPR and lidar (Fig. 7e) varied mostly  
319 between  $-2$  and  $+2 \text{ m s}^{-1}$  at the Wasco and Arlington sites with larger (up to  $\pm 3 \text{ m s}^{-1}$ ) values above 400 m AGL at  
320 Boardman. Both models tended to overestimate wind speeds above 300 m around and just after the evening transitions  
321 (0000-0500 UTC) and between 1200 and 1800 UTC at Wasco. In the rotor layer, the runs (except for the CNTR at  
322 Wasco) tended to underestimate wind speeds, by as much as  $3 \text{ m s}^{-1}$  for the EXPR run at Arlington.

This is the author's peer reviewed, accepted manuscript. However, the online version of record will be different from this version once it has been copyedited and typeset.

PLEASE CITE THIS ARTICLE AS DOI: 10.1063/5.0009138

323 At Boardman, the winds in the lidar cross-section above ~500 m were considerably weaker than at the other two  
324 sites. Both model versions, however, maintained the relatively stronger winds aloft, resulting in large positive biases  
325 reaching  $3 \text{ m s}^{-1}$ . The large positive biases in the 3-site composite cross-sections thus mostly reflect these high biases  
326 aloft at Boardman. Raw LOS lidar data were not available for the lidar at Boardman to use for the quality-assurance  
327 procedures, as described by Pichugina et al. (2019), so these 500- to 1000-m-AGL values may be from vertical regions  
328 of low lidar signal-to-noise ratio, and consequently may not be as accurate as at the two other sites. Therefore, as a  
329 precaution, wind profiles in the next sections will be shown only up to 500 m.

330 MAE from both runs of both models (Fig. 8) amounted to  $\sim 2 \text{ m s}^{-1}$  within the rotor layer, the largest values  
331 exceeding  $3 \text{ m s}^{-1}$  between 02 and 14 UTC in the EXPR version at Arlington and  $2.5 \text{ m s}^{-1}$  at Boardman. MAE above  
332 200 m increased with height, which again revealed the largest values occurring aloft at Boardman.

333 The models are compared against each other in Figs. 9-10. The new physics and other updates are evaluated in  
334 Fig. 9, which shows the MAE differences between EXPR and CNTR runs of the HRRR and HRRRNEST models,  
335 respectively. Negative values denote MAE reduction (improvement) due to model updates in EXPR. The EXPR version  
336 generally showed improvements of  $0.5\text{-}1.0 \text{ m s}^{-1}$  (5-10%) aloft between 200 and 600 m, in agreement with the 'model-  
337 difference' cross-sections in Olson et al. (2019) based on profile data averaged over the eight 915-MHz Radar Wind  
338 Profilers (WPRs), as described above in Section 2.3. Below 150 m AGL, however, during local nighttime hours of  
339 0300-1200 UTC, the lidar-based cross-sections show that EXPR updates produced decreases in the model skill of  $\sim 1$   
340  $\text{m s}^{-1}$  (up to 10%) at Arlington and Boardman compared to the CNTR, a rotor-layer degradation that was not well  
341 characterized in the RWP cross-sections (Olson et al. 2019). Profiles presented later in Section 3.2.b show that these  
342 low-level decreases in skill occurred during spring and summer. This result is consistent with summertime 80-m-level  
343 reductions in skill during the late afternoon and evening hours seen in Olson et al. (2019), Bianco et al. (2019).

344 The magnitudes of MAE differences between EXPR and CNTR runs of both HRRR and HRRRNEST were  
345 largest within the rotor layer for nighttime periods (03-13 UTC). Differences between EXPR and CNTR (Fig. 9a, c)  
346 were smaller for Wasco than the other two sites and the 3-site composites, indicating that the model-change impacts  
347 were site-dependent. The finer-resolution model, HRRRNEST (Fig. 9b, d) results generally show similar but smaller-  
348 magnitude differences due to the model-physics updates.

349 Model grid-spacing effects are shown in Fig.10. MAE differences between CNTR runs of both models (row  
350 10a) generally indicate that increasing resolution to a 750-m mesh produced improvements of  $\sim 0.5 \text{ m s}^{-1}$ , except at the  
351 surface at night. The EXPR runs (row 10b) mostly show improvements due to the finer resolution. However, the EXPR  
352 model at Wasco showed slight ( $< 0.4 \text{ m s}^{-1}$ ) tendencies to degrade skill for much of the time, and likewise for Arlington  
353 at the surface at night (10-16 UTC).

354 The last row (Fig. 10c) shows the combined effect of improved physics and grid resolution of HRRRNEST over  
355 HRRR. Overall improvement ( $\sim 0.5 \text{ m s}^{-1}$ ) occurred for the nighttime/morning hours (03-18 UTC) in the 100-400-m  
356 layer, similar to the pattern for the CNTR resolution impacts but larger. The combined effect of model physics and  
357 finer grid resolution below 150 m at Arlington and below 50 m at Boardman during nighttime hours was to decrease  
358 skill by  $> 0.5 \text{ m s}^{-1}$ , which was also reflected in the 3-site composites.

359 Overall, even in the annual average, wind speeds showed a strong diurnal modulation, the strongest winds  
360 occurring at night (Fig.8a, Pichugina et al. 2019), and the model errors were also diurnal and largest at night. The  
361 model-difference time-height patterns often displayed a complex and patchy nature, even for the sign of the  
362 improvements. The effects of model updates and finer resolution tended to improve model skill, but the skill was seen  
363 to decrease in certain instances: at levels near the surface at Arlington and Boardman, and comparisons showed  
364 decreased skill most of the time for the finer resolution runs of the HRRR-EXPR through the lowest kilometer at Wasco.  
365 The improvements in model skill were larger as a result of increasing the grid resolution than by implementing the set  
366 of model-physics updates in EXPR. The largest improvements were for the combined updated-physics, EXPR/finer-  
367 resolution run vs. the CNTR/coarser-resolution run ( Fig. 10c).

### 368 3.1.2 Model performance during observed events.

369 Similar time-height cross-section analyses were performed for composites over particular events, including  
370 westerly-gap-flow (Fig. 11) and cold-pool (Fig. 12) days, two major event types that often lasted for several days and  
371 influenced wind-power production. These two event types have a strong influence on the annual wind and model-error  
372 statistics (Pichugina et al. 2019, Banta et al. 2020).

373 The composites of winds during frequent westerly gap flow events (Fig. 11a-c) comprised 46% out of the total  
374 number of events in the 2016 reforecast periods (Fig. 8a-c). Similar to annual averages, both runs of the HRRR captured  
375 the mean diurnal trends of wind speed at each site, but show temporal and vertical discrepancies, which are smoothed  
376 for the 3-site composite. Most notably, both HRRR versions produced the same early onset reduction in wind speeds  
377 after 0500 UTC at Arlington and Boardman that was noted by Pichugina et al. 2019, Wilczak et al. (2019), and Banta  
378 et al. (2020) for the HRRR-NCEP model, traced to poor representation of summertime, thermally forced flows related  
379 to the penetration of a regional sea-breeze into this area. Biases (not shown) from CNTR and EXPR Oz runs of HRRR  
380 ranged from -2.5 to 2.5 m s<sup>-1</sup>, with a slightly larger value (~3 m s<sup>-1</sup>) above 400 m at Boardman. The MAE differences  
381 in row d of Fig. 11 show that the EXPR run reduced the magnitude of the wind-speed discrepancies (negative values,  
382 green colors) above 200 m AGL at Arlington and Boardman somewhat, but had a larger MAE (>2 m s<sup>-1</sup>) than the  
383 CNTR within the rotor layer during nighttime hours at Arlington and (to a lesser degree) at Boardman, indicating that  
384 the updates to the EXPR degraded model skill below 150 m—a pattern that was noted in the *annual* cross-sections of  
385 the previous section. The magnitudes are larger here, though, indicating that the model improvements (+ or -) averaged  
386 over all periods largely reflect how the model handled westerly gap flows. The similarity of these patterns to the annual  
387 ones reinforces the dominance of westerly gap flows in HRRR error statistics as well as the basic wind-speed statistics  
388 (Pichugina et al. 2019).

389 During cold-pool events (Fig. 11a-c), both runs of the model also captured many aspects of wind-speed behavior  
390 at each site and for the composite, but the largest errors were due to the simulated weak-wind layer being too shallow  
391 (Pichugina et al. 2019, also noted by McCaffrey et al. 2019, Olson et al. 2019, and Bianco et al. 2019 using different  
392 data sources) and also to the mistiming of episodes of deepening or shallowing of this layer, which appeared even in  
393 the composites. These effects led to ±3 m s<sup>-1</sup> biases (not shown) with larger values at Boardman. MAE differences  
394 between EXPR and CNTR runs of the model (Fig. 11d) varied between ±1 m s<sup>-1</sup> (negative values again indicating

395 improvements for EXPR). Similar analyses of HRRRNEST (not shown) show smaller MAE for each run and smaller  
396 MAE differences between runs.

397 Time-height cross-section analysis, using a high vertical and temporal resolution of lidar measurements,  
398 provides simultaneous information on both temporal and vertical variability of winds and validation errors, but more  
399 quantitative results can be seen in mean profile and time-series analysis.

### 400 3.2 Mean-profile analysis

#### 401 3.2.1 Annual

402 Annually averaged profiles of measured and modeled wind speed from both runs of HRRR and HRRRNEST along  
403 with the profiles of annual-mean errors are shown in Fig. 13 for each site and the 3-site composites. Both runs of the  
404 HRRR and HRRRNEST under predicted wind speeds below 400 m (column 11a) (except for the HRRR-CNTR run at  
405 Wasco), causing larger values of bias (column 13b) of up to  $\sim 2$  m s<sup>-1</sup> at Arlington and MAE (column 13c) of 2 m s<sup>-1</sup> or  
406 more at all sites. Model-skill impacts due to model-physics updates (column 13d) at Wasco show improvements except  
407 very near the surface, whereas for the other two sites the improvements were seen only above 150 m, as noted in the  
408 time-height cross-sections (Fig. 8). Below that level at these sites, the updates in EXPR generated larger MAE in the  
409 rotor layer of 0.3 m s<sup>-1</sup> annually, as also seen in Fig. 8. Finer model resolution (column 13e) mostly resulted in reduced  
410 errors for the 750-m HRRRNEST compared to the 3-km HRRR model. Exceptions were for the HRRR-EXPR above  
411 100 m at Wasco and the combined physics/resolution comparisons below 100 m at Arlington. The improvements were  
412 largest (0.2-0.3 m s<sup>-1</sup>) for EXPR runs below 200 m at the Arlington and Boardman sites, and were also significant for  
413 the combined impacts.

#### 414 3.2.2 Profiles averaged over seasons and major meteorological events

415 *Seasonal* (Fig.14a, c). Similar analyses of seasonally averaged wind speed errors (not shown here) for each site as well  
416 as for the 3-site composites indicate again that the largest errors for both models occurred below 200 m, except for the  
417 winter season.

418 Seasonal differences due to the EXPR updates (Fig. 14a) show that the improvement above 150 m seen in the  
419 annual profiles (Figs. 8, 13) was also found for each season. In winter, improvement below 150 m resulted largely from  
420 the improvements in the EXPR runs in better representing the cold-pool depth at Wasco, thus correcting the high bias  
421 to the wind speeds there. The large annual degradations seen below 150 m in the 3-site annual average (occurring most  
422 strongly at Arlington and Boardman) are shown here to be due to problems in summer and spring.

423 Going to the finer mesh (Fig. 14c) generally reduced errors above  $\sim 30$  m AGL, except for the EXPR runs during  
424 fall. The largest reductions are seen in the EXPR runs below 150 m in summer and spring, when the finer mesh produced  
425 better simulations of the thermally forced, westerly gap flows.

426 *Major meteorological events* (Fig.14b, d). Results obtained for cold-pool days, frequent during winter months, are  
427 similar to those obtained for the winter season but reduced in magnitude, whereas results for westerly gap flows most  
428 resemble those for spring and summer. Easterly flows, which qualitatively exhibit behavior similar to the wintertime  
429 results, observed over different seasons, show  $\sim 0.4$  m s<sup>-1</sup> improvement due to the combined effect of model physics  
430 and model resolution.

431 **3.3 Hub-height (80-m) wind**432 **3.3.1 Time series analysis**

433 Knowledge of the error in hub-height and rotor-disk wind-speed forecasts is of critical economic importance for  
434 the calculation of energy produced by the wind resource. This section focuses on the evaluation of model skill in  
435 forecasting wind speed at 80 m AGL, at or near hub-height of most wind turbines in the surrounding WFIP2 area.  
436 Figure 15 shows annually-averaged, diurnal time series of wind speed and model validation metrics for the HRRR  
437 CNTR and EXPR runs initialized at 00z, and the changes in model error due to updates in EXPR. Results were similar  
438 for the runs initialized at 12z (not shown here).

439 The bias plots (Fig. 15a, b, second row) show the underestimates of wind speed in the rotor layer noted previously  
440 for Fig. 7. Again the exception is the CNTR run at Wasco, where the speeds were overestimated by more than  $1 \text{ m s}^{-1}$   
441 during nighttime hours—due to issues with the depth of the modeled wintertime cold pools, as discussed. Except for  
442 Wasco, the EXPR had larger negative biases and larger MAE than the CNTR (fourth row), including for the 3-site  
443 composites, consistent with the wind-speed cross-sections (Fig. 8) and profiles (Fig.13).

444 Grid-resolution effects can be seen by comparing the wind-speed and error statistics for (a) HRRR and (b)  
445 HRRRNEST. The improved performance of the finer-meshed models is clear from the smaller magnitudes of the error  
446 values. The high biases at Wasco in the CNTR runs and low biases in EXPR at Arlington are still present, but much  
447 reduced. The smaller-magnitude errors led to smaller-magnitude differences due to EXPR updates (bottom rows).

448 **3.3.2 Summary plots**

449 Annual model-comparison results are summarized in Figure 16 where the percent change in forecast MAE ( $\Delta$ -  
450 MAE) for both models is further broken down into nighttime and daytime hours.

451 *Updates in model physics.* Fig. 16a and b show  $\Delta$ -MAE between CNTR and EXPR runs of the HRRR and  
452 HRRRNEST models due to the *model physics* updates in the EXPR runs. The plot shows how the differences were  
453 larger for the HRRR than the HRRRNEST and larger at night. Improvements are seen at Wasco, especially at night,  
454 but HRRR-EXPR performance was mostly worse than the CNTR's at the other sites and in the 3-site composite. The  
455 magnitudes of the  $\Delta$ -MAEs were smaller for the nested model and these changes were of opposite sign at Wasco and  
456 Arlington, which canceled, resulting in small  $\Delta$ -MAE in the composite.

457 *Model horizontal grid resolution.* Changes in model MAE due to finer-resolution grids are depicted in Fig. 14c,  
458 and d for each model version. All categories (except for Wasco at night) showed reduced error, with the relative  
459 decreases appearing largest for the EXPR version.

460 *Overall  $\Delta$ -MAE.* Changes in model MAE due to updates in model physics and horizontal grid resolution are  
461 illustrated in Fig. 16e, f. The negative  $\Delta$ -MAE values for both initial times imply 2-10% improvements at all three sites  
462 and 3 site composites except for nighttime hours at the Arlington.

463 *Seasons and major events.* The nature of the model errors also changed significantly from season to season and  
464 for different event types. Figure 17 shows the combined physics/resolution impacts of the updates implemented into  
465 HRRRNEST-EXPR runs as compared against HRRR-CNTR, shown for 3-site composites averaged over each season  
466 (Fig. 17a) and each major event (Fig. 17b). Improvement is indicated for all seasons, MAE reductions reaching ~10%

467 during daytime in summer and spring, and during nighttime in winter. All events showed improvement for all hours,  
468 the largest appearing for easterly flows, especially at night. Small degradations are indicated for daytime cold pools  
469 and nighttime gap flows.

470 Power is generated by wind turbines if wind speeds are stronger the cut-in threshold of  $3\text{--}4\text{ m s}^{-1}$  for typical power  
471 curves. Distributions of lidar-measured and modeled 80-m winds (see Appendix C, Fig. 21) and Table 6 shows that  
472 about 40% of wind speeds were less than  $4\text{ m s}^{-1}$ . Although the analysis of the error statistics of wind power generation  
473 beyond the scope of this paper, we illustrate here an example of the power MAE change due to updates in the model  
474 physics, model horizontal grid resolution and overall changes that include all the above updates (Fig. 18). The power  
475 at each site was calculated using a typical power curve (Dupont et al. 2017). A trend of nighttime and daytime power  
476 MAE (Fig 18a-e) is similar to the 80-m wind speed MAE (Fig. 16a-e) but magnitudes are larger than those for wind  
477 speeds as the power is proportional to the cubic of the wind speed in regions of the power curve that are sensitive to  
478 wind speed (International Electrotechnical Commission, 2007). The overall impact from the updates in the model  
479 physics and the horizontal grid resolution on the speed and power  $\Delta$ -MAE is illustrated in Table 2. The larger MAE  
480 improvement is observed at the Wasco sites where winds are much stronger compared to the Boardman site (see  
481 Appendix C, Fig. 21). Thus the power MAE improvement, and even more the power forecast error, depended on the  
482 location of the measurement in this complex-terrain setting.

#### 483 4. Discussion

484 The overall findings here indicate that averaged over the four reforecast periods and the three lidar sites, the  
485 model updates to HRRR-EXP improved model skill above 200 m AGL, but degraded skill in the turbine rotor layer.  
486 Profiles showed that the decreases in skill were significant below 150 m at Arlington and Boardman. In the 3-site  
487 composites, time-height cross-sections and time series indicated that the degradation was strongest at night. These  
488 results contrast to those of Bianco et al. (2019), which found uniform improvement in area-averaged 80-m wind data,  
489 except during evening-transition hours in spring and summer. Measurements from the 19 sodars and three lidars  
490 deployed over the larger WFIP2 study area were averaged together in Bianco et al. (2019) and compared with similarly  
491 averaged output from the various versions of HRRR, as previously described. Calculated error values plotted as time  
492 series and bar graphs mostly showed improvement in HRRR skill as a result of EXPR updates.

493 The three Doppler-lidar sites in the present study were located within the wind-energy corridor of the WFIP2  
494 study area along a line of the prevailing wind direction in the Columbia River Valley (Fig. 1). Previous analyses  
495 (Pichugina et al. 2019, Banta et al. 2020) have shown that model error characteristics and magnitudes can vary  
496 significantly among sites separated by a few tens of kilometers or more in the complex terrain of the WFIP2 region. In  
497 an attempt to reconcile the apparent discrepancies, the error data used in the Bianco et al. (2019) study were plotted for  
498 each measurement site to determine whether horizontal variations in error could be a factor in explaining the different  
499 results between the two studies.

500 Figure 19 shows site-by-site plots indicating which locations saw improvements due to the updates in the  
501 HRRRNEST EXPR and which locations saw decreases in skill compared to the HRRRNEST CNTR. For this plot, bias  
502 difference was broken into three categories: (blue) Improvement ( $\text{EXPR } |\text{bias}| < \text{CNTR } |\text{bias}|$ ), (red): degradation  
503 ( $\text{EXPR } |\text{bias}| > \text{CNTR } |\text{bias}|$ ), and (white) both values were about equal ( $\text{EXPR } |\text{bias}| \approx \text{CNTR } |\text{bias}|$ ). It is immediately

504 obvious even in the sodar data that the sites that saw degradation during winter were low-elevation sites along the river.  
505 In summer, and when averaged over all four reforecast periods, the decreased-skill sites were within the wind-energy  
506 corridor along the river, and some of the locations where skill was improved were outside this area (i. e. sites  
507 abbreviated as YKM, PVE). The Doppler lidars of this study were located along the strip where decreases in skill were  
508 found. Thus, spatial differences in error characteristics do appear to be a factor in the differences in results between the  
509 two studies. Evaluating model improvement by averaging over a wide area makes sense, for example, when measuring  
510 the impact of improvements to a model on power production over a wind power generation area, as the total power  
511 generated by all the turbines in that area generally matters most to the grid operator, and error characteristics at a single  
512 site can be unrepresentative or misleading. However, when attempting to diagnose the sources of model errors, it is  
513 more useful to do so at locations and over areas where the errors are occurring, rather than over large regions where  
514 this error information has been averaged or smoothed out.

515 Forecast degradation at the sodar sites located along the river in Fig. 19 is thus in agreement with the forecast  
516 degradations found by scanning lidars at the ARL, WCO, and BOR sites.

517

## 518 5. Conclusions

519 Doppler lidar measurements at three sites located along the prevalent wind directions in the Columbia River  
520 Basin were used to evaluate the spatial and temporal variability of errors for two configurations of the model: the  
521 'parent' HRRR (3-km horizontal grid spacing) and an experimental, finer-resolution, nested version HRRRNEST (750-  
522 m horizontal grid spacing). Both models were run in control mode (CNTR)- the version available at the beginning of  
523 WFIP2 in September 2015- and experimental mode (EXPR), with the model updates implemented by the end of WFIP2  
524 (March 2017).

525 The evaluation of models was performed using three analysis types: time-height cross-sections of mean wind  
526 speed and model-error statistics, vertical profiles of those quantities, and time series with accompanying summary bar  
527 graphs of 80-m wind speed and error statistics. The results show how the updates in the EXPR versions affected model  
528 skill season by season, site by site, and over periods of atmospheric phenomena relevant to wind energy.

529 The greatest improvements in the HRRR model skill came from reducing the grid interval from 3 km to 750  
530 m. Combining the finer resolution with the EXPR updates produced the best overall improvement statistics, but only  
531 somewhat better than the finer-resolution impacts. These conclusions are based on evaluations of both models using  
532 Doppler-lidar measurements at the three sites located within the WFIP2 study area. The better performance of the  
533 HRRRNEST runs compared to HRRR was found for all sites, seasons, and major atmospheric events.

534 Specifically, we find that:

- 535  The largest values of biases, MAE, RMSE and bias-corrected RMSE were found below 150 m for both runs of  
536 HRRR and HRRRNEST.
- 537  Profiles of validation metrics computed for all reforecast periods (annual) below 200 m show bias error of 1.2 m  
538  $s^{-1}$  and 0.6 m  $s^{-1}$  for HRRR and HRRRNEST, respectively. MAE differences were small for both HRRRNEST  
539 runs and varied between  $-0.2$  and  $+0.2$  m  $s^{-1}$  for HRRR runs (Fig. 17). For the 3-km HRRR, updates in the EXPR  
540 version produced improvements of  $\sim 0.2$  m  $s^{-1}$  during winter but produced decreases in skill (larger errors) in

541 summer and spring. The 750-m HRRRNEST versions were less affected by these updates, as the difference  
542 between EXPR and CNTR was generally less than  $0.05 \text{ m s}^{-1}$  for the nested models.

543  Relative differences in annual 80-m wind speed MAE (Fig. 17) due to the experimental physics (EXPR vs. CNTR),  
544 model horizontal grid resolution (HRRRNEST vs. HRRR) as well as the overall improvement (HRRRNEST EXPR  
545 vs. HRRR CNTR) were largest for nighttime hours and for the westerly wind directions at each site and the 3-site  
546 composites.

547  The biases between measured and modeled winds greatly depended on the location of the instrument (terrain  
548 complexity), the season, and the mean wind speed as illustrated for CNTR and EXPR runs of HRRRNEST (Fig.  
549 18).

550  Reducing the grid interval from 3 km to 750 m produced the greatest improvements in HRRR model skill, for the  
551 model versions tested.

552

553 **Acknowledgments:** The authors thank the WFIP2-experiment participants who aided in the deployment and the  
554 collection of lidar data. A special thanks go to our colleagues Scott P. Sandberg and Ann Weickmann from  
555 NOAA/ESRL/CSL and C. Hocut, Army Research Laboratory for their tremendous work of calibrating and deploying  
556 lidars to the research sites. From NOAA/ESRL we thank Clark King (PSL) for communications with landowners and  
557 obtaining site licenses, Aditya Choukulkar (CSL) for the deployment of lidars, monitoring lidar data in real-time and  
558 providing quality controlled lidar data to the data archive portal (DAP), and Timothy Bonin for developing lidar data  
559 processing techniques to extend vertical coverage. We thank Joe Cline (DOE), Melinda Marquis (NOAA), and Jim  
560 McCaa (Vaisala) for their effort to propose, design, and lead the WFIP2.

561 This work was sponsored by the U.S. Department of Energy, by the Wind Energy Technologies Office and by the  
562 NOAA/ESRL Air Quality Program and Atmospheric Science for Renewable Energy Program.

563 This work was co-authored by the scientist from the National Renewable Energy Laboratory, operated by Alliance for  
564 Sustainable Energy, LLC, for the U.S. Department of Energy (DOE) under Contract DE-AC36-08GO28308. Funding  
565 provided by the U.S. Department of Energy Office of Energy Efficiency and Renewable Energy Wind Energy  
566 Technologies Office. The views expressed in the article do not necessarily represent the views of the DOE or the U.S.  
567 government. The U.S. Government retains and the publisher, by accepting the article for publication, acknowledges  
568 that the U.S. Government retains a nonexclusive, paid-up, irrevocable, worldwide license to publish or reproduce the  
569 published form of this work or to allow others to do so, for U.S. Government purposes.

570 **Appendix A.** Description of the WFIP2 models evaluated in the paper

571 **Appendix B.** Correlation between model outputs of 80 m wind speed extracted at the lidar sites using bi-linear  
572 interpolation or nearest grid point value (Fig. 20).

573 **Appendix C.** The annual distributions of 80-m wind speeds and wind directions at each site (Fig. 21).

574

575 **References**



This is the author's peer reviewed, accepted manuscript. However, the online version of record will be different from this version once it has been copyedited and typeset.

PLEASE CITE THIS ARTICLE AS DOI: 10.1063/5.0009138

- 576 Ascione, A., Cinque, A., Miccadei, E., Villani, F. and Berti, C. 2008: The Plio-Quaternary uplift of the Apennine chain:  
577 New data from the analysis of topography and river valleys in Central Italy, *Geomorphology*, **102**(1), 105–118,  
578 doi:10.1016/j.geomorph.2007.07.022
- 579 Banta, R.M., Y.L. Pichugina, N.D. Kelley, W.A. Brewer, and R.M. Hardesty, 2013: Wind-energy meteorology: Insight  
580 into wind properties in the turbine rotor layer of the atmosphere from high-resolution Doppler lidar. *Bull. Amer.*  
581 *Meteor. Soc.*, **94**, 883-902. DOI:10.1175/BAMS-D-11-00057.1
- 582 Banta, R.M., Y.L. Pichugina, W.A. Brewer, E.P. James, J.B. Olson, S.G. Benjamin, J.R. Carley, L. Bianco, I.V.  
583 Djalalova, J.M. Wilczak, M.C. Marquis, J. Cline, and R.M. Hardesty, 2018: Evaluating and improving NWP  
584 forecasts for the future: How the needs of offshore wind energy can point the way. *Bull. Amer. Meteor. Soc.*, **99**,  
585 1155-1176, doi: 10.1175/BAMS-D-16-0310.1 Banta, R.M., Y.L. Pichugina, W.A. Brewer, A. Choukulkar, K.O.  
586 Lantz, J.B. Olson, J. Kenyon, H.J.S. Fernando, R. Krishnamurthy, M.J. Stoelinga, J. Sharp, L.S. Darby, D.D.  
587 Turner, S. Baidar, and S.P. Sandberg, 2019: Characterizing NWP model errors using Doppler-lidar  
588 measurements of recurrent regional diurnal flows: Marine-air intrusions into the Columbia-River Basin. *Mon.*  
589 *Wea. Rev.*, **148**, 929-953; doi.org/10.1175/MWR-D-19-0188.1
- 590 Banta, R.M., Pichugina Y.L., Brewer W.A., Lundquist J.K., Kelley N.D., Sandberg S.P., Alvarez R.J., Hardesty R.M.,  
591 Weickmann A.M., 2015: 3-D volumetric analysis of wind-turbine wake properties in the atmosphere using high-  
592 resolution Doppler lidar. *J. Atmos. Oceanic Technol.*, **32**: 904–914. doi.org/10.1175/JTECH-D-14-00078.1
- 593 Benjamin, S.G., S.S. Weygandt, J.M. Brown, M. Hu, C. Alexander, T.G. Smirnova, J.B. Olson, E. James, D.C. Dowell,  
594 G.A. Grell, et al., 2016: A North American hourly assimilation and model forecast cycle: The Rapid Refresh.  
595 *Mon. Wea. Rev.*, **144**, 1669-1694; doi: <http://dx.doi.org/10.1175/MWR-D-15-0242.1>.
- 596 Bianco, L., I.V. Djalalova, J.M. Wilczak, J.B. Olson, et al., 2019: Impact of model improvements on 80 m wind speeds  
597 during the second Wind Forecast Improvement Project (WFIP2). *Geosci. Model. Dev.*, **12**, 4803-4821;  
598 doi.org: [10.5194/gmd-12-4803-2019](https://doi.org/10.5194/gmd-12-4803-2019)
- 599 Bonin, T. A., Choukulkar, A., Brewer, W. A., Sandberg, S. P., Weickmann, A. M., Pichugina, Y. L., Banta, R. M.,  
600 Oncley, S. P., and Wolfe, D. E. 2017: Evaluation of turbulence measurement techniques from a single Doppler  
601 lidar. *Atmos. Meas. Tech.*, **10**, 3021–3039, <https://doi.org/10.5194/amt-10-3021-2017>.
- 602 Draxl, C., A.N. Hahmann, A. Pena, and G. Giebel, 2014: Evaluating winds and vertical shear from Weather Research  
603 and Forecasting model forecasts using seven planetary boundary layer schemes. *Wind Energy*, **17**, 39-55.  
604 doi.org/10.1002/we.1555.
- 605 Draxl, Berg, Bianco, Bonin, Choukulkar, Clifton, Cline, Djalalova, Ghate, Gritmit, Holub, Kenyon, Lantz, Long,  
606 Lundquist, McCaa, McCaffrey, Newman, Olson, Pichugina, Sharp, Shaw, Smith, and Toy, 2019: The  
607 Verification and Validation Strategy Within the Second Wind Forecast Improvement Project (WFIP 2). *National*  
608 *Renewable Energy Laboratory Report* www.nrel.gov/publications.
- 609 Draxl, C., R. Worsnop, G. Xia, D. Chand, J. K. Lundquist, Y. Pichugina, J. Sharp, G. Wedam, J. Wilczak, and L.  
610 Berg: 2020, Mountain waves impact wind power generation, submitted to Wind Energy Science.
- 611 Drechsel, S., G.J. Mayr, J.W. Messner, and R. Stauffer, 2012: Lower boundary wind speeds: Measurements and  
612 verification of forecasts. *J. Appl. Meteor. Climatol.*, **51**, 1602-1617, doi.org/10.1175/JAMC-D-11-0247.1

This is the author's peer reviewed, accepted manuscript. However, the online version of record will be different from this version once it has been copyedited and typeset.

PLEASE CITE THIS ARTICLE AS DOI: 10.1063/5.0009138

- 613 Dupont, Elise & Koppelaar, Rembrandt & Jeanmart, Hervé. (2017). Global available wind energy with physical and  
614 energy return on investment constraints. *Applied Energy*. 10.1016/j.apenergy.2017.09.085.
- 615 International Electrotechnical Commission, 2007: Wind turbines - Part 12-1: Power performance measurements of  
616 electricity producing wind turbines. IEC 61400-12-1, 90 pp.
- 617 Fast J.D., and L.S. Darby. 2004. "An Evaluation of Mesoscale Model Predictions of Down-Valley and Canyon Flows  
618 and Their Consequences Using Doppler Lidar Measurements During VTMX 2000." *Journal of Applied  
619 Meteorology* 43, no. 3:420-436.
- 620 Fitch, A. C., J. B. Olson, J. K. Lundquist, J. Dudhia, A. K. Gupta, J. Michalakes, and I. Barstad, 2012: Local and  
621 Mesoscale Impacts of Wind Farms as Parameterized in a Mesoscale NWP Model. *Mon. Weather Rev.*, **140**,  
622 3017–3038, <https://doi.org/10.1175/MWR-D-11-00352.1>.
- 623 Lundquist, J.K., DuVivier, K.K., Kaffine, D. et al. Costs and consequences of wind turbine wake effects arising from  
624 uncoordinated wind energy development. *Nat Energy* **4**, 26–34 (2019). [https://doi.org/10.1038/s41560-018-](https://doi.org/10.1038/s41560-018-0281-2)  
625 [0281-2](https://doi.org/10.1038/s41560-018-0281-2)
- 626 Krogseter, O., and J. Reuder, 2015: Validation of boundary layer parameterization schemes in the weather research  
627 and forecasting model under the aspect of offshore wind energy applications—Part I: Average wind speed and  
628 wind shear. *Wind Energy*, **18**, 769-782.
- 629 McCaffrey, K., J.M. Wilczak, L. Bianco, E. Gritmit, J. Sharp, R. Banta, K. Friedrich, H.J.S. Fernando, R.  
630 Krishnamurthy, L. Leo, and P. Muradyan, 2019: Identification and characterization of persistent cold pool  
631 events from temperature and wind profilers in the Columbia River Basin. *J. Appl. Meteor. Climatol.*, **58**, 2533–  
632 2551; doi.org/10.1175/JAMC-D-19-0046.1
- 633 Olson, J.B., J.S. Kenyon, I. Djalalova, L. Bianco, D.D. Turner, Y. Pichugina, A. Choukulkar, M.D. Toy, J.M. Brown,  
634 W.M. Angevine, E. Akish, J.-W. Bao, P. Jimenez, B. Kosovic, K.A. Lundquist, C. Draxl, J.K. Lundquist, J.  
635 McCaa, K. McCaffrey, K. Lantz, C. Long, J. Wilczak, R. Banta, M. Marquis, S. Redfern, L.K. Berg, W. Shaw,  
636 and J. Cline, 2019: Improving wind energy forecasting through numerical weather prediction model  
637 development. *Bull. Amer. Meteor. Soc.*, **100**, 2201-2220; doi.org/10.1175/BAMS-D-18-0040.1
- 638 Pichugina, Y. L., R.M. Banta, J.B. Olson, J.R. Carley, M.C. Marquis, W.A. Brewer, J.M. Wilczak, I. V. Djalalova, L.  
639 Bianco, E.P. James, S.G. Benjamin, and J. Cline, 2017: Assessment of NWP forecast models in simulating  
640 offshore winds through the lower boundary layer by measurements from a ship-based scanning Doppler lidar.  
641 *Monthly Weather Review*, vol. **145**, no. 10, 4277-4301 doi: [10.1175/MWR-D-16-0442.1](https://doi.org/10.1175/MWR-D-16-0442.1)
- 642 Pichugina, Y.L., R.M. Banta, and Coauthors, 2019: Spatial variability of winds and HRRR-NCEP model error  
643 statistics at three Doppler-lidar sites in the wind-energy generation region of the Columbia River Basin. *J.  
644 Appl. Meteor. Climatol.*, **58**, 1633-1656. doi.org/10.1175/JAMC-D-11-040.1
- 645 Rajewski, D.A., E.S. Takle, J.K. Lundquist, S. Oncley, J.H. Prueger, T.W. Horst, M.E. Rhodes, R. Pfeiffer, J.L.  
646 Hatfield, K.K. Spoth, and R.K. Doorenbos, 2013: Crop Wind Energy Experiment (CWEX): Observations of  
647 Surface-Layer, Boundary Layer, and Mesoscale Interactions with a Wind Farm. *Bull. Amer. Meteor. Soc.*,  
648 **94**, 655–672, <https://doi.org/10.1175/BAMS-D-11-00240>.

This is the author's peer reviewed, accepted manuscript. However, the online version of record will be different from this version once it has been copyedited and typeset.

PLEASE CITE THIS ARTICLE AS DOI: 10.1063/5.0009138

- 649 Redfern, S., J. B. Olson, J. K. Lundquist, C. T. M. Clack, 2019, Incorporation of the Rotor-Equivalent Wind Speed  
650 into the Weather Research and Forecasting model's Wind Farm Parameterization. *Monthly Weather Review*  
651 **147**, 1029-1046.
- 652 Schroeder, Paul, W. Alan Brewer, Aditya Choukulkar, Ann Weickmann, Michael Zucker, Maxwell Holloway, Scott  
653 Sandberg. 2019: A compact, flexible, and robust micro pulsed Doppler Lidar. *Journal of Atmospheric and*  
654 *Oceanic Technology*, in peer review.
- 655 Sharp, J., & Mass, C. (2002). Columbia Gorge gap flow: Insights from observational analysis and ultra-high-resolution  
656 simulation. *Bulletin of the American Meteorological Society*, *83*(12), 1757-1762.
- 657 Sharp, J. and C.F. Mass, 2004: Columbia Gorge Gap Winds: Their Climatological Influence and Synoptic Evolution.  
658 *Wea. Forecasting*, **19**, 970-992, <https://doi.org/10.1175/826.1>
- 659 Shaw, W.J., L.K Berg, J. Cline, C. Draxl, E. Gritmit, J.K. Lundquist, M. Marquis, J. McCaa, J. Olson, C. Sivaraman, J.  
660 Sharp, J. Wilczak, 2019: The Second Wind Forecast Improvement Project (WFIP 2): General overview. *Bull.*  
661 *Amer. Meteor. Soc.*, 100, 1687-1699; [doi.org/10.1175/BAMS-D-18-0036.1](https://doi.org/10.1175/BAMS-D-18-0036.1)
- 662 Skamarock, W. C., and Coauthors, 2008: A description of the Advanced Research WRF version 3. NCAR Tech. Note  
663 NCAR/TN-475+STR, 113 pp., <https://doi.org/10.5065/D68S4MVH>. Siedersleben, S. K., J. K. Lundquist, A.  
664 Platis, A. Lampert, K. Bärfuss, B. Cañadillas, B. Djath, J. Schulz-Stellenfleth, T. Neumann, J. Bange, S.  
665 Emeis, 2018, Micrometeorological Impacts of Offshore Wind Farms as seen in Observations and Simulations,  
666 *Environmental Research Letters* **13**, 124012.
- 667 Siedersleben, S. K., Platis, A., Lundquist, J. K., Djath, B., Lampert, A., Bärfuss, K., Cañadillas,  
668 B., Schulz-Stellenfleth, J., Bange, J., Neumann, T., and Emeis, S.: Turbulent kinetic energy  
669 over large offshore wind farms observed and simulated by the mesoscale model WRF (3.8.1), *Geosci. Model*  
670 *Dev.*, **13**, 249-268, <https://doi.org/10.5194/gmd-13-249-2020>, 2020
- 671 Whiteman, C. D., S. Zhong, W. J. Shaw, J. M. Hubbe, X. Bian, and J. Mittelstadt, 2001: Cold pools in the Columbia  
672 Basin, *Wea. Forecasting*, **16**, 432-447, [doi:10.1175/1520-0434\(2001\)016<0432:CPITCB.2.0.CO;2](https://doi.org/10.1175/1520-0434(2001)016<0432:CPITCB.2.0.CO;2).
- 673 Wilczak, J.M., M. Stoelinga, L.K. Berg, J. Sharp, C. Draxl, K. McCaffrey, R.M. Banta, L. Bianco, I. Djalalova, J.K.  
674 Lundquist, P. Muradyan, A. Choukulkar, L. Leo, T. Bonin, Y. Pichugina, R. Eckman, C.N. Long, K. Lantz,  
675 R.P. Worsnop, J. Bickford, N. Bodini, D. Chand, A. Clifton, J. Cline, D.R. Cook, H.J.S. Fernando, K.  
676 Friedrich, R. Krishnamurthy, M. Marquis, J. McCaa, J.B. Olson, S. Otarola-Bustos, G. Scott, W.J. Shaw, S.  
677 Wharton, A.B. White, 2019: The Second Wind Forecast Improvement Project (WFIP2): Observational field  
678 campaign. *Bull. Amer. Meteor. Soc.*, **100**, 1701-1723; [doi.org/10.1175/BAMS-D-18-0035.1](https://doi.org/10.1175/BAMS-D-18-0035.1)
- 679 Yang, B., Y. Qian, L. K. Berg, P. L. Ma, S. Wharton, V. Bulaevskaya, H. Yan, Z. Hou, and W. J. Shaw, 2017:  
680 Sensitivity of turbine-height wind speeds to parameters in planetary boundary-layer and surface-layer schemes  
681 in the weather research and forecasting model. *Bound.-Layer Meteor.*, **162**, 117-142. doi: [10.1007/s10546-](https://doi.org/10.1007/s10546-016-0185-2)  
682 [016-0185-2](https://doi.org/10.1007/s10546-016-0185-2).
- 683 Zhong, S., and J. D. Fast, 2003: An evaluation of the MM5, RAMS, and Meso-Eta models at subkilometer resolution  
684 using field campaign data in the Salt Lake Valley. *Mon. Wea. Rev.*, **131**, 1301-1322.

This is the author's peer reviewed, accepted manuscript. However, the online version of record will be different from this version once it has been copyedited and typeset.

PLEASE CITE THIS ARTICLE AS DOI: 10.1063/5.0009138

685 Zhong, S., C. D. Whiteman, X. Bian, W. J. Shaw, and J. M. Hubbe, 2001: Meteorological processes affecting the  
 686 evolution of a wintertime cold-air pool in the Columbia Basin. *Mon. Wea. Rev.*, **129**, 2600–2613.

687 **Data Availability Statement**

AVAILABILITY OF DATA	DATA AVAILABILITY STATEMENT
Data generated at a central, large scale Facility: NOAA Meteorological Assimilation Data Ingest System (MADIS)	The information on instrument metadata such as location, dates of deployment, data-processing methods including time averaging, whether the data was transferred to the MADIS and whether the data were assimilated in real-time into developmental versions of the Rapid Refresh (RAP) and High Resolution Rapid Refresh (HRRR) models run at NOAA/ESRL can be found at <a href="https://madis.noaa.gov/support_overview.shtml">https://madis.noaa.gov/support_overview.shtml</a>
Data openly available in a public repository that does not issue DOIs	The data that support the findings of this study are openly available in Data Archive and Portal (DAP), <a href="https://a2e.energy.gov/data">https://a2e.energy.gov/data</a> The DAP establishes a sustained data management structure with protocols and access to assure massive datasets resulting from A2e (Atmosphere to Electrons) efforts will have the quality needed for scientific discovery and portals required to make data available to a broad stakeholder group. The DAP will collect, store, catalog, process, preserve, and disseminate all significant A2e data—and ultimately all historical wind data supported by the U.S. Department of Energy’s Office of Energy Efficiency and Renewable Energy—with state-of-the-art technology while conforming to or defining new industry data standards
Real-time and quality controlled data from scanning Doppler lidars in available on DAP and on request from the authors	During WFIP2 two scanning, pulsed Leosphere WindCube 200S Doppler lidar systems continuously from September 2015 to April 2017 and the third scanning Doppler lidar, a Halo Streamline XR continuously operated from January through December 2016. In addition to DAP, real-time lidar measurements, as well as data processing products, can be found at <a href="https://www.esrl.noaa.gov/csd/groups/csd3/measurements/wfip2/">https://www.esrl.noaa.gov/csd/groups/csd3/measurements/wfip2/</a>
Data available on request due to privacy/ethical restrictions:	Power generation data.  The data that support the findings of this study are available from the Bonneville Power Authority (BPA) balancing area. Restrictions apply to the availability of these data, which were used under license for this study. Data are available from the authors upon reasonable request and with the permission of BPA. Data on wind power generation within the BPA can be found here <a href="https://transmission.bpa.gov/Business/Operations/Wind/twndbspt.aspx">https://transmission.bpa.gov/Business/Operations/Wind/twndbspt.aspx</a>

688 **Table Captions**

689 Table 1. The number of days (#) having observed event types during reforecast periods in 2016, 12 months of concurrent  
 690 Doppler lidar measurements in 2016, and 18 months of the WFIP2 experiment. Occurrence (%) of a particular event  
 691 type during each period relative to the total occurrence of events.

692 Table. 2. The overall impact of the updates in model physics and horizontal grid resolution on wind speed and power  
 693  $\Delta$ -MAE.

This is the author's peer reviewed, accepted manuscript. However, the online version of record will be different from this version once it has been copyedited and typeset.

PLEASE CITE THIS ARTICLE AS DOI: 10.1063/5.0009138

694 Table 3. Observed 80-m mean wind speed and Bias of HRRR and HRRRNEST CNTR and EXPR runs during the  
695 WFIP2 reforecast period (February 2016-March 2017) at 23 sites. The first three columns show site ID, site elevation  
696 above sea level (ASL, m), and terrain complexity expressed as standard deviation (STD) of the elevation within 3 km  
697 circle around each site.

698 Table 4. Statistics of the correlation between model outputs of 80 m wind speed extracted at the lidar sites using bi-  
699 linear (Bi) interpolation or nearest grid point (N) value.

700 Table 5. Mean values for distributions of 80 m wind speed and direction from Fig. 21

701 Table 6. Percent of wind speeds in each region of a power curve of a typical wind turbine.

702 Table 7. Summary of the HRRR and HRRRNEST reforecast configurations.

703 Table 8. Description of the control and experimental physics configurations used in the reforecasts (adapted from  
704 Table 2 in Olson et al. 2019), where model developments in support of WFIP2 are shown in bold. All components  
705 not under development in WFIP2 (regular font) are described in Benjamin et al. (2016).

#### 706 **Figure Captions**

707 Figure 1. (a) Map of the Columbia River Valley with the location of scanning Doppler lidars denoted by gold-filled  
708 circles. Red circles indicate the highest peaks of the Cascade Mountains. (b) Google Earth detailed map of the study  
709 area shows the location of two NOAA Doppler scanning lidars (200S) at Wasco (452 m ASL) and Arlington (262 m  
710 ASL). The Notre Dame University Halo Streamline XR lidar is located at the Boardman site at 110 m ASL. The  
711 white line indicates the east-west transect of the study region along the prevalent wind directions observed from  
712 surface measurements and models during previous studies in this area and confirmed from the analysis of Doppler  
713 lidar measurements in Pichugina et al. (2019). The surrounding wind turbines (total rated capacity of ~3,800 MW)  
714 are indicated by the clusters of dark yellow circles. An elevation gradient along the transect line is shown in (c).

715 Figure 2. (a) Domains of WFIP2 (green) HRRR and HRRRNEST models are shown along with the operational (white)  
716 RAP (13-km grid spacing) and (red) HRRR-NCEP (3-km grid spacing) models. (Fig. 2a adapted from Olson et al.  
717 2019). (b) An example of HRRRNEST-modeled wind flow at 80 m superimposed on area topography from WRF V3.7.  
718 The example is taken from a 7-h forecast initialized at 000UTC on 15 May 2016. Locations of Doppler lidars are shown  
719 by black circles. (c) Maps of the terrain elevations (in meters) at Wasco, Arlington, and Boardman research sites. The  
720 location of each lidar (dark yellow triangles) is shown relative to the HRRR 3-km model corners of the grid cells (red  
721 circles), and relative to the HRRRNEST 750-m model corners of the grid cells (white circles).

722 Figure 3. Atmospheric events observed over the WFIP2 research area from the analysis of models, satellites, and all  
723 available ground observations. (a) The number of events observed during 18 months of the experiment, 12 months of  
724 2016, and reforecast periods in 2016 shown by colors according to the legend. Multiple events can occur on the same  
725 day. (b) Relative number (%) of major events in each month observed during the reforecast periods.

726 Figure 4. Time-height cross-sections of wind speed and wind direction at the (from top to bottom) Wasco, Arlington,  
727 and Boardman site during atmospheric phenomena observed in the WFIP2 area: (a) Cold pool, (b) Westerly Gap Flow,  
728 (c) Easterly Gap Flow, and (d) Mountain Waves. Wind speed is color-coded from 0 to 15 m s<sup>-1</sup> according to the color

This is the author's peer reviewed, accepted manuscript. However, the online version of record will be different from this version once it has been copyedited and typeset.

PLEASE CITE THIS ARTICLE AS DOI: 10.1063/5.0009138

729 scale at the top of each panel. Black arrows show wind direction. Two white horizontal lines on each panel indicate  
730 typical rotor-disk height, 50-150 m AGL.

731 Figure 5. Time-height cross-sections of wind speed averaged over all days in 2016 with associated atmospheric  
732 phenomena: (from left to right) Cold pool; Westerly Gap flow, and Easterly Gap Flow. Event-averaged wind speed is  
733 shown for each site: (a) Wasco, (b) Arlington, (c) Boardman, and (d) for 3-site composites. Wind speeds are color-  
734 coded according to the color scale shown for each event on the top of this figure.

735 Figure 6. Time series of (a, d) 80-m wind speed observed at the 3 lidar sites and (b, e) wind power computed by  
736 normalized power curve during a westerly gap flow/marine intrusion event on 13-18 August 2016, and cold pool event  
737 on 07-12 February 2016. (c, f) Total power generation over the Bonneville Power Authority (BPA) area during these  
738 periods. The bottom row shows distributions of wind speed and wind directions for the (g, h) August and (i, j) February  
739 cases. Different colors indicate each site according to the legends.

740 Figure 7. Time-height cross-sections of annual-mean wind speed from (a) lidar, (b) HRRR CNTR run, and (c) HRRR  
741 EXPR run for each site (from left to right columns: Wasco, Arlington, and Boardman), and for the 3-site composites.  
742 Two bottom rows show the wind speed difference (bias) between (d) HRRR CNTR run and lidar, and (e) HRRR EXPR  
743 run and lidar, expressed as HRRR minus lidar-measured values. White lines indicate 50 m and 150 m AGL

744 Figure 8. Annual statistics: same as Fig. 7d-e but for MAE from (a, b) HRRR CNTR and EXPR runs, (c, d)  
745 HRRRNEST CNTR and EXPR runs. All panels are shown for 00z runs of both models; 12z runs were similar.

746 Figure 9. Annual MAE differences due to changes in model physics and other updates (EXPR-CNTR) made in (a)  
747 HRRR and (b) HRRRNEST. Bottom two rows (c, d) show these differences expressed as percentages, normalized by  
748 mean, lidar-measured wind speeds.

749 Figure 10. Annual MAE differences due to changes in model horizontal spacing (HRRRNEST-HRRR) for (a) CNTR  
750 and (b) EXPR runs of models. The bottom row (c) shows MAE difference due to combined effects of changes in model  
751 physics and horizontal spacing.

752 Figure 11. Time-height cross-sections of wind speed from lidar, HRRR CNTR, and HRRR EXPR 00z runs averaged  
753 over (a-c) westerly gap flow. The bottom row (d) shows the MAE difference between EXPR and CNTR runs. Columns  
754 are shown for (from left to right) Wasco, Arlington, Boardman sites, and 3-site composites.

755 Figure 12. Same as Fig. 11 but composited over cold-pool events.

756 Figure 13. Annual profiles of wind speed and validation metrics are shown for the (from top to bottom), Wasco,  
757 Arlington, and Boardman sites, and the 3-site composites. (a) Measured wind speed is shown by a black solid line, and  
758 the (a-c) CNTR and EXPR runs are shown by red and blue colors for (solid) HRRR and (dashed) HRRRNEST  
759 according to the legend at the top left panel. (d) MAE improvement due to model physics: error differences ( $\text{m s}^{-1}$ )  
760 between EXPR and CNTR runs of (black) HRRRNEST and (gray) HRRR models for (solid) MAE, (dashed) RMSE,  
761 and (dotted) bias-corrected RMSE (RMSEu). (e) MAE improvement due to finer resolution in the (red) CNTR runs  
762 (HRRRNEST CNTR – HRRR CNTR) of both models, and (blue) finer resolution in the EXPR runs (HRRRNEST

This is the author's peer reviewed, accepted manuscript. However, the online version of record will be different from this version once it has been copyedited and typeset.

PLEASE CITE THIS ARTICLE AS DOI: 10.1063/5.0009138

763 EXPR – HRRR EXPR), and the (black) total effect of physics and resolution (HRRRNEST EXPR – HRRR CNTR).  
 764 Negative values mean improvement.

765 Figure 14. (a-b) 3-site composite profiles of error differences ( $\text{m s}^{-1}$ ) between EXPR and CNTR runs of (black)  
 766 HRRRNEST and (gray) HRRR models: (solid) MAE, (dashed) RMSE, and (dotted) bias-corrected RMSE (RMSEu).  
 767 Error differences are shown for (a) calendar seasons and (b) four major events. (c-d) MAE differences due to (red) finer  
 768 resolution in the CNTR runs (HRRRNEST CNTR – HRRR CNTR), and (blue) finer resolution in the EXPR runs  
 769 (HRRRNEST EXPR – HRRR EXPR). The total effect of improved physics and model resolution (HRRRNEST EXPR  
 770 – HRRR CNTR) is shown by black lines. Improvements are shown for (c) calendar seasons and (d) four major events.  
 771 Negative values mean improvement.

772 Figure 15. Time-series of 80-m annual (15a from top to bottom) winds speed, BIAS, MAE, and the difference in  
 773 validation metrics between EXPR and CNTR runs of HRRR initialized at 00z.

774 Mean values in the top three panels are from (black) lidar measurements, and the (red) CNTR and (blue) EXPR runs.  
 775 Horizontal dashed lines of the corresponding color represent mean values of Bias and MAE from both runs further  
 776 averaged over the diurnal cycle. Black lines on the bottom panels show the difference between two runs (EXPR-CNTR)  
 777 for (solid) RMSE, (dashed) unbiased RMSE, and (dotted) MAE according to the legend at the top right corner. Fig.  
 778 15b is the same as Fig. 15a, except for HRRRNEST.

779 Figure 16. Relative differences in annual 80-m wind speed MAE ( $\Delta$ -MAE, in %) due to the (a, b) experimental physics  
 780 and (c, d) model horizontal grid resolution at each site and 3-site composites, (e) the overall (physics + resolution)  $\Delta$ -  
 781 MAE for initial time 0z, (f) same as (e) but for the initial time 12z. Each panel shows  $\Delta$ -MAE for (gray) data averaged  
 782 for all hours, (dark blue) nighttime, and (dark yellow) daytime hours. Nighttime and daytime hours for the initial time  
 783 0z (Fig. 16 a-e) are 0300-1200 UTC. Nighttime and daytime hours for the initial time 12z (Fig. 16 f) are 00-1200 UTC  
 784 and 1500-2400 UTC. The  $\Delta$ -MAEs were computed as follow: (a)  $[\text{HRRR EXPR} - \text{HRRR CNTR}] / \text{HRRR CNTR}$ ; (b)  
 785  $[\text{HRRRNEST EXPR} - \text{HRRRNEST CNTR}] / \text{HRRRNEST CNTR}$ ; (c)  $[\text{HRRRNEST CNTR} - \text{HRRR CNTR}] / \text{HRRR}$   
 786  $\text{CNTR}$ ; (d)  $[\text{HRRRNEST EXPR} - \text{HRRR EXPR}] / \text{HRRR EXPR}$ ; (e-f)  $[\text{HRRRNEST EXPR} - \text{HRRR CNTR}] / \text{HRRR}$   
 787  $\text{CNTR}$ . The negative values at each panel imply improvement.

788 Figure 17. The combined physics/horizontal grid resolution relative  $\Delta$ -MAE for 3-site composites of 80-m winds  
 789 averaged over (a) each season and (b) major event types. Combined relative MAE defined as  $[\text{HRRRNEST EXPR} -$   
 790  $\text{HRRR CNTR}] / \text{HRRR CNTR}$ .

791 Figure 18. Same as Fig. 16 a-e but for the power MAE computed by using 80 m wind speed measured by lidar and  
 792 predicted by CNTR and EXPR runs of HRRR and HRRRNEST for 0z initial time.

793 Figure 19. Maps of the terrain overlapped with the bias difference (colored circles) between HRRRNEST EXPR and  
 794 CNTR runs (Bianco et al. 2019) at the locations of 19 sodars and 3 different types of lidars as described in the text.  
 795 The bias difference is shown in three categories according to the legend on each map. Sites, where the absolute value  
 796 of the bias from EXPR runs, is smaller (larger) than from the CNTR runs indicated some improvement (degradation)  
 797 in model physics are shown correspondingly by blue (red) circles and indicated in the legend as “Yes” (“No”). Sites,

This is the author's peer reviewed, accepted manuscript. However, the online version of record will be different from this version once it has been copyedited and typeset.

PLEASE CITE THIS ARTICLE AS DOI: 10.1063/1.50009138

798 where biases from CNTR and EXPR runs are almost equal, are indicated by yellow and “0” in the legend. Sites where  
799 observed or modeled data were not available (no data) are indicated by white circles. Maps are shown for mean values  
800 over reforecast periods in the (a) winter, (b) summer seasons, and (c) all four-seasons of WFIP2.

801 Figure 20. Scatter plots between modeled of 80-m wind speed extracted at the lidar sites using bi-linear interpolation  
802 or nearest grid point value: (a) for HRRRNEST (750 m horizontal grid) and (b) HRRR (3 km horizontal grid) models.  
803 Red and blue points on all panels represent CNTR and EXPR runs respectively.

804 Figure 21. The annual distributions of 80-m wind speeds and wind directions at each site are shown for (red) control  
805 and (blue) experimental runs of (a) HRRR and (b) HRRRNEST models. Lidar-measured variables are shown by black  
806 curves at each panel. Gray shaded areas indicate wind speeds (4-12 m s<sup>-1</sup>) in a non-rated region of a typical wind turbine  
807 power curve (Dupont et al. 2017).

808 **Tables with Captions**

809 Table 1. The number of days (#) having observed event types during reforecast periods in 2016, 12 months of concurrent  
810 Doppler lidar measurements in 2016, and 18 months of the WFIP2 experiment. Occurrence (%) of a particular event  
811 type during each period relative to the total occurrence of events.

	Cold Pool		W-Gap Flow		E-Flow		Mount. Wakes		Topo. Wakes		CO		Other		Total
	#	%	#	%	#	%	#	%	#	%	#	%	#	%	
<b>WFIP2</b>	136	17	339	43	92	12	90	11	80	10	12	2	39	5	788
<b>2016</b>	64	13	237	47	57	11	63	13	55	11	9	2	21	4	506
<b>Refcst</b>	22	9	110	46	26	11	33	14	27	11	5	2	16	7	239

812



This is the author's peer reviewed, accepted manuscript. However, the online version of record will be different from this version once it has been copyedited and typeset.

PLEASE CITE THIS ARTICLE AS DOI: 10.1063/5.0009138

813 Table. 2. The overall impact of the updates in model physics and horizontal grid resolution on wind speed and power  
814  $\Delta$ -MAE.

	Wasco		Arlington		Boardman		3 sites	
	<i>Speed</i>	<i>Power</i>	<i>Speed</i>	<i>Power</i>	<i>Speed</i>	<i>Power</i>	<i>Speed</i>	<i>Power</i>
<b>All</b>	-7.13	-13.71	-1.35	-9.11	-5.61	-7.01	-4.76	-10.59
<b>Nighttime</b>	-10.65	-15.44	2.06	-4.43	-6.85	-6.17	-5.31	-9.02
<b>Daytime</b>	-3.81	-12.14	-4.58	-13.35	-4.43	-7.78	-4.23	-12.02

815

This is the author's peer reviewed, accepted manuscript. However, the online version of record will be different from this version once it has been copyedited and typeset.

PLEASE CITE THIS ARTICLE AS DOI: 10.1063/1.50009138

816 Table 3. Observed 80-m mean wind speed and Bias of HRRR and HRRRNEST CNTR and EXPR runs during the  
817 WFIP2 reforecast period (February 2016-March 2017) at 23 sites. The first three columns show site ID, site elevation  
818 above sea level (ASL, m), and terrain complexity expressed as standard deviation (STD) of the elevation within 3 km  
819 circle around each site.

Site ID	Elev. (m)	Terrain std (m)	Instrument	Obs Speed (m s <sup>-1</sup> )	Bias (m s <sup>-1</sup> )			
					CNT 3 km	EXP 3 km	CNT 750 m	EXP 750 m
AO1	706	64	sodar	5.67	0.069	-0.111	0.05	0.015
AO2	356	13	sodar	6.04	-0.009	-0.195	-0.04	-0.087
AO3	116	12	sodar	4.78	-0.164	-0.324	-0.183	-0.209
AO4	432	34	sodar	6.04	0.145	-0.063	0.048	-0.039
AO5	456	13	sodar	6.3	0.125	-0.048	0.015	-0.043
AO6	731	81	sodar	6.85	-0.025	-0.151	-0.053	-0.075
AO7	166	55	sodar	4.78	0.078	-0.133	0.157	0.067
AO8	703	98	sodar	4.43	-0.148	-0.183	0.106	0.084
AO9	836	57	sodar	2.47	0.84	0.59	0.8	0.681
ARL	266	56	200S	4.78	-0.133	-0.276	-0.144	-0.214
BOR	112	6	sodar	4.78	-0.092	-0.248	-0.091	-0.14
CDN	891	25	sodar	6.17	0.013	-0.102	-0.008	-0.032
DCR	795	26	sodar	5.35	0.185	0.02	0.108	0.084
GDL	501	16	sodar	4.32	0.234	0.112	0.039	0.042
GDR	725	81	WindCube	7.19	-0.067	-0.18	-0.078	-0.1
PVE	991	42	sodar	4.16	0.152	-0.026	0.144	0.135
RFS	62	80	sodar	4.78	0.095	-0.083	-0.026	-0.062
RTK	708	19	sodar	5.02	0.29	0.156	0.188	0.181
VCR	542	69	ZephIR	7.13	-0.098	-0.255	-0.067	-0.112
WCO	462	25	sodar	6.67	0.07	-0.108	-0.027	-0.082
WWL	382	34	sodar	4.18	0.114	-0.109	0.082	0.051
YKM	330	19	sodar	2.82	0.213	0.095	0.109	0.102
AO1	706	64	sodar	5.67	0.069	-0.111	0.05	0.015

820

This is the author's peer reviewed, accepted manuscript. However, the online version of record will be different from this version once it has been copyedited and typeset.

PLEASE CITE THIS ARTICLE AS DOI: 10.1063/1.50009138

821 Table 4. Statistics of the correlation between model outputs of 80 m wind speed extracted at the lidar sites using bi-  
822 linear (Bi) interpolation or nearest grid point (N) value.

Site	Model	R <sup>2</sup>	intercept	slope	Mean Bi	STD Bi	Mean N	STD N	Speed diff
<b>HRRRNEST</b>									
<i>CNTR</i>									
<i>Wasco</i>		0.99	0.06	0.99	6.88	3.82	6.93	3.82	-0.05
<i>Arlington</i>		0.99	0.08	1.02	5.73	3.57	5.91	3.65	-0.19
<i>Boardman</i>		0.99	0.05	1.00	5.48	3.86	5.53	3.86	-0.05
<i>EXPR</i>									
<i>Wasco</i>		0.99	0.05	1.00	6.53	3.71	6.58	3.73	-0.06
<i>Arlington</i>		0.99	0.06	1.03	5.24	3.32	5.46	3.43	-0.22
<i>Boardman</i>		0.99	0.04	1.00	5.16	3.57	5.20	3.57	-0.04
<b>HRRR</b>									
<i>CNTR</i>									
<i>Wasco</i>		0.99	0.03	0.99	7.03	3.84	7.00	3.82	0.03
<i>Arlington</i>		0.99	0.02	0.97	5.71	3.55	5.55	3.46	0.16
<i>Boardman</i>		0.99	-0.04	1.02	5.16	3.69	5.22	3.76	-0.06
<i>EXPR</i>									
<i>Wasco</i>		0.99	0.02	1.00	5.98	3.38	6.00	3.39	-0.02
<i>Arlington</i>		0.99	-0.05	1.00	4.56	2.76	4.49	2.76	0.06
<i>Boardman</i>		0.99	-0.04	1.01	4.32	2.98	4.31	3.01	0.01

823

This is the author's peer reviewed, accepted manuscript. However, the online version of record will be different from this version once it has been copyedited and typeset.

PLEASE CITE THIS ARTICLE AS DOI: 10.1063/5.0009138

824 Table 5. Mean values for distributions of 80 m wind speed and direction from Fig. 21

Site		Westerly flows				Easterly flows			
		HRRRNEST		HRRR		HRRRNEST		HRRR	
		Speed	Dir	Speed	Dir	Speed	Dir	Speed	Dir
Wasco	<i>Lidar</i>	7.7	270.5	7.9	271.0	4.1	92.4	4.2	91.5
	<i>CNTR</i>	7.2	265.8	8.0	267.5	4.3	95.1	4.8	87.7
	<i>EXPR</i>	6.9	266.0	7.0	267.7	3.9	94.9	3.9	88.9
Arlington	<i>Lidar</i>	7.2	263.6	7.4	263.7	3.1	73.4	3.2	73.2
	<i>CNTR</i>	6.1	259.7	6.8	261.5	3.3	64.5	3.6	71.5
	<i>EXPR</i>	5.6	258.2	5.5	258.0	3.1	64.9	3.0	71.2
Boardman	<i>Lidar</i>	7.0	251.4	7.1	252.0	2.8	85.5	2.8	84.8
	<i>CNTR</i>	6.3	252.1	6.3	249.4	2.6	54.8	2.9	57.5
	<i>EXPR</i>	5.8	250.4	5.4	247.0	2.5	57.9	2.5	58.6

825

This is the author's peer reviewed, accepted manuscript. However, the online version of record will be different from this version once it has been copyedited and typeset.

PLEASE CITE THIS ARTICLE AS DOI: 10.1063/5.0009138

826 Table 6. Percent of wind speeds in each region of a power curve of a typical wind turbine.

Wasco		HRRR			HRRRNEST		
		<i>Lidar</i>	<i>CNTR</i>	<i>EXPR</i>	<i>Lidar</i>	<i>CNTR</i>	<i>EXPR</i>
	<i>0-4 ms<sup>-1</sup></i>	40	35	43	42	40	43
	<i>5-12 ms<sup>-1</sup></i>	52	57	54	51	54	52
	<i>13-25 ms<sup>-1</sup></i>	8	8	3	7	6	5
Arlington							
	<i>0-4 ms<sup>-1</sup></i>	41	48	58	42	50	55
	<i>5-12 ms<sup>-1</sup></i>	50	49	42	50	47	43
	<i>13-25 ms<sup>-1</sup></i>	9	3	0	8	3	2
Boardman							
	<i>0-4 ms<sup>-1</sup></i>	54	55	61	54	55	57
	<i>5-12 ms<sup>-1</sup></i>	41	43	39	41	42	42
	<i>13-25 ms<sup>-1</sup></i>	5	2	1	5	3	2

827

This is the author's peer reviewed, accepted manuscript. However, the online version of record will be different from this version once it has been copyedited and typeset.

PLEASE CITE THIS ARTICLE AS DOI: 10.1063/1.50009138

828 Table 7. Summary of the HRRR and HRRRNEST reforecast configurations.

Acronym	Description	Initial- and Lateral-Boundary Conditions	Physics	Forecast Cadence and Forecast Length
HRRR	WFIP2 provisional HRRR (see Fig. 2a, large green box)  3-km horizontal grid spacing, 50 vertical layers	Initial: cold start from operational RAP; no data assimilation or prior cycling  Lateral boundary: operational RAP	Control (CNTR); see Table 8, second column	Twice-daily forecast initializations (i.e., 0000 and 1200 UTC)  Forecasts to 24 h, output at 15-min intervals
			Experimental (EXP); see Table 8, third column	
HRRRNEST	One-way concurrent nest within WFIP2 provisional HRRR (see Fig. 2a, small green box)  750-m horizontal grid spacing, 50 vertical layers	Initial: parent HRRR, after 3-h “spin-up” period  Lateral boundary: parent HRRR	Control (CNTR); see Table 8, second column	As in HRRR, except nest initialization delayed 3 h
			Experimental (EXP); see Table 8, third column	

829

This is the author's peer reviewed, accepted manuscript. However, the online version of record will be different from this version once it has been copyedited and typeset.

PLEASE CITE THIS ARTICLE AS DOI: 10.1063/5.0009138

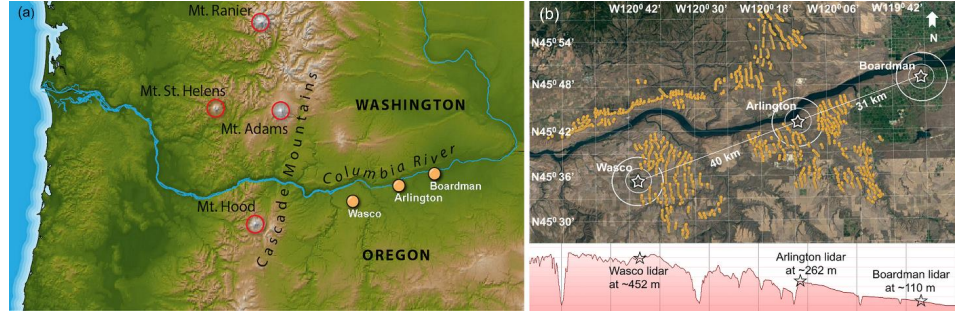
830 Table 8. Description of the control and experimental physics configurations used in the reforecasts (adapted from  
831 Table 2 in Olson et al. 2019), where model developments in support of WFIP2 are shown in bold. All components  
832 not under development in WFIP2 (regular font) are described in Benjamin et al. (2016)

Model Component	Control (CNTR)	Experimental (EXPR)
Land Surface	RUC 9-level	RUC 9-level
Surface Layer	MYNN	<b>MYNN</b>
PBL	MYNN level 2.5	<b>MYNN-EDMF</b>
SW Radiation	RRTMG	RRTMG
LW Radiation	RRTMG	RRTMG
Microphysics	Thompson Aero	Thompson Aero
Shallow Convection	---	<b>MYNN-EDMF</b>
Horizontal Diffusion	Smagorinsky on sigma levels	<b>Smagorinsky on cartesian coordinates</b>
Orographic Drag	---	<b>Small-scale gravity wave drag (inactive when <math>\Delta x \leq 1</math> km)</b>
Wind-Farm Drag	---	<b>Fitch et al. 2012</b>
Vertical Levels	51 levels	51 levels
Vertical Coordinate	sigma	<b>Hybrid sigma-pressure</b>
Albedo	AVHRR	AVHRR

This is the author's peer reviewed, accepted manuscript. However, the online version of record will be different from this version once it has been copyedited and typeset.

PLEASE CITE THIS ARTICLE AS DOI: 10.1063/5.0009138

833



834

835

Figure 1. (a) Map of the Columbia River Valley with the location of scanning Doppler lidars denoted by gold-filled circles. Red circles indicate the highest peaks of the Cascade Mountains. (b) Google Earth detailed map of the study area shows the location of two NOAA Doppler scanning lidars (200S) at Wasco (452 m ASL) and Arlington (262 m ASL). The Notre Dame University Halo Streamline XR lidar is located at the Boardman site at 110 m ASL. The white line indicates the east-west transect of the study region along the prevalent wind directions observed from surface measurements and models during previous studies in this area and confirmed from the analysis of Doppler lidar measurements in Pichugina et al. (2019). The surrounding wind turbines (total rated capacity of ~3,800 MW) are indicated by the clusters of dark yellow circles. An elevation gradient along the transect line is shown in (c).

842



This is the author's peer reviewed, accepted manuscript. However, the online version of record will be different from this version once it has been copyedited and typeset.

PLEASE CITE THIS ARTICLE AS DOI: 10.1063/1.50009138

843  
844  
845  
846  
847  
848  
849  
850

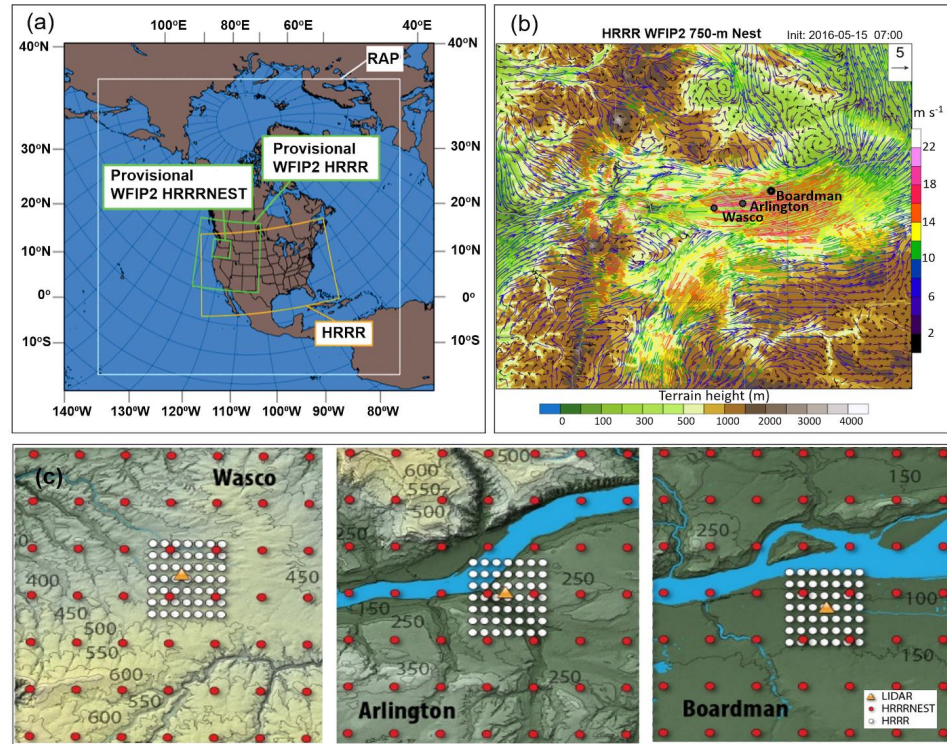
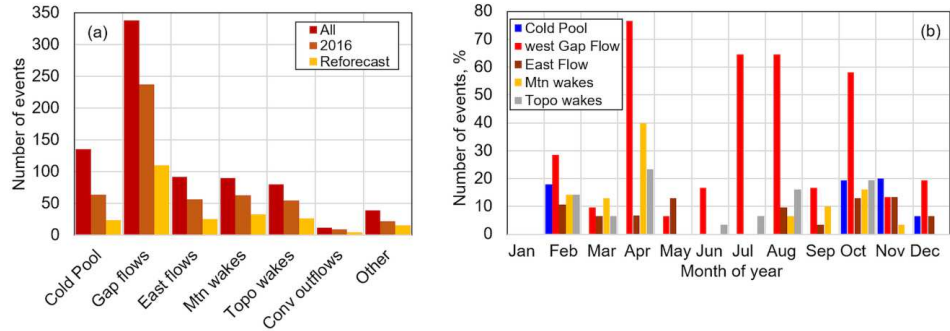


Figure 2. (a) Domains of WFIP2 (green) HRRR and HRRRNEST models are shown along with the operational (white) RAP (13-km grid spacing) and (red) HRRR-NCEP (3-km grid spacing) models. (Fig. 2a adapted from Olson et al. 2019). (b) An example of HRRRNEST-modeled wind flow at 80 m superimposed on area topography from WRF V3.7. The example is taken from a 7-h forecast initialized at 000UTC on 15 May 2016. Locations of Doppler lidars are shown by black circles. (c) Maps of the terrain elevations (in meters) at Wasco, Arlington, and Boardman research sites. The location of each lidar (dark yellow triangles) is shown relative to the HRRR 3-km model corners of the grid cells (red circles), and relative to the HRRRNEST 750-m model corners of the grid cells (white circles).

This is the author's peer reviewed, accepted manuscript. However, the online version of record will be different from this version once it has been copyedited and typeset.

PLEASE CITE THIS ARTICLE AS DOI: 10.1063/1.50009138

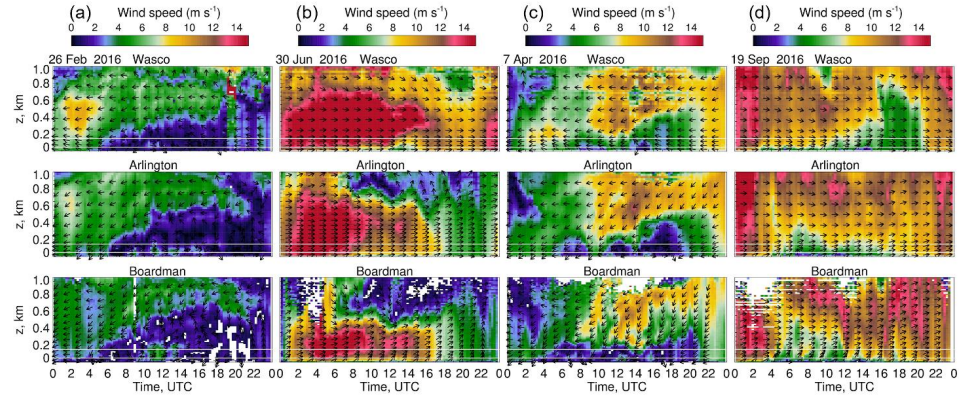


851  
852  
853  
854  
855  
856

Figure 3. Atmospheric events observed over the WFIP2 research area from the analysis of models, satellites, and all available ground observations. (a) The number of events observed during 18 months of the experiment, 12 months of 2016, and reforecast periods in 2016 shown by colors according to the legend. Multiple events can occur on the same day. (b) Relative number (%) of major events in each month observed during the reforecast periods.

This is the author's peer reviewed, accepted manuscript. However, the online version of record will be different from this version once it has been copyedited and typeset.

PLEASE CITE THIS ARTICLE AS DOI: 10.1063/1.50009138

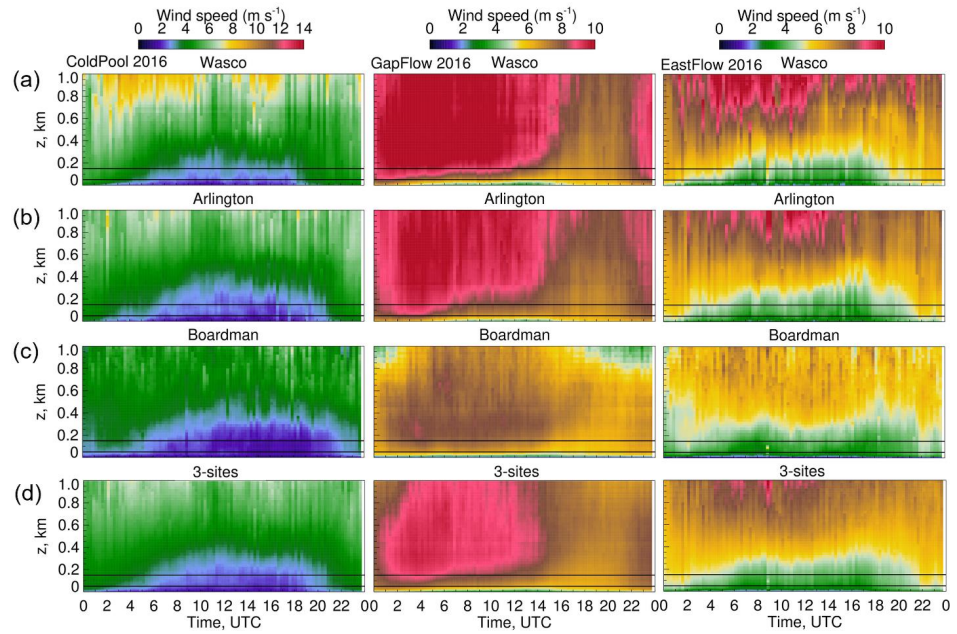


857  
858  
859  
860  
861  
862  
863

Figure 4. Time-height cross-sections of wind speed and wind direction at the (from top to bottom) Wasco, Arlington, and Boardman site during atmospheric phenomena observed in the WFIP2 area: (a) Cold pool, (b) Westerly Gap Flow, (c) Easterly Gap Flow, and (d) Mountain Waves. Wind speed is color-coded from 0 to 15  $\text{m s}^{-1}$  according to the color scale at the top of each panel. Black arrows show wind direction. Two white horizontal lines on each panel indicate typical rotor-disk height, 50-150 m AGL.

This is the author's peer reviewed, accepted manuscript. However, the online version of record will be different from this version once it has been copyedited and typeset.

PLEASE CITE THIS ARTICLE AS DOI: 10.1063/5.0009138

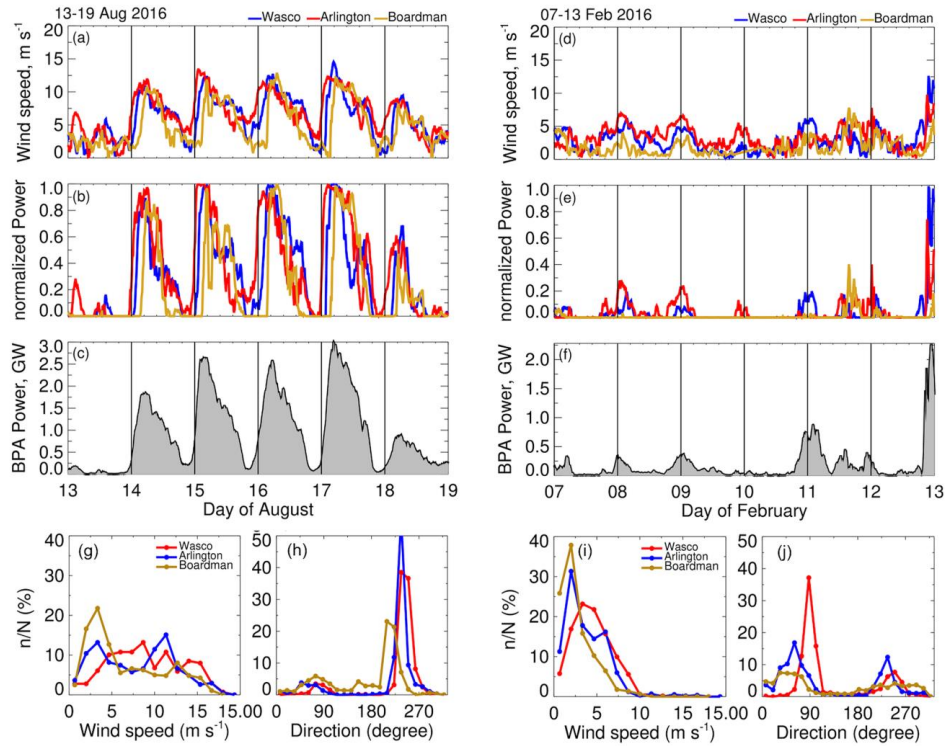


864  
865  
866  
867  
868  
869

Figure 5. Time-height cross-sections of wind speed averaged over all days in 2016 with associated atmospheric phenomena: (from left to right) Cold pool; Westerly Gap flow, and Easterly Gap Flow. Event-averaged wind speed is shown for each site: (a) Wasco, (b) Arlington, (c) Boardman, and (d) for 3-site composites. Wind speeds are color-coded according to the color scale shown for each event on the top of this figure.

This is the author's peer reviewed, accepted manuscript. However, the online version of record will be different from this version once it has been copyedited and typeset.

PLEASE CITE THIS ARTICLE AS DOI: 10.1063/1.50009138



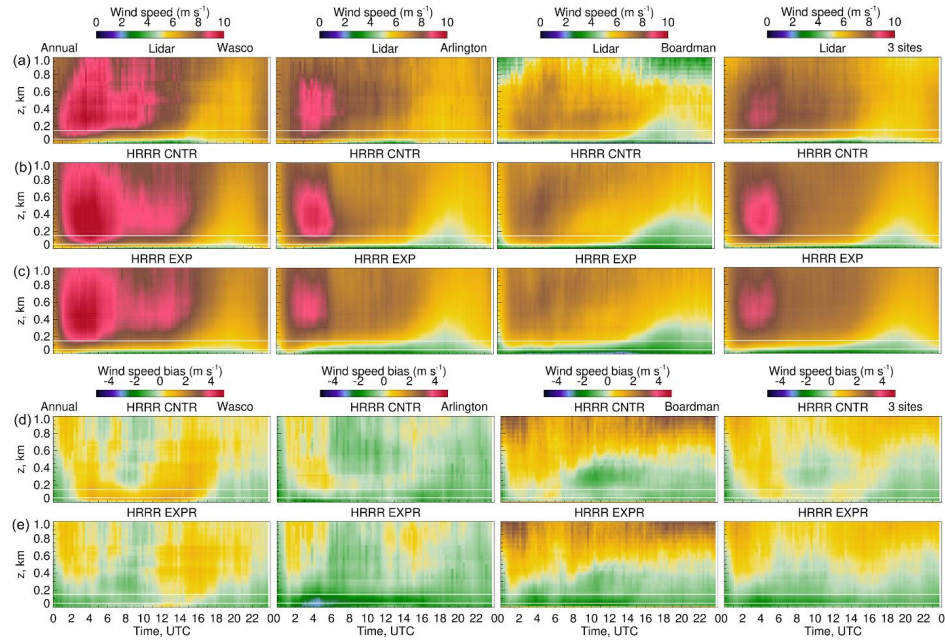
870

871 Figure 6. Time series of (a, d) 80-m wind speed observed at the 3 lidar sites and (b, e) wind power computed by  
 872 normalized power curve during a westerly gap flow/marine intrusion event on 13-18 August 2016, and cold pool event  
 873 on 07-12 February 2016. (c, f) Total power generation over the Bonneville Power Authority (BPA) area during these  
 874 periods. The bottom row shows distributions of wind speed and wind directions for the (g, h) August and (i, j) February  
 875 cases. Different colors indicate each site according to the legends.

876

This is the author's peer reviewed, accepted manuscript. However, the online version of record will be different from this version once it has been copyedited and typeset.

PLEASE CITE THIS ARTICLE AS DOI: 10.1063/5.0009138



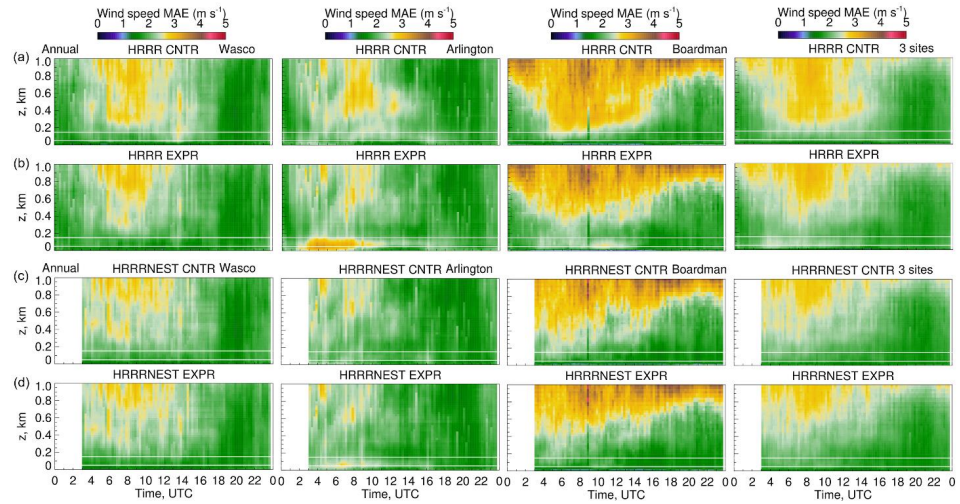
877  
878  
879  
880  
881  
882

Figure 7. Time-height cross-sections of annual-mean wind speed from (a) lidar, (b) HRRR CNTR run, and (c) HRRR EXP run for each site (from left to right columns: Wasco, Arlington, and Boardman), and for the 3-site composites. Two bottom rows show the wind speed difference (bias) between (d) HRRR CNTR run and lidar, and (e) HRRR EXP run and lidar, expressed as HRRR minus lidar-measured values. White lines indicate 50 m and 150 m AGL.

This is the author's peer reviewed, accepted manuscript. However, the online version of record will be different from this version once it has been copyedited and typeset.

PLEASE CITE THIS ARTICLE AS DOI: 10.1063/5.0009138

883



884

885

Figure 8. Annual statistics: same as Fig. 7d-e but for MAE from (a, b) HRRR CNTR and EXPR runs, (c, d) HRRRNEST CNTR and EXPR runs. All panels are shown for 00z runs of both models; 12z runs were similar.

886

887

888

889

This is the author's peer reviewed, accepted manuscript. However, the online version of record will be different from this version once it has been copyedited and typeset.

PLEASE CITE THIS ARTICLE AS DOI: 10.1063/5.0009138

890  
891  
892  
893  
894

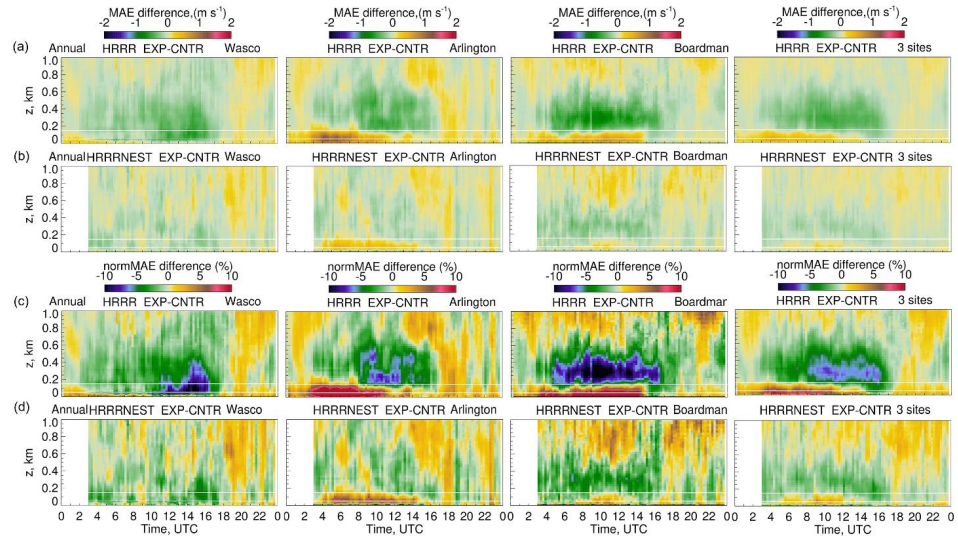


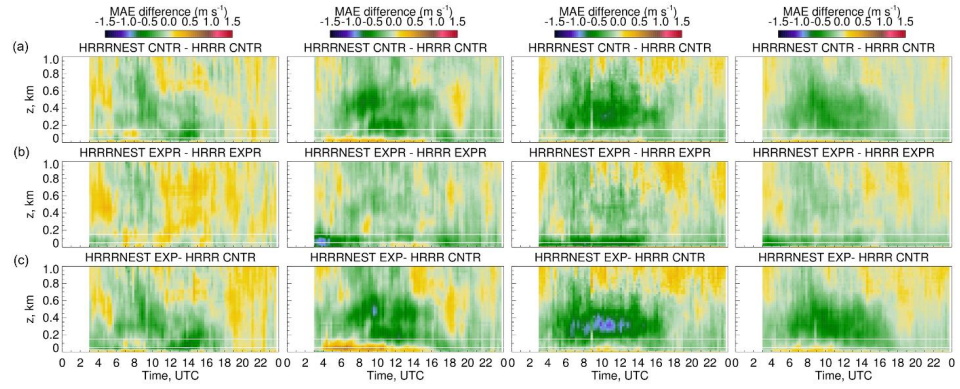
Figure 9. Annual MAE differences due to changes in model physics and other updates (EXPR-CNTR) made in (a) HRRR and (b) HRRRNEST. Bottom two rows (c, d) show these differences expressed as percentages, normalized by mean, lidar-measured wind speeds.



This is the author's peer reviewed, accepted manuscript. However, the online version of record will be different from this version once it has been copyedited and typeset.

PLEASE CITE THIS ARTICLE AS DOI: 10.1063/5.0009138

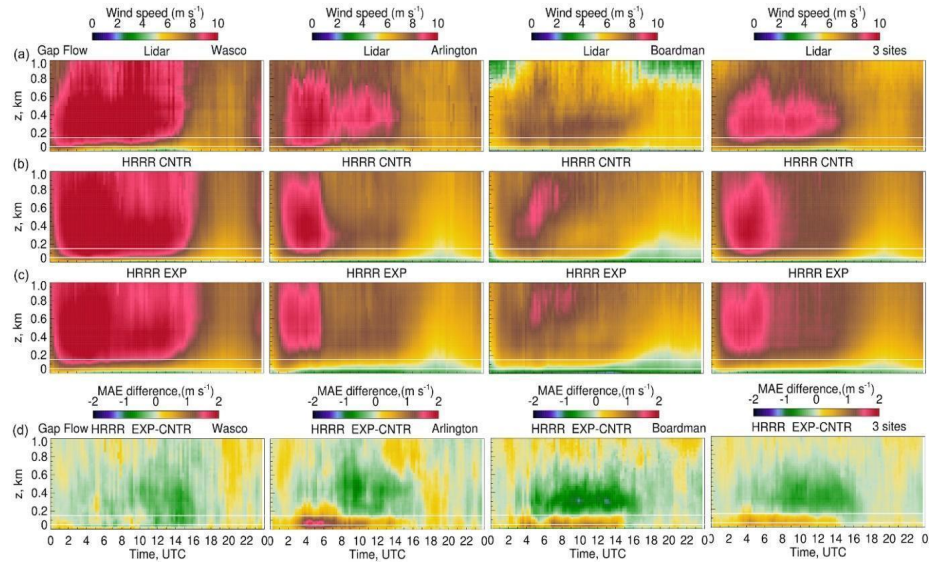
895



896 Figure 10. Annual MAE differences due to changes in model horizontal spacing (HRRRNEST-HRRR) for (a) CNTR  
 897 and (b) EXPR runs of models. The bottom row (c) shows MAE difference due to combined effects of changes in model  
 898 physics and horizontal spacing.  
 899

This is the author's peer reviewed, accepted manuscript. However, the online version of record will be different from this version once it has been copyedited and typeset.

PLEASE CITE THIS ARTICLE AS DOI: 10.1063/5.0009138



900  
901  
902  
903  
904

Figure 11. Time-height cross-sections of wind speed from lidar, HRRR CNTR, and HRRR EXP 00z runs averaged over (a-c) westerly gap flow. The bottom row (d) shows the MAE difference between EXP and CNTR runs. Columns are shown for (from left to right) Wasco, Arlington, Boardman sites, and 3-site composites.

This is the author's peer reviewed, accepted manuscript. However, the online version of record will be different from this version once it has been copyedited and typeset.

PLEASE CITE THIS ARTICLE AS DOI: 10.1063/5.0009138

905  
906

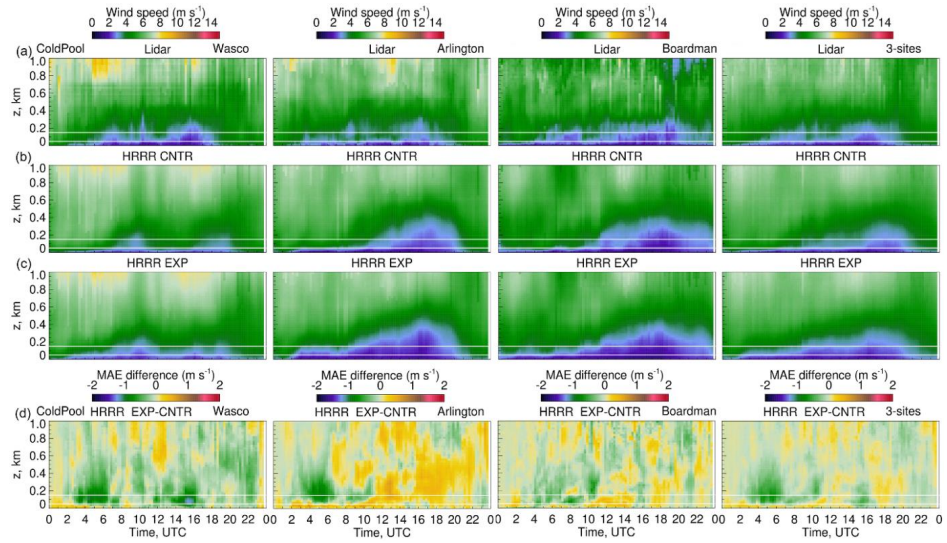
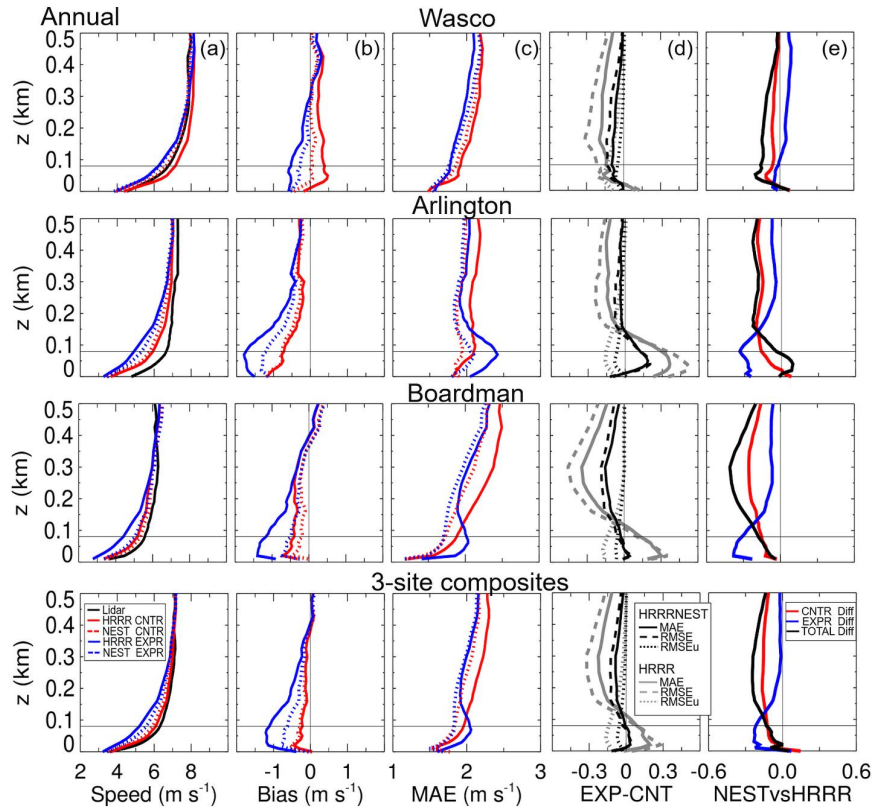


Figure 12. Same as Fig. 11 but composited over cold-pool events.

This is the author's peer reviewed, accepted manuscript. However, the online version of record will be different from this version once it has been copyedited and typeset.

PLEASE CITE THIS ARTICLE AS DOI: 10.1063/5.0009138



907

908

909

910

911

912

913

914

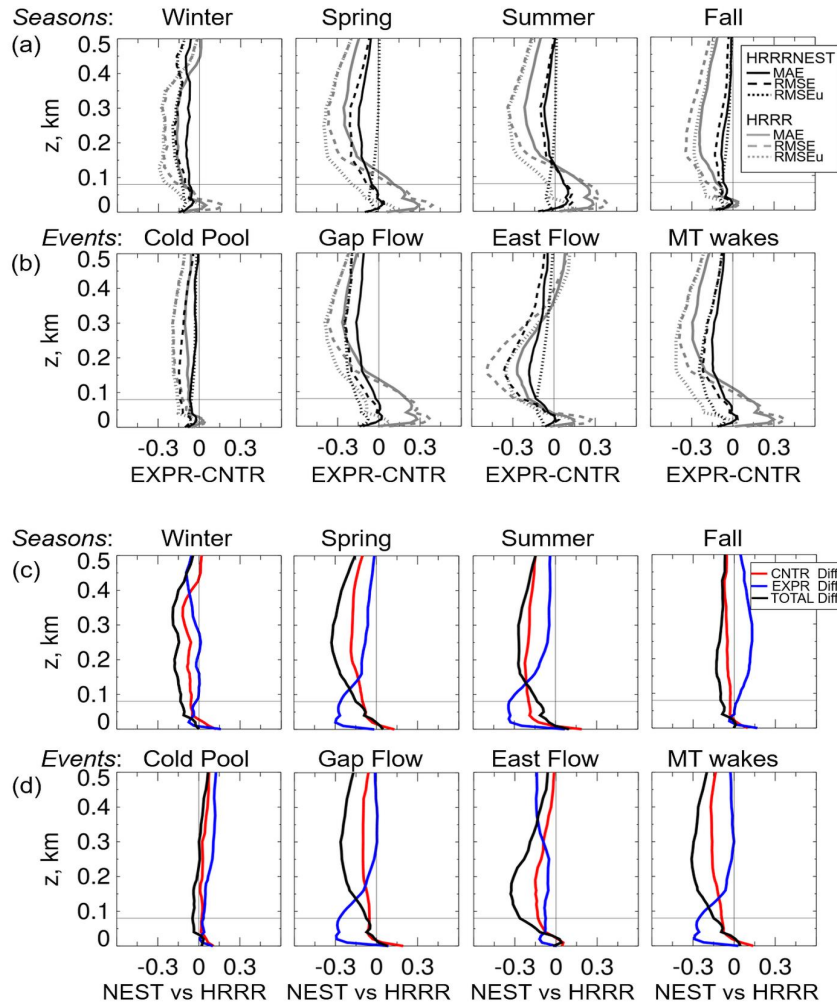
915

916

Figure 13. Annual profiles of wind speed and validation metrics are shown for the (from top to bottom), Wasco, Arlington, and Boardman sites, and the 3-site composites. (a) Measured wind speed is shown by a black solid line, and the (a-c) CNTR and EXPR runs are shown by red and blue colors for (solid) HRRR and (dashed) HRRRNEST according to the legend at the top left panel. (d) MAE improvement due to model physics: error differences ( $\text{m s}^{-1}$ ) between EXPR and CNTR runs of (black) HRRRNEST and (gray) HRRR models for (solid) MAE, (dashed) RMSE, and (dotted) bias-corrected RMSE (RMSEu). (e) MAE improvement due to finer resolution in the (red) CNTR runs (HRRRNEST CNTR – HRRR CNTR) of both models, and (blue) finer resolution in the EXPR runs (HRRRNEST EXPR – HRRR EXPR), and the (black) total effect of physics and resolution (HRRRNEST EXPR – HRRR CNTR). Negative values mean improvement.

This is the author's peer reviewed, accepted manuscript. However, the online version of record will be different from this version once it has been copyedited and typeset.

PLEASE CITE THIS ARTICLE AS DOI: 10.1063/5.0009138

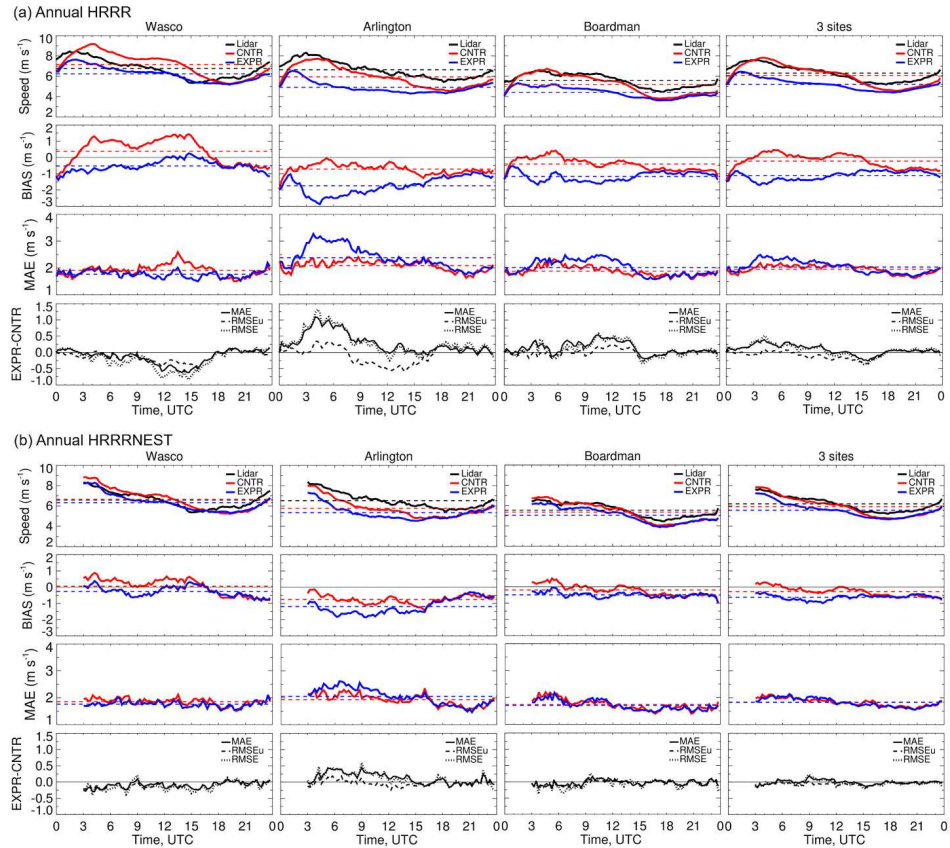


917

918 Figure 14. (a-b) 3-site composite profiles of error differences ( $m s^{-1}$ ) between EXP and CNTR runs of (black)  
 919 HRRRNEST and (gray) HRRR models: (solid) MAE, (dashed) RMSE, and (dotted) bias-corrected RMSE (RMSEu).  
 920 Error differences are shown for (a) calendar seasons and (b) four major events. (c-d) MAE differences due to (red)  
 921 finer resolution in the CNTR runs (HRRRNEST CNTR – HRRR CNTR), and (blue) finer resolution in the EXP runs  
 922 (HRRRNEST EXP – HRRR EXP). The total effect of improved physics and model resolution (HRRRNEST EXP  
 923 – HRRR CNTR) is shown by black lines. Improvements are shown for (c) calendar seasons and (d) four major events.  
 924 Negative values mean improvement.

This is the author's peer reviewed, accepted manuscript. However, the online version of record will be different from this version once it has been copyedited and typeset.

PLEASE CITE THIS ARTICLE AS DOI: 10.1063/5.0009138



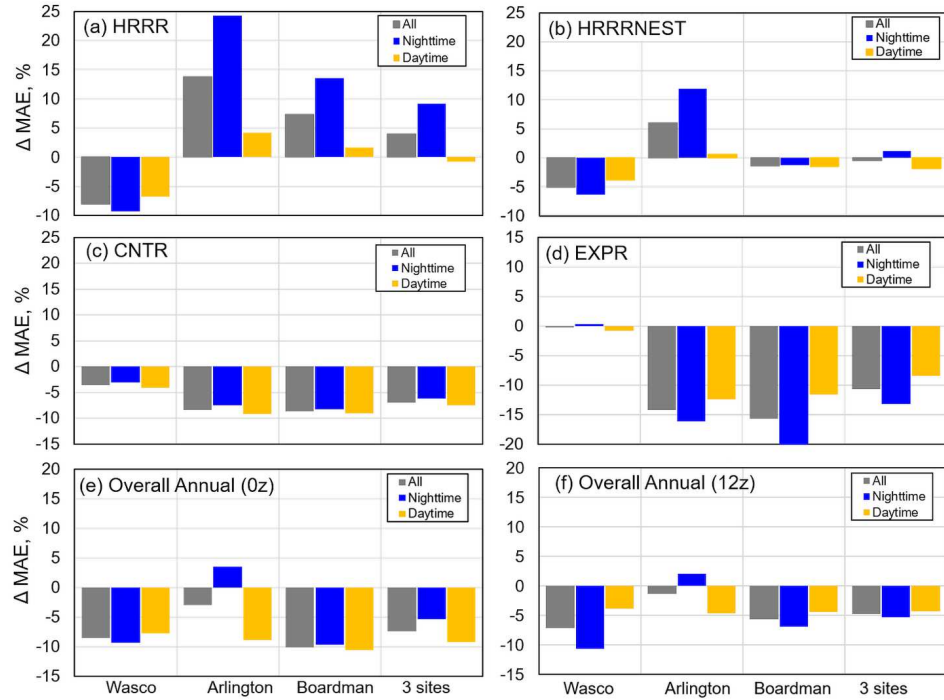
925  
926  
927  
928  
929  
930  
931  
932

Figure 15. Time-series of 80-m annual (15a from top to bottom) winds speed, BIAS, MAE, and the difference in validation metrics between EXPR and CNTR runs of HRRR initialized at 00z.

Mean values in the top three panels are from (black) lidar measurements, and the (red) CNTR and (blue) EXPR runs. Horizontal dashed lines of the corresponding color represent mean values of Bias and MAE from both runs further averaged over the diurnal cycle. Black lines on the bottom panels show the difference between two runs (EXPR-CNTR) for (solid) RMSE, (dashed) unbiased RMSE, and (dotted) MAE according to the legend at the top right corner. Fig. 15b is the same as Fig. 15a, except for HRRRNEST.

This is the author's peer reviewed, accepted manuscript. However, the online version of record will be different from this version once it has been copyedited and typeset.

PLEASE CITE THIS ARTICLE AS DOI: 10.1063/5.0009138



933  
934  
935  
936  
937  
938  
939  
940  
941  
942  
943

Figure 16. Relative differences in annual 80-m wind speed MAE ( $\Delta$ -MAE, in %) due to the (a, b) experimental physics and (c, d) model horizontal grid resolution at each site and 3-site composites, (e) the overall (physics + resolution)  $\Delta$ -MAE for initial time 0z, (f) same as (e) but for the initial time 12z. Each panel shows  $\Delta$ -MAE for (gray) data averaged for all hours, (dark blue) nighttime, and (dark yellow) daytime hours. Nighttime and daytime hours for the initial time 0z (Fig. 16 a-e) are 0300-1200 UTC. Nighttime and daytime hours for the initial time 12z (Fig. 16 f) are 00-1200 UTC and 1500-2400 UTC. The  $\Delta$ -MAEs were computed as follow: (a) [HRRR EXPR – HRRR CNTR]/HRRR CNTR; (b) [HRRRNEST EXPR – HRRRNEST CNTR]/HRRRNEST CNTR; (c) [HRRRNEST CNTR – HRRR CNTR]/HRRR CNTR; (d) [HRRRNEST EXPR – HRRR EXPR]/RRR EXPR; (e-f) [HRRRNEST EXPR – HRRR CNTR]/HRRR CNTR. The negative values at each panel imply improvement.

This is the author's peer reviewed, accepted manuscript. However, the online version of record will be different from this version once it has been copyedited and typeset.

PLEASE CITE THIS ARTICLE AS DOI: 10.1063/5.0009138

944  
945  
946  
947  
948

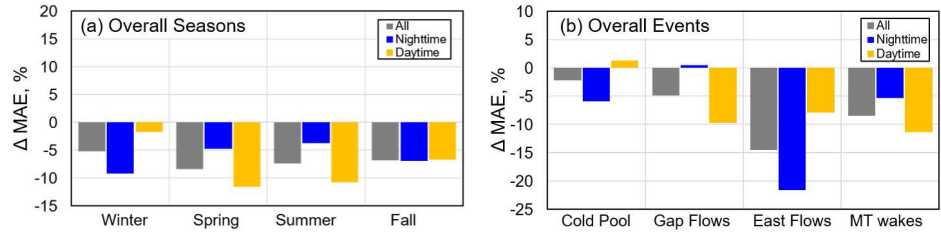
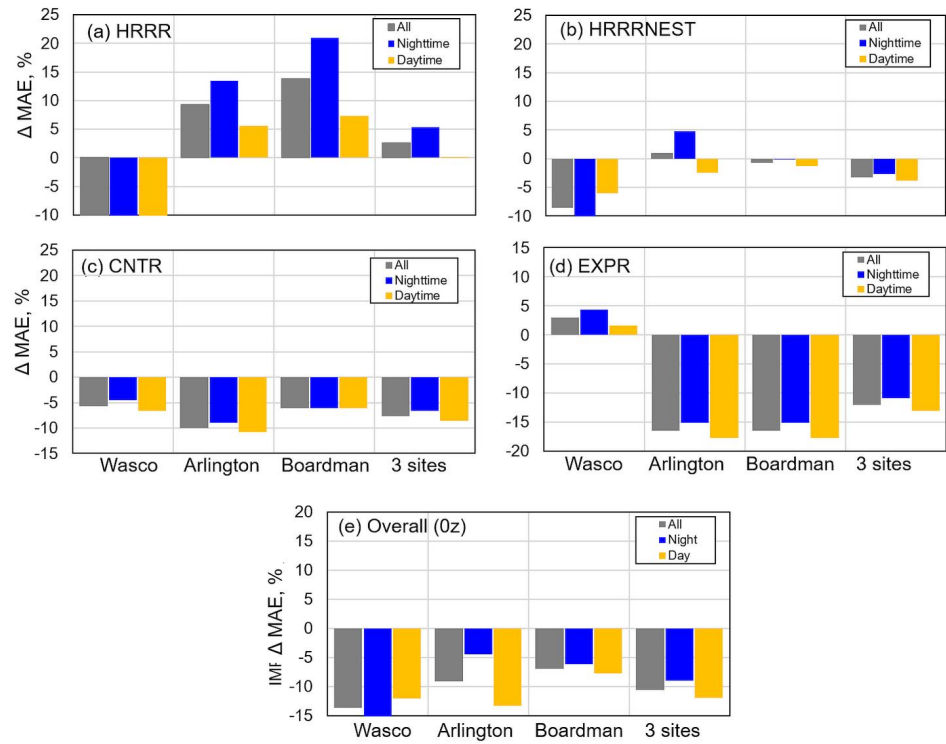


Figure 17. The combined physics/horizontal grid resolution relative  $\Delta$ -MAE for 3-site composites of 80-m winds averaged over (a) each season and (b) major event types. Combined relative MAE defined as  $[\text{HRRRNEST EXPR} - \text{HRRR CNTR}] / \text{HRRR CNTR}$ .



This is the author's peer reviewed, accepted manuscript. However, the online version of record will be different from this version once it has been copyedited and typeset.

PLEASE CITE THIS ARTICLE AS DOI: 10.1063/5.0009138



949

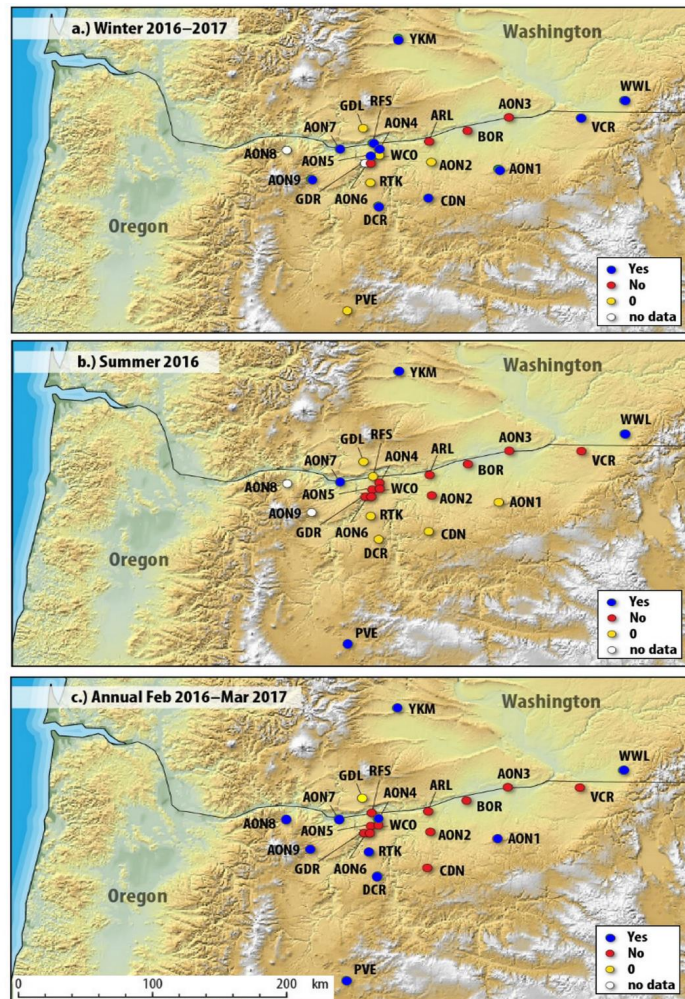
950 Figure 18. Same as Fig. 16 a-e but for the power MAE computed by using 80 m wind speed measured by lidar and  
 951 predicted by CNTR and EXPR runs of HRRR and HRRRNEST for 0z initial time.

This is the author's peer reviewed, accepted manuscript. However, the online version of record will be different from this version once it has been copyedited and typeset.

PLEASE CITE THIS ARTICLE AS DOI: 10.1063/5.0009138

952

953 Figure 19. Maps of the terrain overlapped with the bias difference (colored circles) between HRRRNEST EXPR and  
 954 CNTR runs (Bianco et al. 2019) at the locations of 19 sodars and 3 different types of lidars as described in the text.  
 955 The bias difference is shown in three categories according to the legend on each map. Sites, where the absolute value  
 956 of the bias from EXPR runs, is smaller (larger) than from the CNTR runs indicated some improvement (degradation)  
 957 in model physics are shown correspondingly by blue (red) circles and indicated in the legend as “Yes” (“No”). Sites,  
 958 where biases from CNTR and EXPR runs are almost equal, are indicated by yellow and “0” in the legend. Sites,  
 959 where observed or modeled data were not available (no data) are indicated by white circles. Maps are shown for mean values  
 960 over reforecast periods in the (a) winter, (b) summer seasons, and (c) all four-seasons of WFIP2.



50

This is the author's peer reviewed, accepted manuscript. However, the online version of record will be different from this version once it has been copyedited and typeset.

PLEASE CITE THIS ARTICLE AS DOI: 10.1063/5.0009138

961  
962  
963  
964  
965

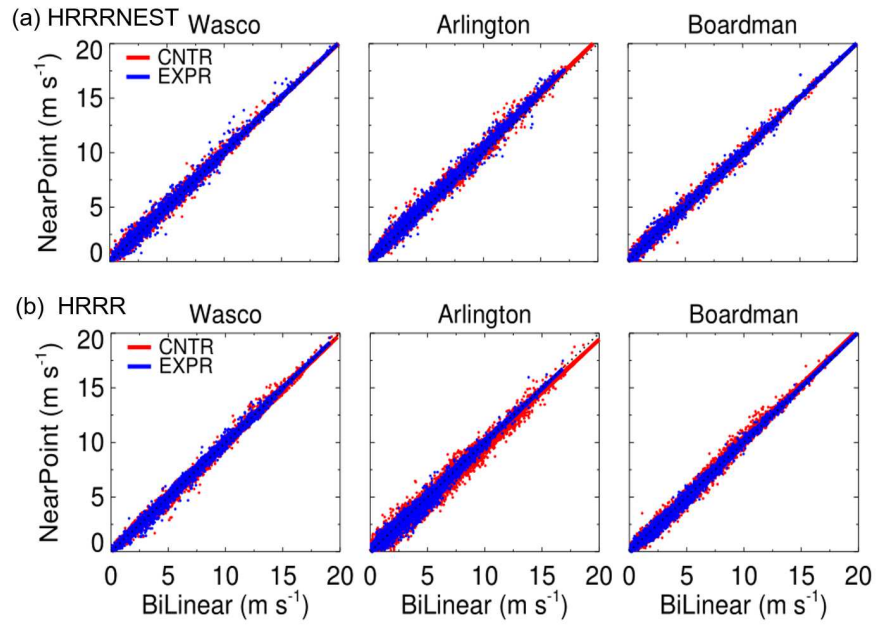
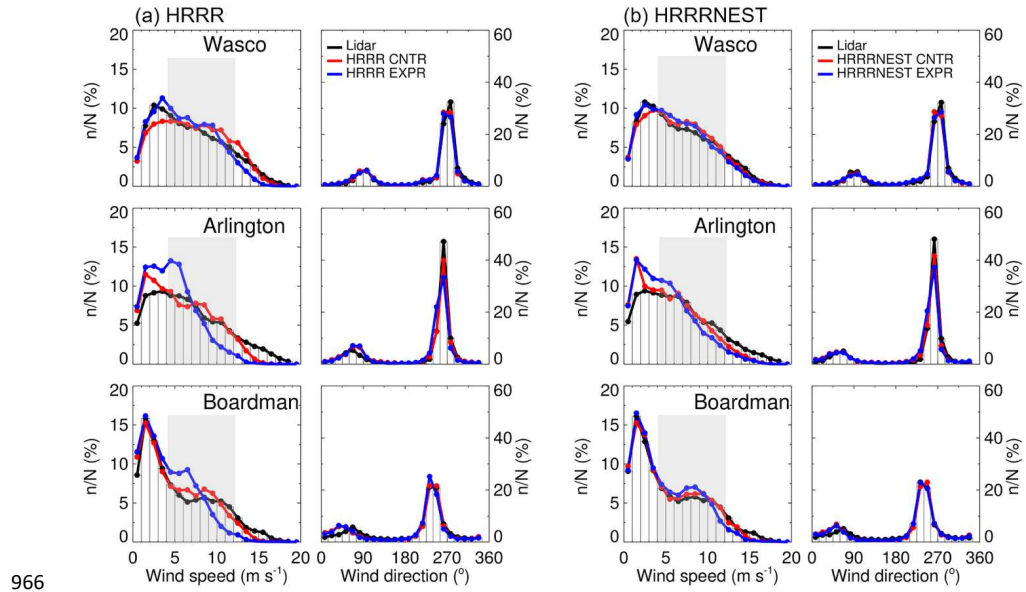


Fig. 20. Scatter plots between modeled of 80-m wind speed extracted at the lidar sites using bi-linear interpolation or nearest grid point value: (a) for HRRRNEST (750 m horizontal grid) and (b) HRRR (3 km horizontal grid) models. Red and blue points on all panels represent CNTR and EXPR runs respectively.

This is the author's peer reviewed, accepted manuscript. However, the online version of record will be different from this version once it has been copyedited and typeset.

PLEASE CITE THIS ARTICLE AS DOI: 10.1063/5.0009138



966

967 Figure 21. The annual distributions of 80-m wind speeds and wind directions at each site are shown for (red) control  
 968 and (blue) experimental runs of (a) HRRR and (b) HRRRNEST models. Lidar-measured variables are shown by black  
 969 curves at each panel. Gray shaded areas indicate wind speeds ( $4\text{--}12\text{ m s}^{-1}$ ) in a non-rated region of a typical wind turbine  
 970 power curve (Dupont et al. 2017).

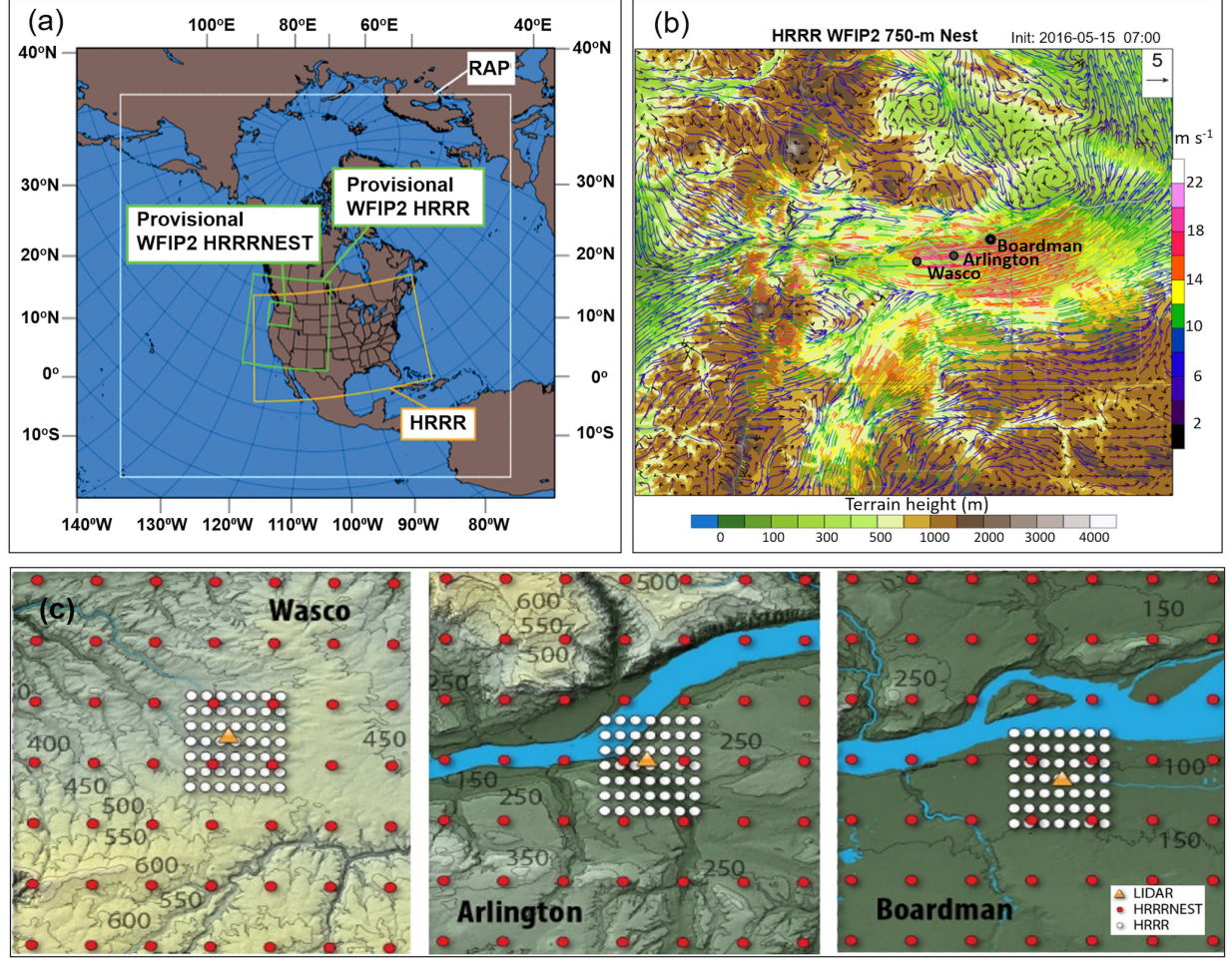
This is the author's peer reviewed, accepted manuscript. However, the online version of record will be different from this version once it has been copyedited and typeset.

PLEASE CITE THIS ARTICLE AS DOI: 10.1063/5.0009138



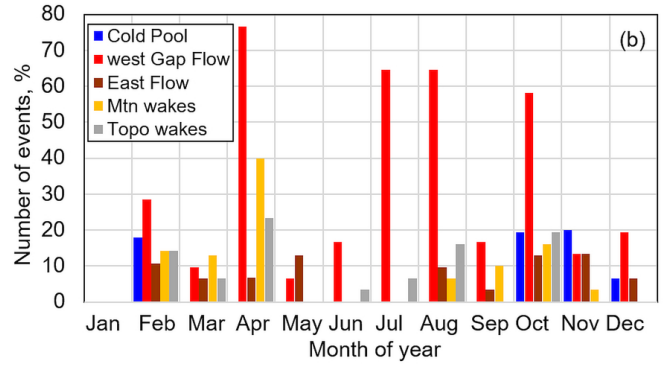
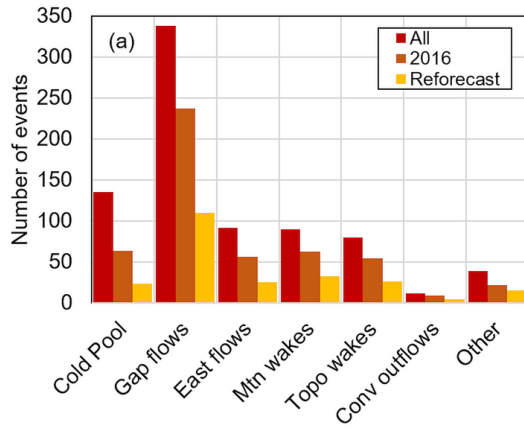
This is the author's peer reviewed, accepted manuscript. However, the online version of record will be different from this version once it has been copyedited and typeset.

PLEASE CITE THIS ARTICLE AS DOI: 10.1063/5.0009138



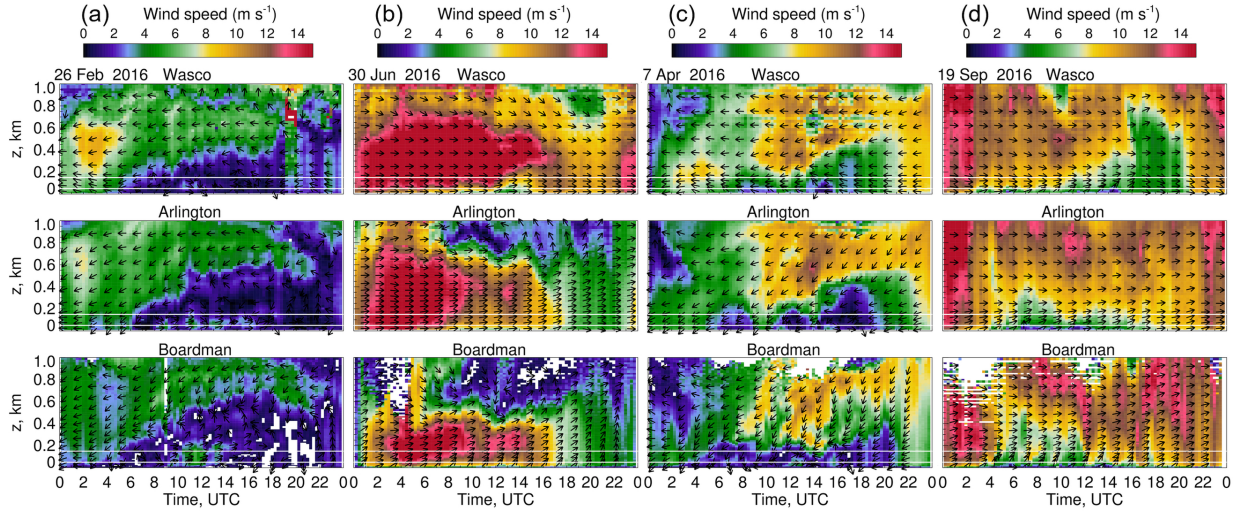
This is the author's peer reviewed, accepted manuscript. However, the online version of record will be different from this version once it has been copyedited and typeset.

PLEASE CITE THIS ARTICLE AS DOI: 10.1063/5.0009138



This is the author's peer reviewed, accepted manuscript. However, the online version of record will be different from this version once it has been copyedited and typeset.

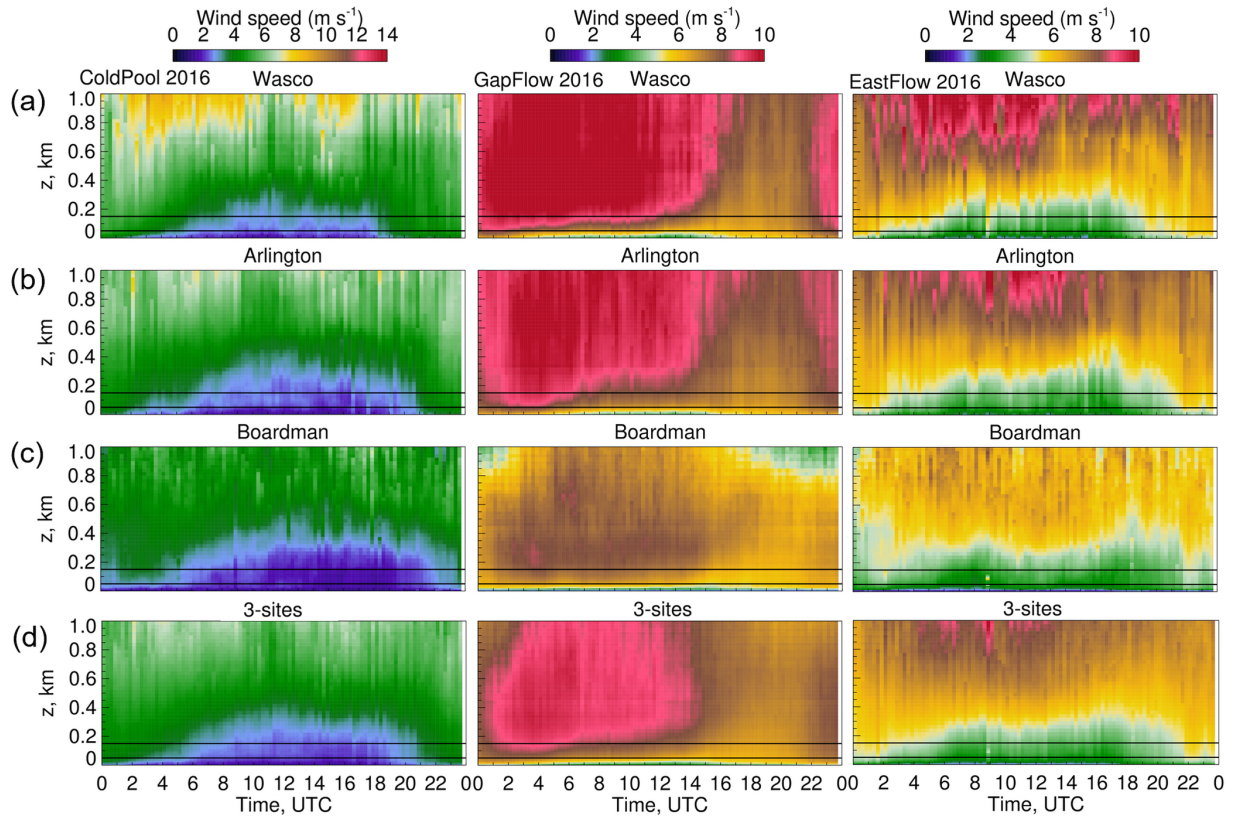
PLEASE CITE THIS ARTICLE AS DOI: 10.1063/1.50009138





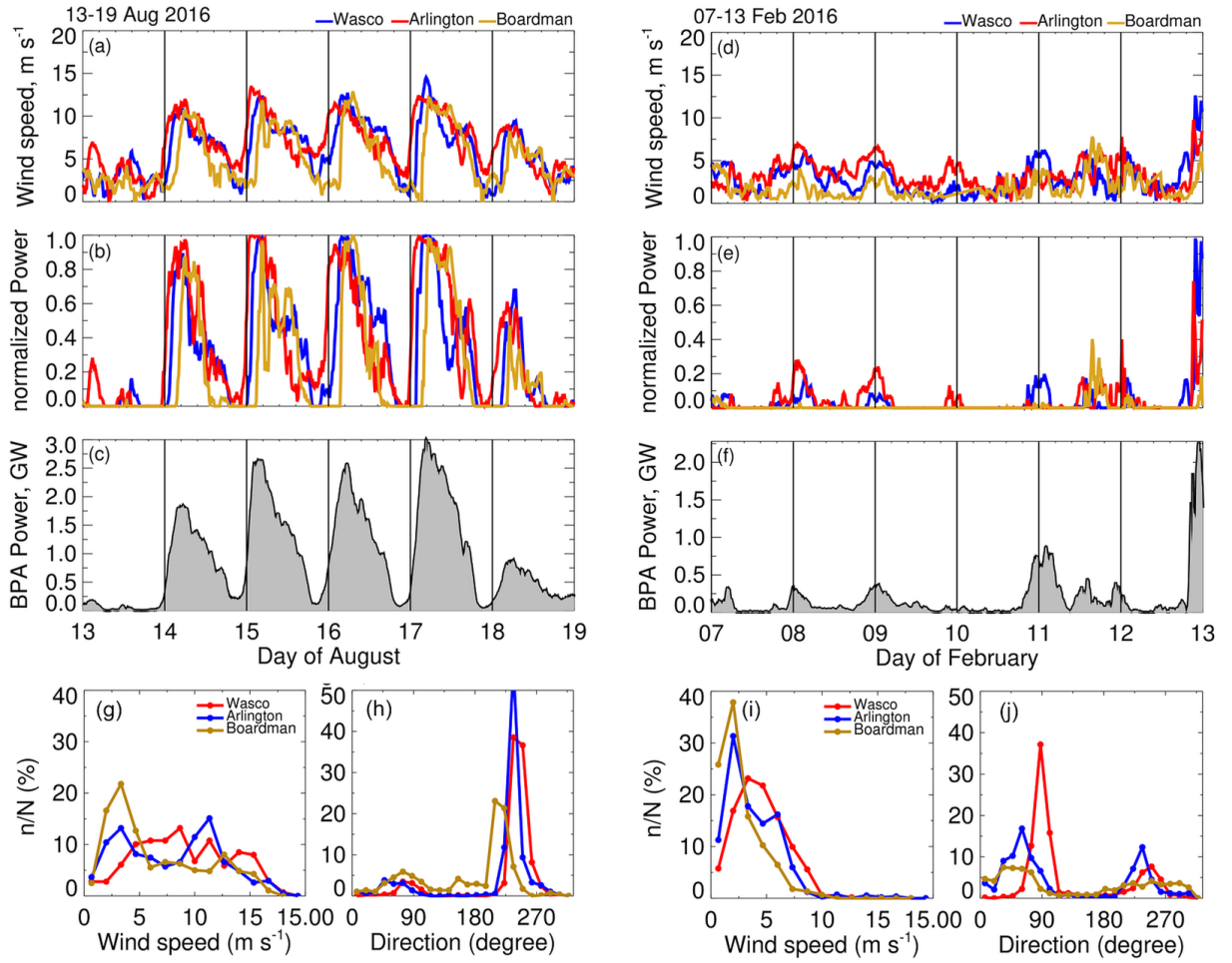
This is the author's peer reviewed, accepted manuscript. However, the online version of record will be different from this version once it has been copyedited and typeset.

PLEASE CITE THIS ARTICLE AS DOI: 10.1063/5.0009138



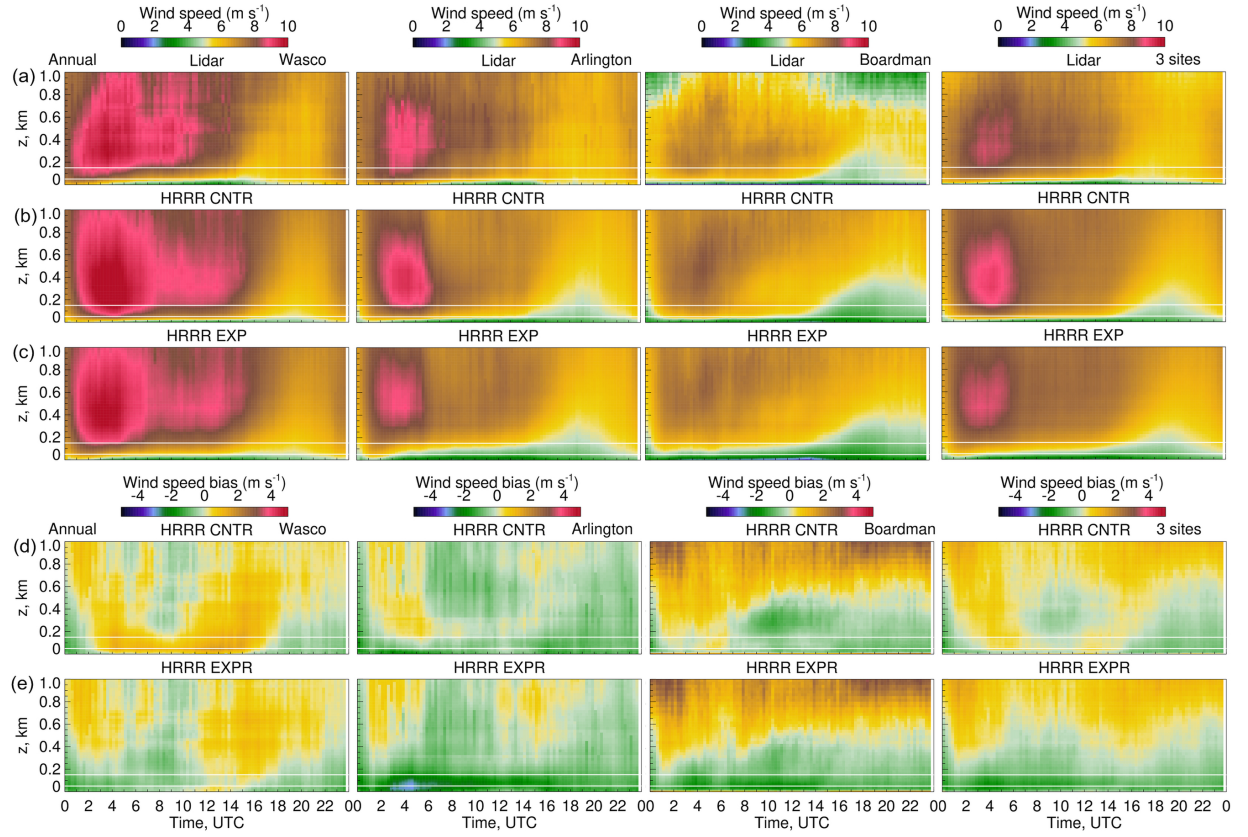
This is the author's peer reviewed, accepted manuscript. However, the online version of record will be different from this version once it has been copyedited and typeset.

PLEASE CITE THIS ARTICLE AS DOI: 10.1063/5.0009138



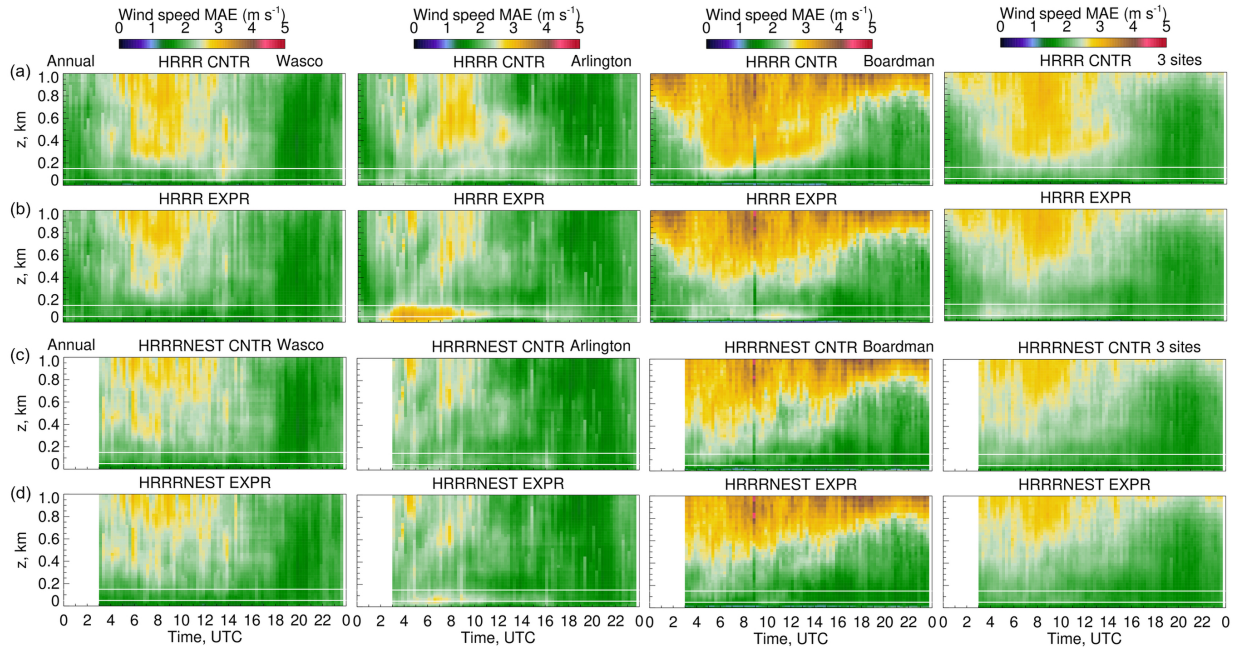
This is the author's peer reviewed, accepted manuscript. However, the online version of record will be different from this version once it has been copyedited and typeset.

PLEASE CITE THIS ARTICLE AS DOI: 10.1063/5.0009138



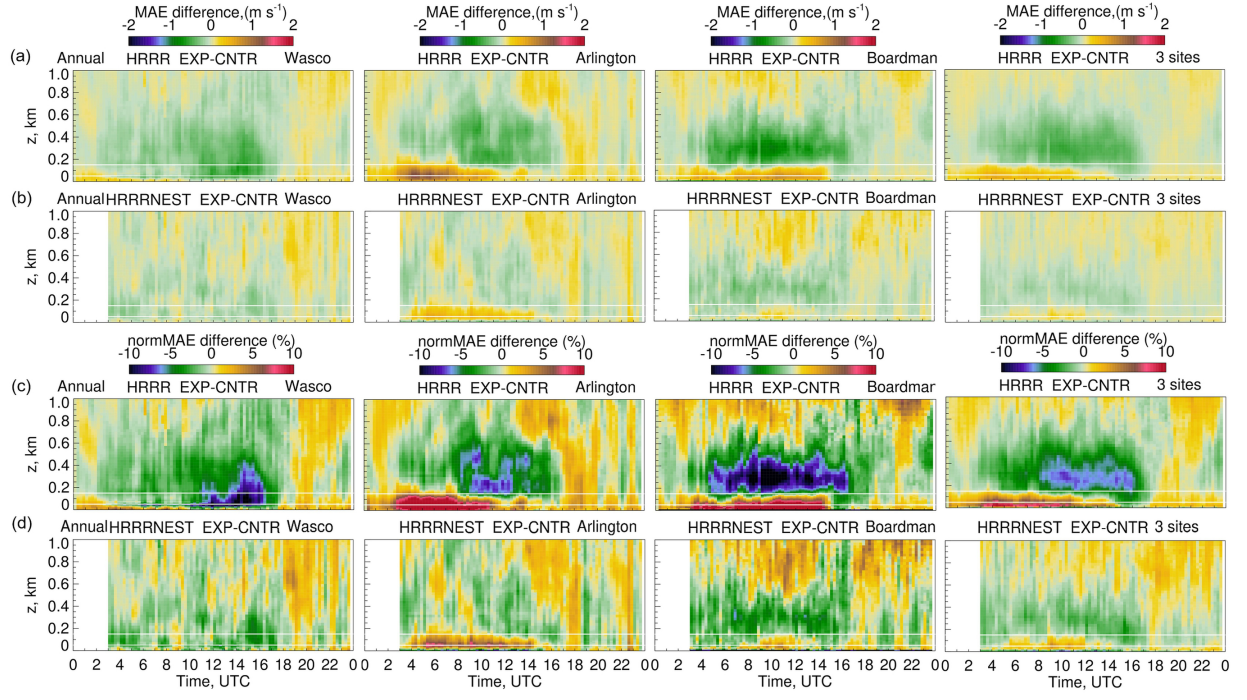
This is the author's peer reviewed, accepted manuscript. However, the online version of record will be different from this version once it has been copyedited and typeset.

PLEASE CITE THIS ARTICLE AS DOI: 10.1063/5.0009138



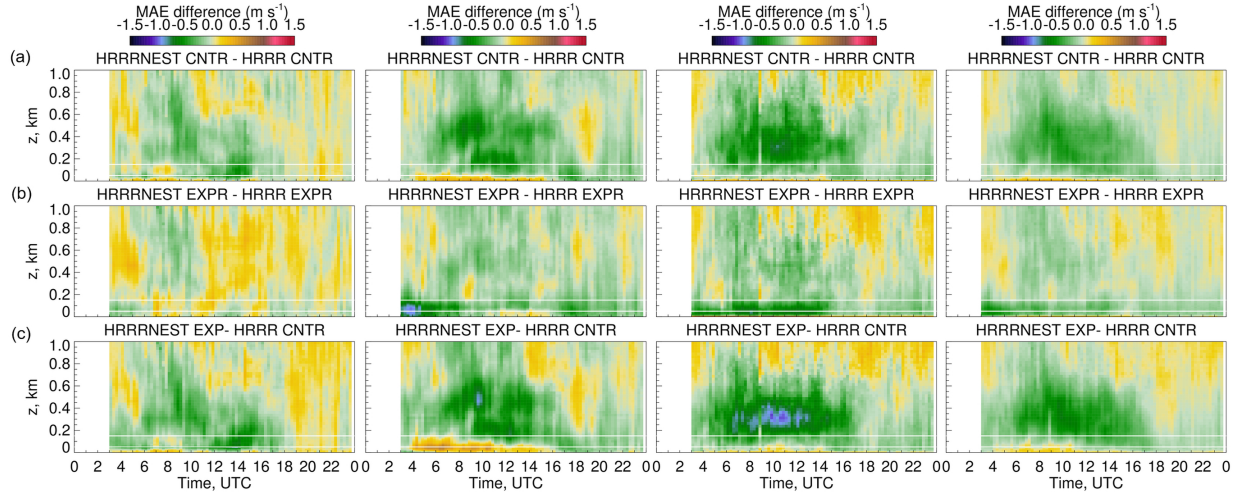
This is the author's peer reviewed, accepted manuscript. However, the online version of record will be different from this version once it has been copyedited and typeset.

PLEASE CITE THIS ARTICLE AS DOI: 10.1063/5.0009138



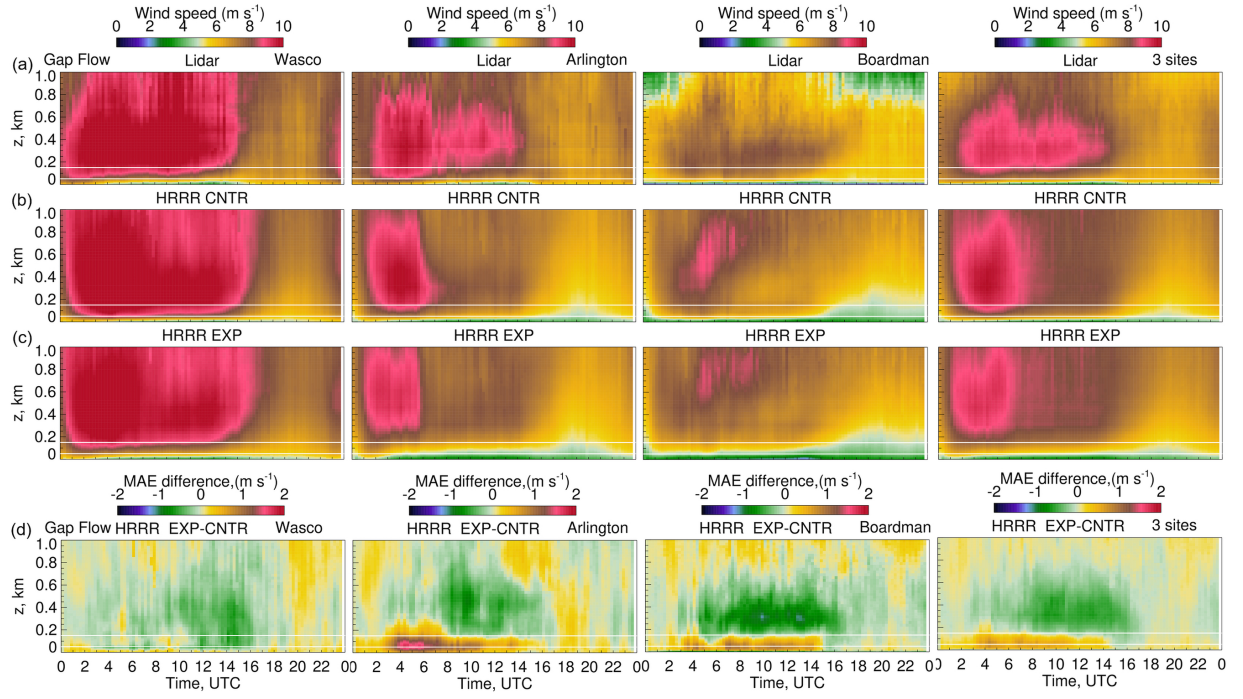
This is the author's peer reviewed, accepted manuscript. However, the online version of record will be different from this version once it has been copyedited and typeset.

PLEASE CITE THIS ARTICLE AS DOI: 10.1063/5.0009138



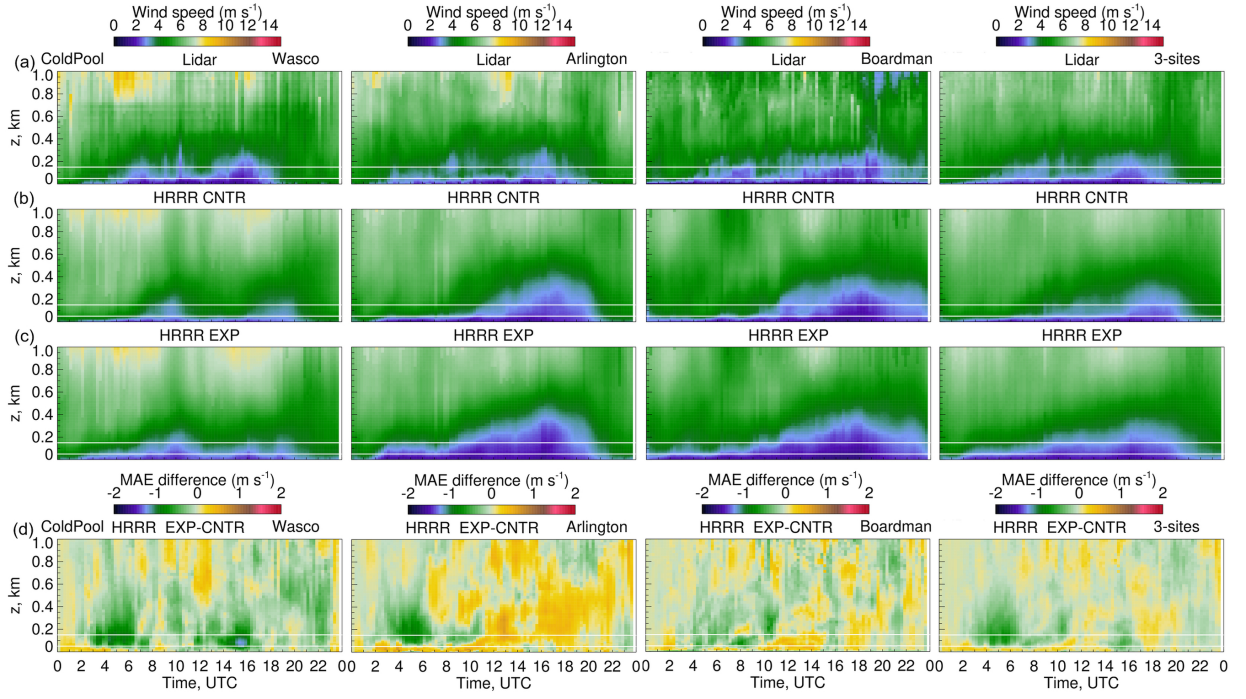
This is the author's peer reviewed, accepted manuscript. However, the online version of record will be different from this version once it has been copyedited and typeset.

PLEASE CITE THIS ARTICLE AS DOI: 10.1063/5.0009138



This is the author's peer reviewed, accepted manuscript. However, the online version of record will be different from this version once it has been copyedited and typeset.

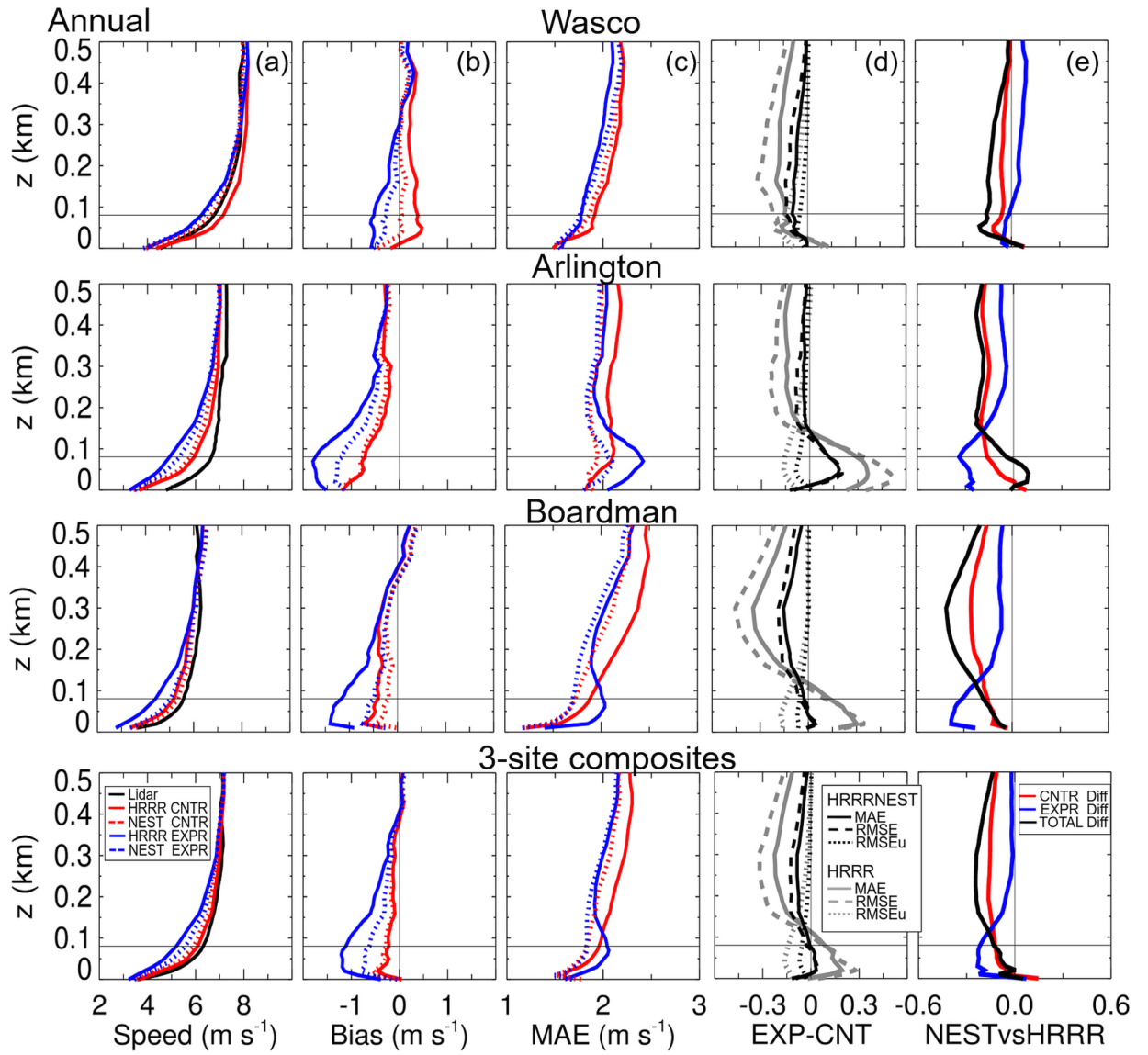
PLEASE CITE THIS ARTICLE AS DOI: 10.1063/5.0009138





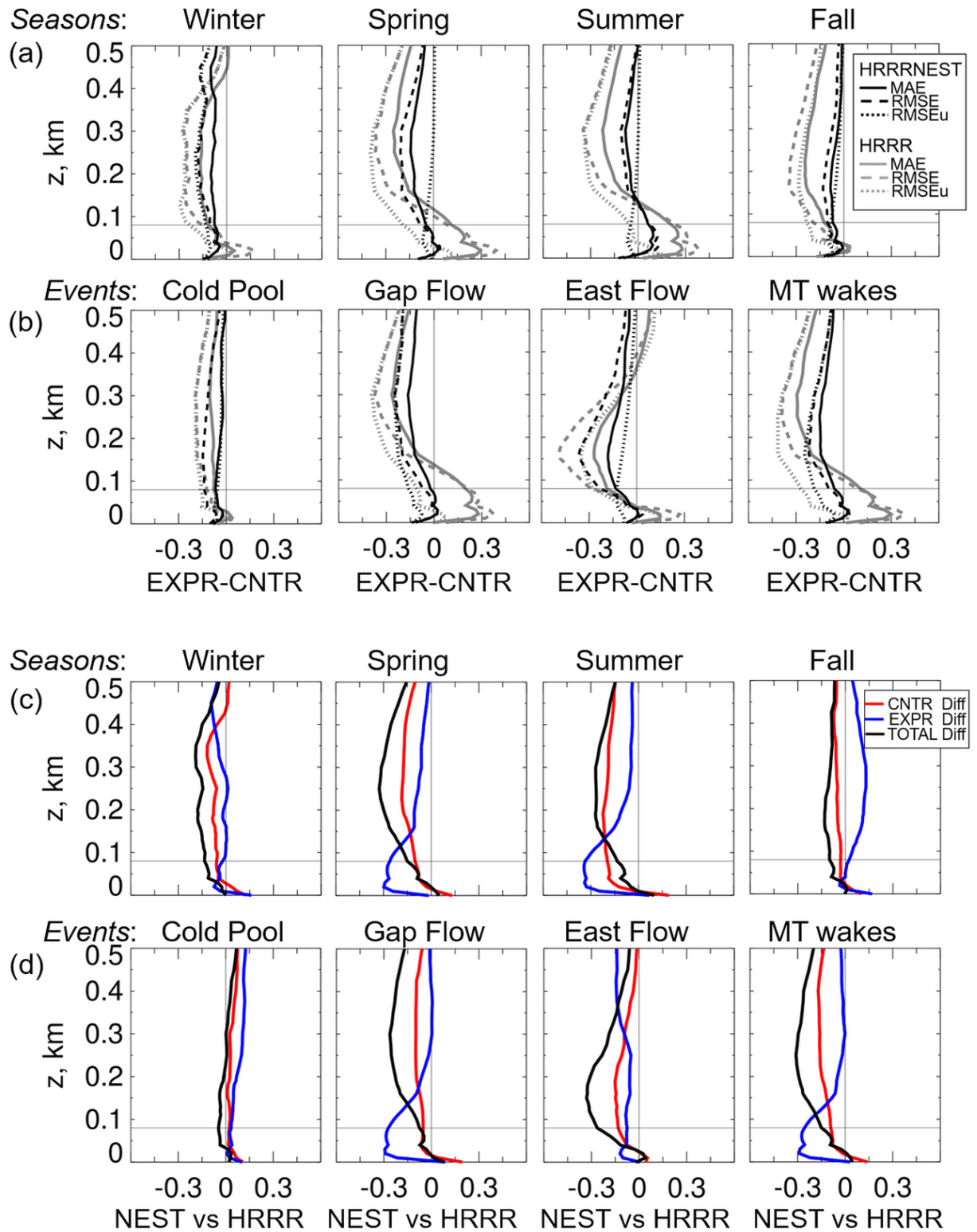
This is the author's peer reviewed, accepted manuscript. However, the online version of record will be different from this version once it has been copyedited and typeset.

PLEASE CITE THIS ARTICLE AS DOI: 10.1063/5.0009138



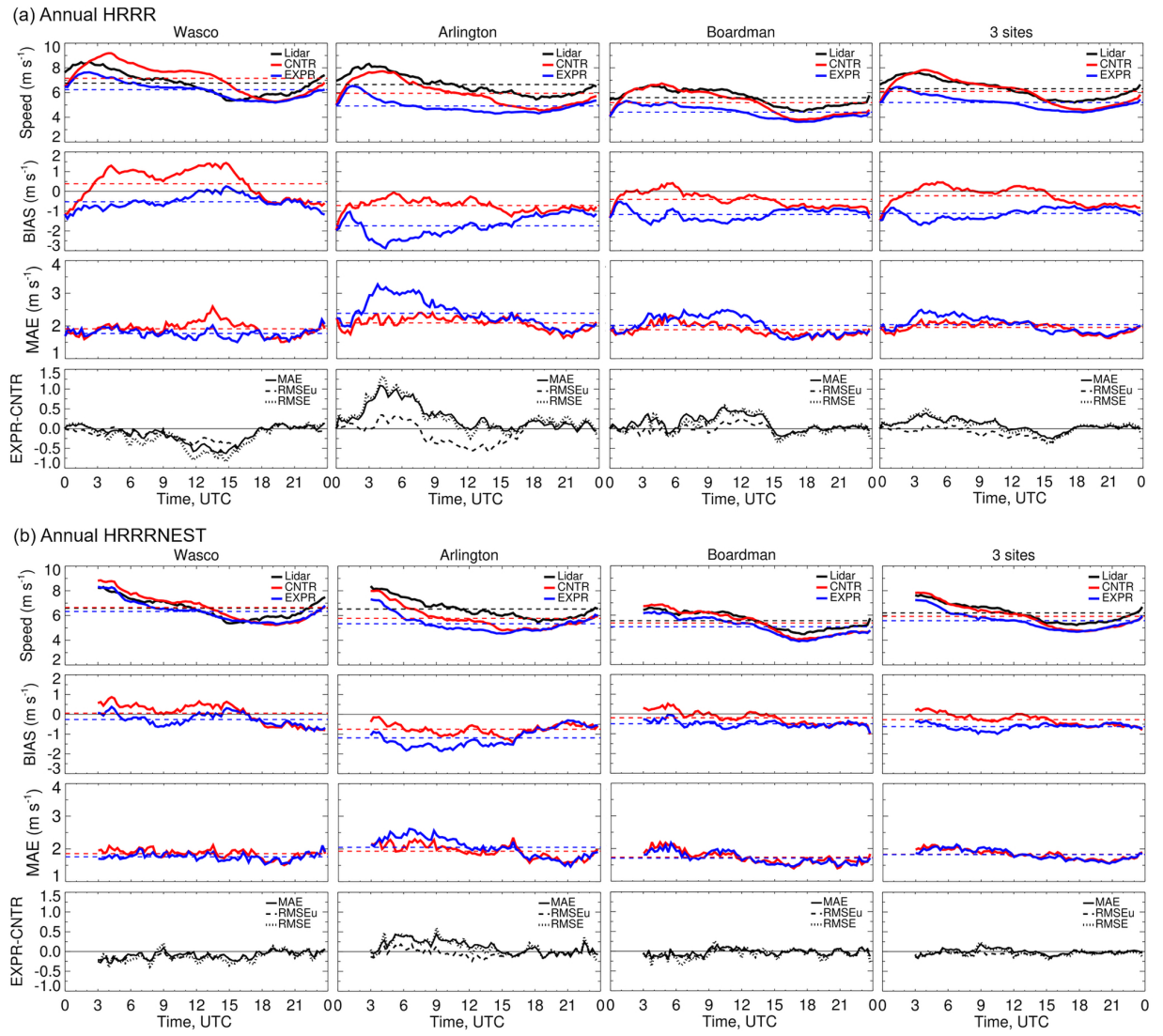
This is the author's peer reviewed, accepted manuscript. However, the online version of record will be different from this version once it has been copyedited and typeset.

PLEASE CITE THIS ARTICLE AS DOI: 10.1063/5.0009138



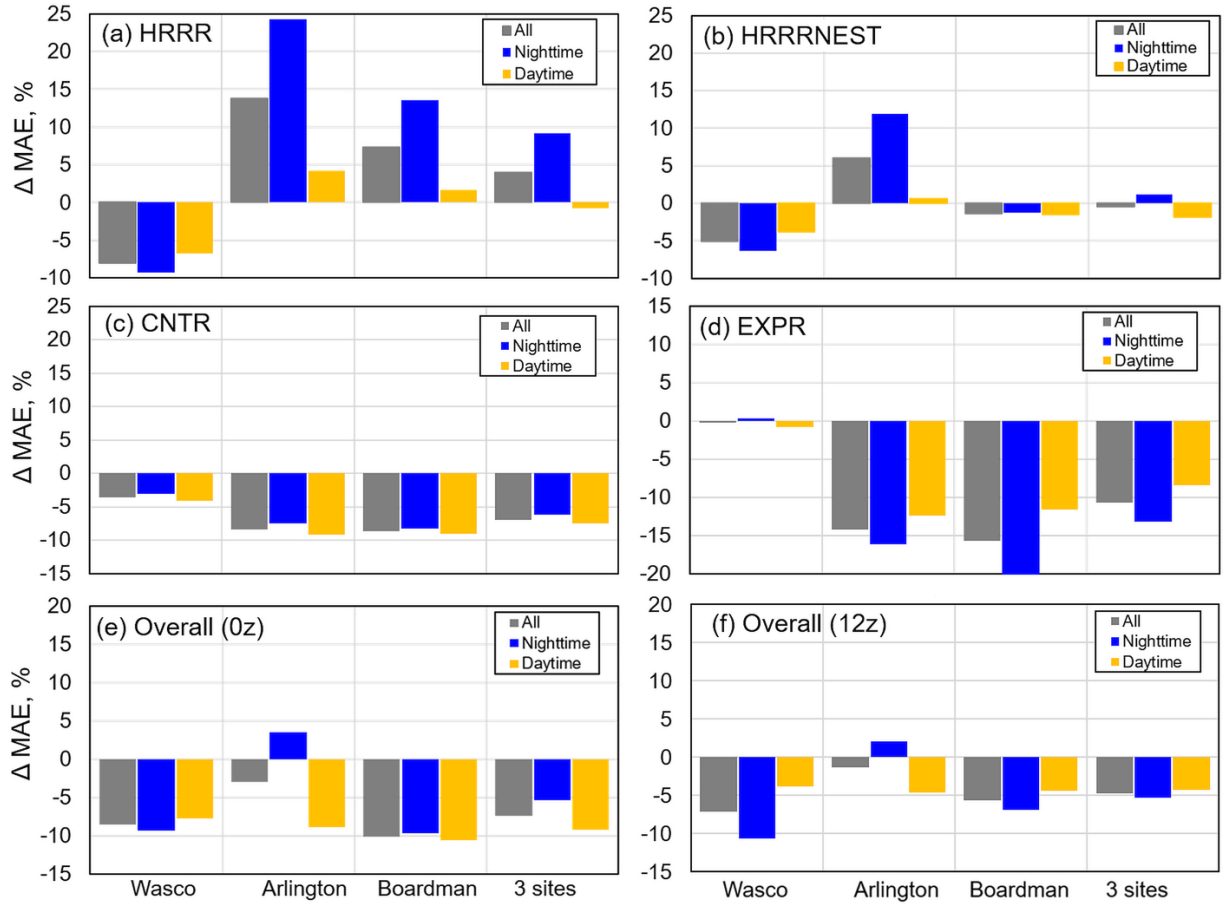
This is the author's peer reviewed, accepted manuscript. However, the online version of record will be different from this version once it has been copyedited and typeset.

PLEASE CITE THIS ARTICLE AS DOI: 10.1063/5.0009138



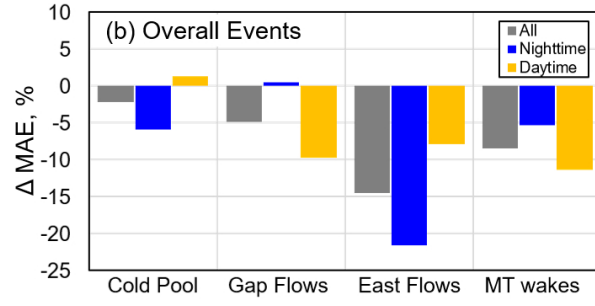
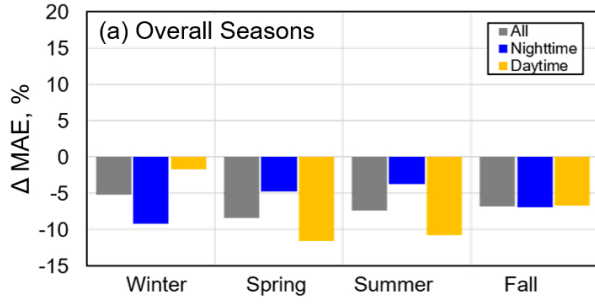
This is the author's peer reviewed, accepted manuscript. However, the online version of record will be different from this version once it has been copyedited and typeset.

PLEASE CITE THIS ARTICLE AS DOI: 10.1063/5.0009138



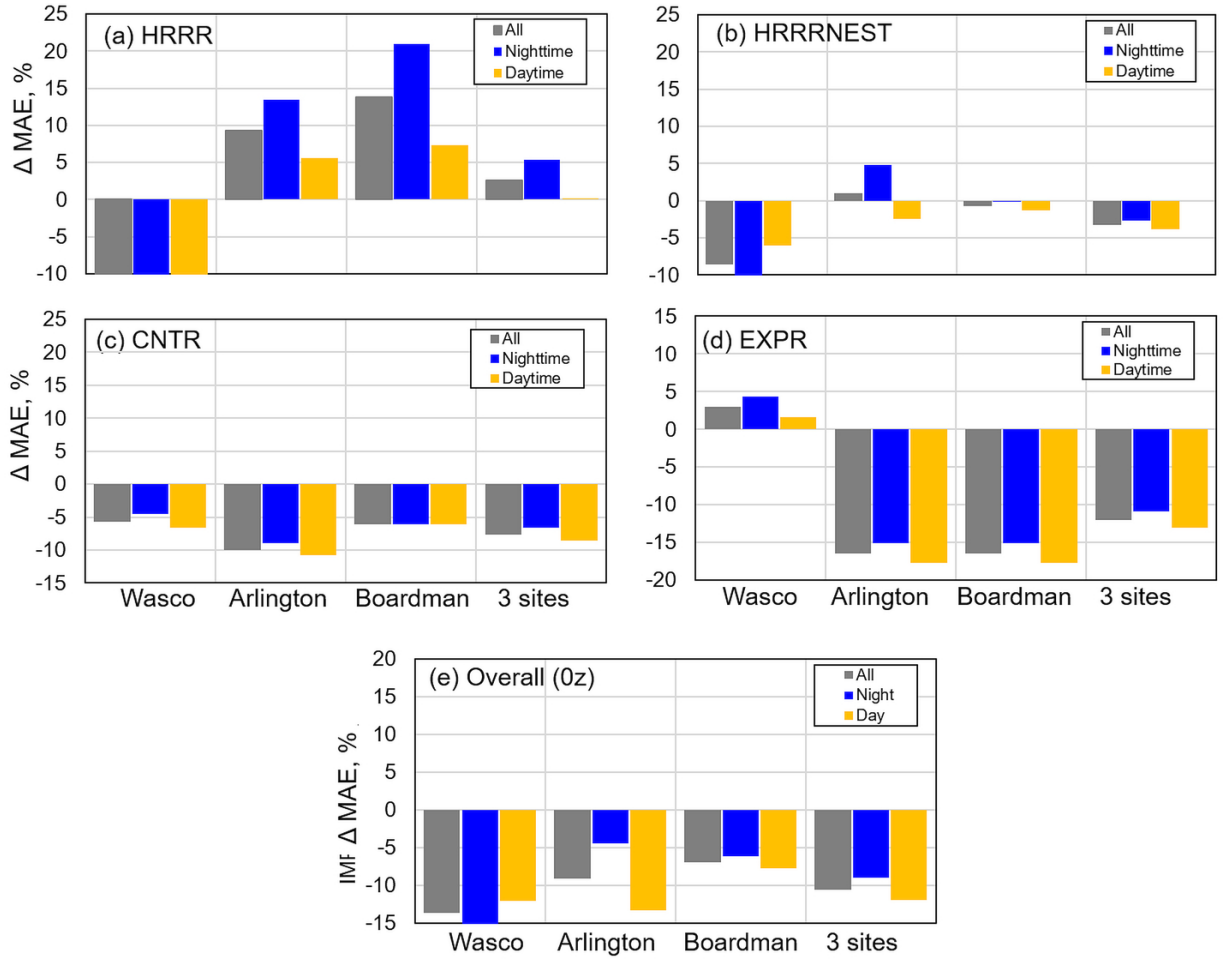
This is the author's peer reviewed, accepted manuscript. However, the online version of record will be different from this version once it has been copyedited and typeset.

PLEASE CITE THIS ARTICLE AS DOI: 10.1063/5.0009138



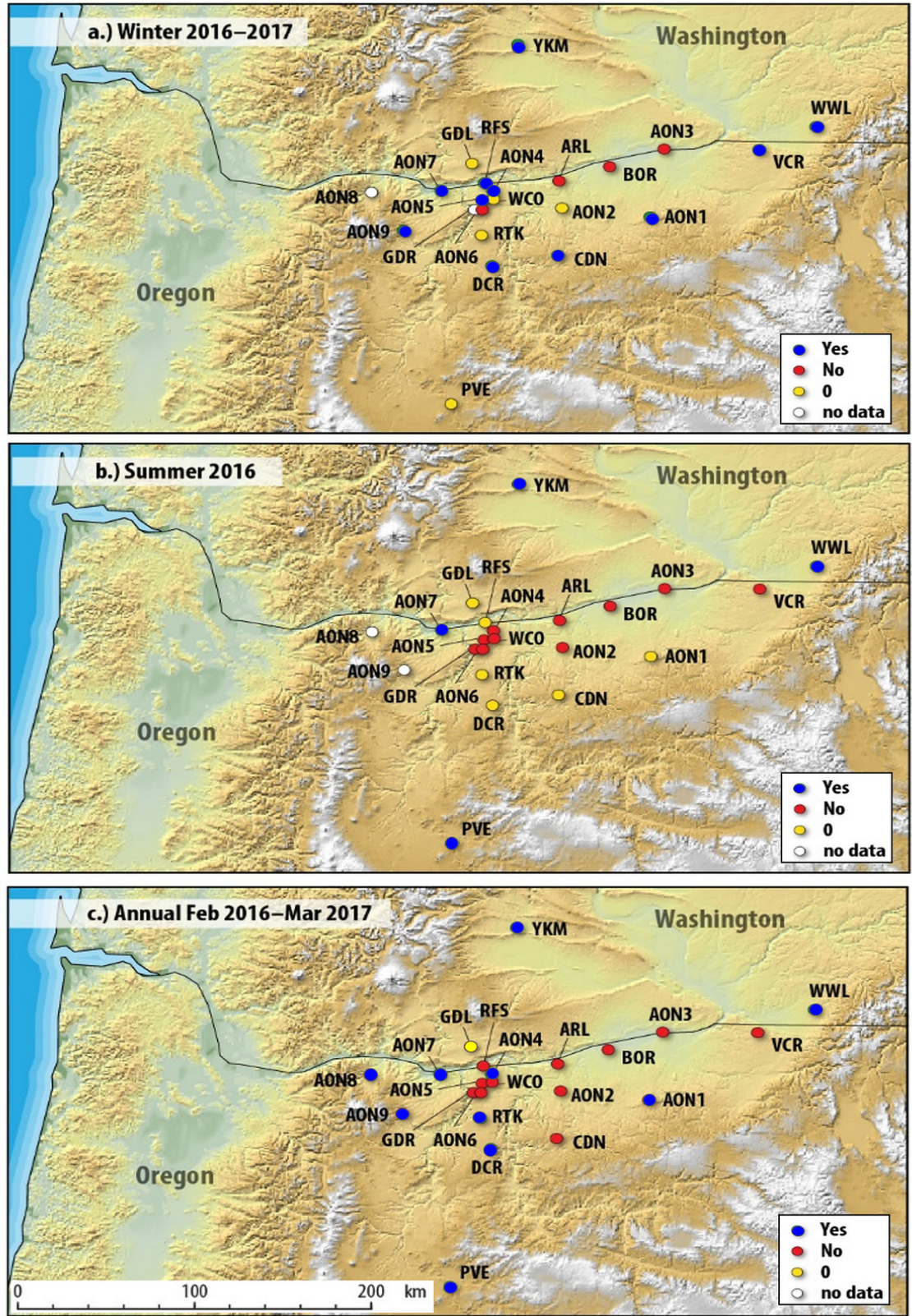
This is the author's peer reviewed, accepted manuscript. However, the online version of record will be different from this version once it has been copyedited and typeset.

PLEASE CITE THIS ARTICLE AS DOI: 10.1063/5.0009138



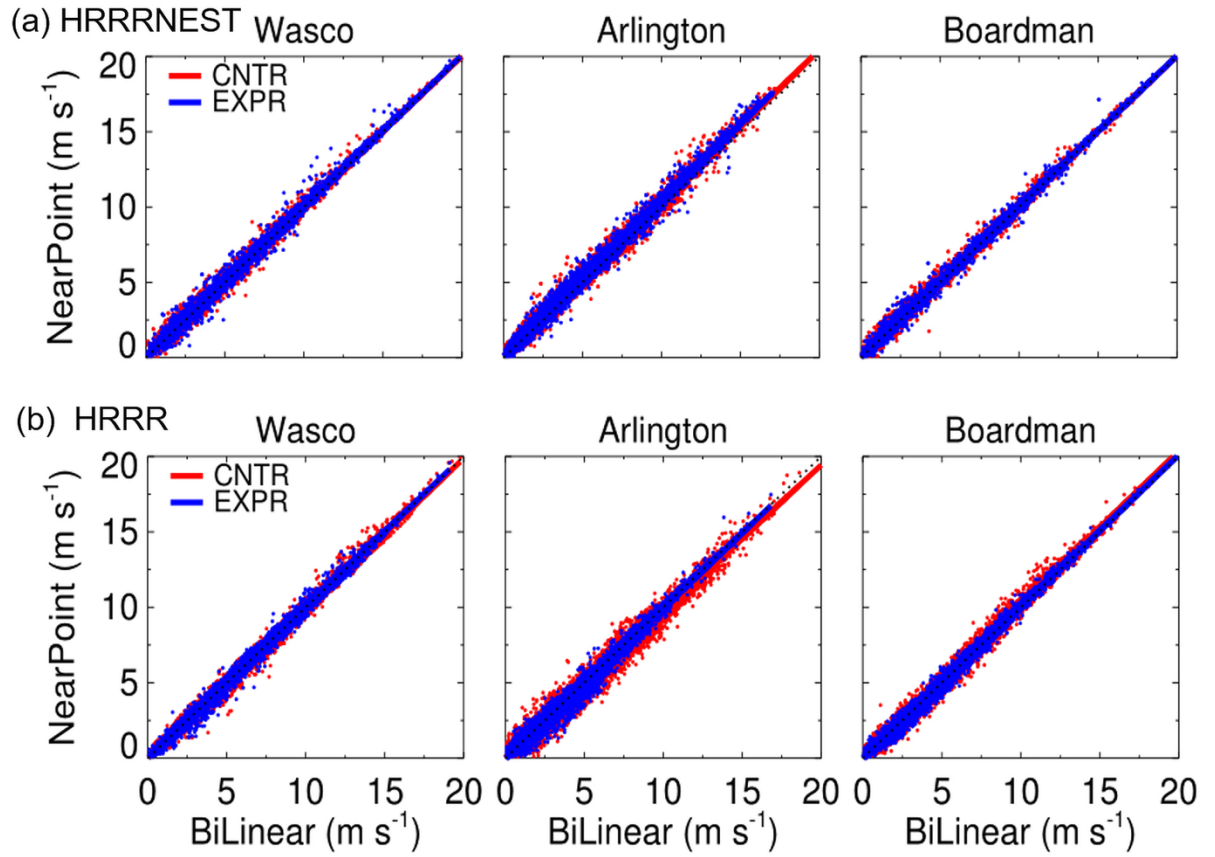
This is the author's peer reviewed, accepted manuscript. However, the online version of record will be different from this version once it has been copyedited and typeset.

PLEASE CITE THIS ARTICLE AS DOI: 10.1063/5.0009138



This is the author's peer reviewed, accepted manuscript. However, the online version of record will be different from this version once it has been copyedited and typeset.

PLEASE CITE THIS ARTICLE AS DOI: 10.1063/5.0009138





This is the author's peer reviewed, accepted manuscript. However, the online version of record will be different from this version once it has been copyedited and typeset.

PLEASE CITE THIS ARTICLE AS DOI: 10.1063/5.0009138

